DESIGNING AND UNDERSTANDING HEMATITE BASED NANOMATERIALS FOR SOLAR ENERGY APPLICATIONS

by

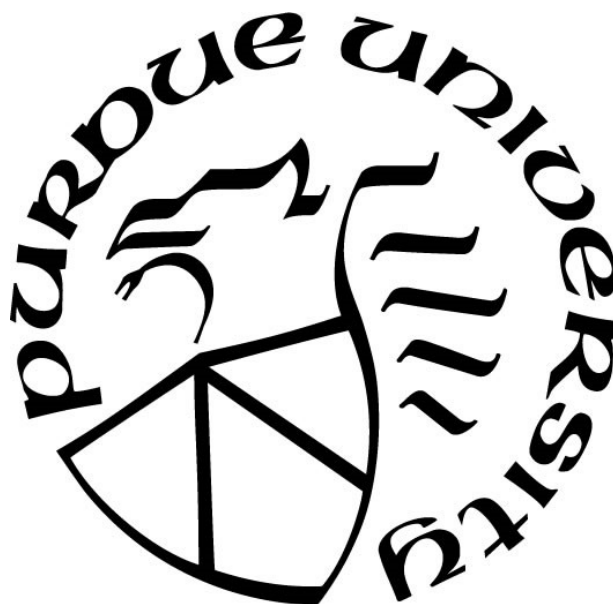**Melissa P. Cardona**

A Dissertation

Submitted to the Faculty of Purdue University

In Partial Fulfillment of the Requirements for the degree of

Doctor of Philosophy

Department of Chemistry

West Lafayette, Indiana

May 2019

THE PURDUE UNIVERSITY GRADUATE SCHOOL
STATEMENT OF COMMITTEE APPROVAL

Dr. Chen Yang, co-chair

Department of Electrical & Computer Engineering, Department of
Chemistry, Boston University

Dr. Christina Li, co-chair

Department of Chemistry

Dr. Tong Ren

Department of Chemistry

Dr. Jianguo Mei

Department of Chemistry

Approved by:

Dr. Christine Hrycyna

Head of the Graduate Program

ACKNOWLEDGMENTS

I would like to express gratitude to my advisor, Professor Chen Yang, for her guidance, encouragement and advice throughout my graduate studies, which have allowed me to grow as a scientist and researcher. I would also like to thank my committee member and co-chair, Professor Christina Li, and my committee members Professor Tong Ren and Professor Jianguo Mei, for their support.

I sincerely thank Dr. Hartmut Hedderich and Dr. Patricia Bishop of Purdue University JAFCI for their assistance and insights regarding spectroscopic instrumentation. I also sincerely thank Mr. Paul Mak of the Boston University Optoelectronic Processing Facility for training me on instrumentation, assisting in the set-up of laboratory instrumentation and helping solve multiple technical problems; and Dr. Jeffrey Bacon of the BU Chemical Instrumentation Center for training with and useful discussions regarding X-Ray Reflectivity measurements and analysis.

I would like to thank Professor Yat Li at UC Santa Cruz for supporting my experiments, and Professor Dunwei Wang at Boston College for allowing us access to his instrumentation for some photoelectrochemical measurements.

To my current and former Yang Lab colleagues, Dr. Wexia Zhang, Dr. Yunlong Zi, Dr. Sarath Ramadurgam, Dr. Tzuging Lin, Dr. Kelly McNear, Dr. Jeremy McCall, Katherine Hansen, Yimin Huang, Xingda An, Amartya Dutta, Linli Shi, Nan Zheng and Sulaiman Abdul-Hadi, thank you for your encouragement and support over the years, I have learned so much working with all of you. Thank you also to Dr. Wei Li from Professor Dunwei Wang's group for assistance with IMPS experiments and insightful discussions, and Dr. Mingyang Li of Prfoessor Yat Li's group for providing hematite samples for my experiments.

Finally, I want to thank my friends and family, especially my boyfriend, Brian, my parents, Ida and Charlie, and my sister, Jillian, for their love and support in everything I pursue.

TABLE OF CONTENTS

LIST OF TABLES

LIST OF FIGURES

LIST OF ABBREVIATIONS

Atmospheric pressure Chemical Vapor Deposition (APCVD)

Atomic layer deposition (ALD)

Charge transfer efficiency (CTE)

Chemical Vapor Deposition (CVD)

Core-multishell (CMS)

Core-Shell (CS)

Deposition-Anneal (DA)

Electrical impedance spectroscopy (EIS)

Ferrocene (FeCp$_2$)

Fluorine doped tin oxide (FTO)

Intensity modulated photocurrent spectroscopy (IMPS)

Linear sweep voltammetry (LSV)

Longitudinal acoustic (LA)

Nanoparticle (NP)

Nanowire (NW)

Photoelectrochemical (PEC)

Plasma enhanced atomic layer deposition (PEALD)

Poly methyl methacrylate (PMMA)

Reduced graphene oxide (rGO)

Scanning electron microscopy (SEM)

Single layer graphene (SLG)

Tetrakis(dimethylamido) titanium (TDMATi)

Transverse acoustic (TA)

Transverse optic (TO)

X-Ray Diffraction (XRD)

X-Ray Reflectivity (XRR)

ABSTRACT

Author: Cardona, Melissa, P. PhD
Institution: Purdue University
Degree Received: May 2019
Title: Designing and Understanding Hematite Based Nanomaterials for Solar Energy
     Applications
Committee Chair: Chen Yang

Solar water splitting (photoelectrocatalysis) is a sustainable method of hydrogen fuel production. Hematite (α-Fe_2O_3) is a promising photocatalytic material due to its favorable band gap (2.1 eV), stability and low cost. However, overcoming hematite's poor surface and electrical properties is crucial for improving its solar to hydrogen efficiency. This dissertation designs and investigates nanomaterial-based techniques to promote electron/hole pair generation and separation to enhance hematite's photocurrent density.

To this end, I first demonstrate that single layer graphene (SLG) can be transferred to the surface of nanostructured, titanium doped hematite. The transfer is confirmed and the SLG improves the photocurrent density by 1.6 times compared to uncoated hematite. Electrochemical techniques are employed to reveal the role of the single layer graphene overlayer and the reason for improved water oxidation. First, Electrical Impedance Spectroscopy under AM 1.5G solar illumination shows that the SLG affects the resistance and capacitance at the surface-electrolyte interface. Direct kinetic studies were carried out using Intensity Modulated Photocurrent Spectroscopy. This revealed that the SLG results in a decreased charge transfer rate and a decreased charge recombination rate. Therefore, though SLG inhibits charge transfer, its role as an overlayer on hematite is reduced recombination at the electrode surface, allowing for higher yield of charge carriers available for the oxygen evolution reaction. This demonstrates that SLG acts as a

passivation layer on hematite. SLG overlayers also improve the photocurrent density of TiO$_2$ photoanodes, demonstrating that SLG overlayers have the potential to act as a general surface-modification technique to improve the efficiency of semiconductor photocatalysts.

Second, I conduct theoretical studies to calculate the ideal photocurrent density of metal-semiconductor core-shell (CS) and semiconductor-metal-semiconductor core-multishell (CMS) nanowires (NWs). Using emerging plasmonic metals TiN and ZrN as the metal core or metal interlayer, the photocurrent density of sub-50 nm hematite features is enhanced. One key to fabricating these CS and CMS NWs is the synthesis of ultra-thin plasmonic metal nitride materials. To achieve this, a TiN synthesis is developed via plasma enhanced atomic layer deposition (PE-ALD) using TDMATi and NH$_3$ plasma precursors. Using Raman spectroscopy, it is observed that this ALD method produces nitrogen vacant TiN$_x$. Ellipsometry results confirm that the TiN is plasmonic with a broad visible light plasmon resonance. On silicon substrates, the plasmon wavelength is at 646 nm and 651 nm for TiN film thicknesses of 50 and 10 nm, respectively. Therefore showing that plasmonic TiN thin film fabrication is possible using a PE-ALD method and that the plasmonic properties are retained for ultra-thin films, making them suitable for plasmon enhancement of hematite nanomaterials.

CHAPTER 1.   INTRODUCTION

1.1   Motivation

As the world transitions toward meeting global energy needs with renewable sources, hydrogen (H_2) has been targeted a promising and exciting alternative to traditional fossil fuels. At 120 MJ/kg, hydrogen has the highest mass energy density of any known fuel source including gasoline (44.4 MJ/kg) , natural gas (43 MJ/kg) and coal (24 MJ/kg). In a hydrogen fuel cell, the chemical-to-electrical energy conversion can reach 60% which is higher than that of combustion engines according to the United States Department of Energy. Hydrogen is also a clean fuel that does not emit dangerous byproducts or carbon-based greenhouse gasses when burned; a hydrogen fuel cell produces only electricity, heat and water. Hydrogen fuel cells have the potential to provide fuel for vehicles, and electricity for buildings, homes and electronic devices.[1]

However, hydrogen in the form of H_2 is not a naturally occurring molecule on earth. It is abundant in compound form, bonded within molecules such as CH_4, NH_3, etc. Therefore, despite the promise of hydrogen fuel and fuel cells, sustainable production of H_2 presents unique challenges. Currently, 95% of the nine million metric tons of H_2 produced in the United States is done so using natural gas reforming (also known as steam methane reforming or steam reforming).[2] This two-step process consists of methanization to produce carbon monoxide and hydrogen, and reacting the CO byproduct using the water-gas shift:

This process produces high hydrogen yields of 65-75%, and is nearly cost competitive with gasoline production.[3] But, despite these advantages and the popularity of this method, the byproduct of the greenhouse gas CO_2 means that for long-term, large-scale

energy storage, this method should be replaced by more environmentally friendly alternatives.

What is desired for the future of hydrogen energy production is an efficient, low cost pathway with zero carbon emissions. Though they currently make up a much smaller part of the hydrogen fuel economy, there are many other pathways for hydrogen production that meet all or part of these needs including biomass gasification, coal gasification, microbial biomass conversion and water electrolysis.[4] Of particular interest is releasing hydrogen from water, most commonly done in the form of electrolysis, which uses a bias to drive the following endothermic reaction:

$$H_2O \ \rightarrow \frac{1}{2} \ O_2 \ + \ H_2$$
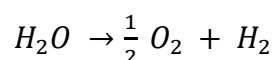
This is a zero-carbon emission reaction. Additionally, photoelectrochemical (PEC) water splitting can be conducted by certain materials (photocatalysts) using solar energy to drive the reaction. Solar driven electrolysis is known as photocatalysis, photoelectrocatalysis or solar water splitting. Optimizing and understanding this procedure provides a sustainable pathway for large-scale hydrogen production.

1.2 Overview of Semiconductor Photocatalysts

The overall water splitting reaction is the summation of two half reactions. Photogenerated holes conduct water oxidation. This four-hole transfer is the rate limiting step and often called the "kinetic bottleneck" of water decomposition. This reaction takes place at the anode.

$$2H_2O + 4h^+ \ \rightarrow 4H^+ + \ O_2$$
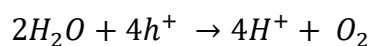
Photogenerated electrons participate in water reduction, resulting in the hydrogen product that can be used a fuel. This reaction takes place at the cathode.

$$2H^+ + 2e^- \rightarrow H_2$$
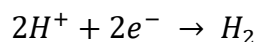
In the case of semiconducting materials for water splitting, the electronic structure of the semiconductor plays a large role in its photocatalytic mechanism. Upon irradiation of light, electrons are excited from the valence band to the conduction band. When electrons migrate to the surface electrolyte interface without undergoing recombination, they react to evolve hydrogen. Similarly, holes in the valence band migrate to the electrode surface and react with water to evolve oxygen (Figure 1.1). .
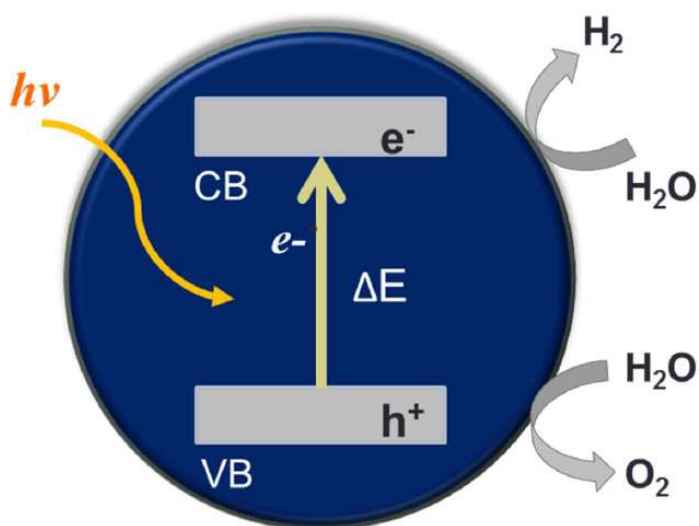
Figure 1.1 Mechanism of semiconductor (i.e. TiO$_2$) photocatalytic water splitting

Important in the solar water splitting efficiency of the semiconductor is the energy gap between the conduction and valence bands, ΔE. In general, a semiconductor can absorb wavelengths of light that are equal to or less than is bandgap. Therefore, it is important to select and design semiconductor materials with bandgaps alight with visible light

absorbance. Especially important is visible light absorption near 500 nm, as this is wavelength of peak solar emission.

For efficient water splitting, band alignment is equally important as bandgap. To avoid large overpotential for hydrogen evolution, the conduction band must be more negative than hydrogen reduction potential (0.0 V_{RHE}). For oxygen evolution, the valance band more positive than the water oxidation potential (1.23 V_{RHE}).

The first photocatalyst, a TiO_2 semiconductor electrode that performed the electrolysis of water under solar irradiation and anodic bias potential, was discovered by Fujishma and Honda in 1972.[5] TiO_2 has a 3.2 eV band gap and the alignment of its valence and conduction bands results in the ability to perform the water reduction and oxidation reactions, respectively. Since this first study, much research has gone into improving the PEC efficiency of TiO_2 as well as exploring new materials as water splitting catalysts, to optimize hydrogen generation.

Many semiconductor materials have since been discovered to have photocatalytic properties. Some, such as silicon and TiO_2, have band alignment consistent with performing the full water splitting reaction with little theoretical overpotential (Figure 1.1). Others, such as Cu_2O and WO_3, have band alignment with only the hydrogen or oxygen evolution half reaction, respectively. It is possible to have a PEC cell using two photoelectrodes to perform the water splitting reaction. For example, TiO_2 in NaOH (aq) to perform water oxidation and Si in H_2SO_4 (aq) to perform water reduction. Alternatively, materials such as these are often used to study one half-reaction using a two-electrode set-up, utilizing a photoanode/counter electrode for water oxidation and photocathode/counter electrode for water reduction.

Since the discovery of TiO_2, there has been much research conducted to overcome its limitations on the solar water splitting efficiency. One such limitation is TiO_2 solar absorption is limited by its wide bandgap, limiting its visible light absorbance to ~ 420 nm, leading researchers to attempt to modify the TiO_2 bandgap to allow for visible light absorbance using a variety of techniques.[6-7] Many have alternatively sought out smaller bandgap photocatalysts such as CdS, WO_3 and α-Fe_2O_3.[8]

1.3   Advances in Metal Oxide Semiconductor Nanomaterials for Photocatalysis: A Case Study using Hematite

Hematite (α-Fe_2O_3) was first reported as a smaller-band gap photocatalyst by *Hardee and Bard* in 1976[9] and is an excellent test material to study enhancement techniques for PEC applications. Though requiring large overpotentials for water reduction, its band alignment makes it a promising photoanode for the oxygen evolution half-reaction. The greatest promise of hematite is its band gap of 2.1-2.2 eV resulting in visible light absorption up to 560-580 nm. This band gap correlates to a theoretical solar-to-hydrogen conversion efficiency of approximately 15%, over six times greater than the 2.2% predicted for TiO_2 (rutile phase). Additionally, unlike some other small-bandgap semiconductors, iron oxide is inexpensive, earth abundant, non-toxic and thermodynamically stable and chemically stable in neutral and high pH aqueous medium

Despite these promising characteristics, hematite is limited by its poor electrical properties and sluggish oxygen evolution kinetics compared to other metal oxide photoanodes. Its short electron/hole diffusion length of 2-4 nm leads to high recombination rates.[10] Because of this, techniques such as nanostructuring to increase surface area and

improve charge transport are important to obtain good hematite performance. Even so, hematite underperforms compared its theoretical photocurrent density.

1.3.1   Charge Separation Techniques: Surface Modification and Plasmon Enhancement

Because many of hematite's electronic shortcomings affect the surface electrolyte interface, where the water oxidation reaction takes place, one technique to improve hematite's performance is modifying the material surface. For one, hematite's kinetic rate of charge transfer is slower than other metal oxide photoanodes. To this end, nano-scale metal based co-catalysts such as cobalt phosphate ("Co-Pi") and iridium dioxide (IrO_2) have been demonstrated to improve the oxygen evolution reaction by making the reaction more kinetically favorable.[11,12-13] Another problem to overcome is the large number of surface states on hematite, which trap holes and act as recombination centers. This results in high surface recombination rates and limits hematite's photoelectrochemical efficiency.[14] To address this thermodynamic limitation, surface modification techniques are used, passivating surface states with ultrathin metal oxide films such as Al_2O_3[15], and TiO_2.[16-17] Alternatively, acid treatments have been shown to suppress surface electron-hole recombination, attributed in part to surface state elimination.[18] Co-catalysts and passivation techniques can also be combined, and doing so has been demonstrated to reduce the turn-on potential and increase photocurrent density in hematite photoanodes.[19]

Improving charge transport and increasing electron/hole pairs in the bulk of the film is also important for enhancing hematite as a PEC material. Ideally, structures need to be electrically thin enough for efficient charge mobility but optically thick enough for good visible light absorption. Plasmonic metal nanostructures can be used to address this

problem. When the plasmonic metal is surrounded by the photocatalyst, two mechanisms occur that are beneficial to hematite's performance: hot electrons caused by plasmon decay which drive the water splitting reaction, and increased photon absorbance in the surrounding semiconductor.[20-21] Gold NPs embedded in hematite thin films improve photocurrent density by increasing increases the number carriers in the film.[22] Gold nanopillars coated in hematite increase the absorbance in hematite to improve photocurrent density.[23] Unassisted water splitting is achieved by embedding and decorating hematite with Au NPs on a silicon nanowire scaffold.[24] Alternative plasmonic metals such as aluminum have been demonstrated to improve hematite's absorption efficiency and photocurrent density when used as the metal layer in semiconductor-metal-hematite CMS NW archetectures.[21, 25] More recently, plasmonic metal nitride materials have emerged to enhance solar water oxidation efficiency.[26]

While surface modification and plasmon enhancement of hematite photoanodes may at first seem like very different techniques to improve solar to hydrogen efficiency, they both aim to increase the number of available holes to participate in the water splitting reaction. Surface modification, especially by passivation layers, may decrease the rate of recombination at the surface-electrolyte interface. Increasing optical absorption using plasmonic nanostructures increases the total number of photo-generated electron/hole pairs. Ultimately, a combination of techniques to increase the yield and lifetime of charge carriers (nanostructruing, doping, surface modification, optical enhancement) will likely be needed for hematite to reach its ideal theoretical photocurrent density.

1.4   A Unique Chemical Synthesis Approach: Atomic Layer Deposition

Atomic layer deposition (ALD), a subset of the Chemical Vapor Deposition (CVD) technique, is a method of depositing thin, inorganic materials from high vapor pressure precursors. Introduced and alternatively known as Atomic Layer Epitaxy, this technique was first developed via experimental work in the 1960s and 1970s[27-28] and has excelled in popularity ever since, at least in part thanks to miniaturization in the microelectronics industry.[29] The main advantages of this technique are the ability to synthesize conformal materials with sub-nanometer thicknesses and the conformal coating of high aspect-ratio nanostructures.[30]
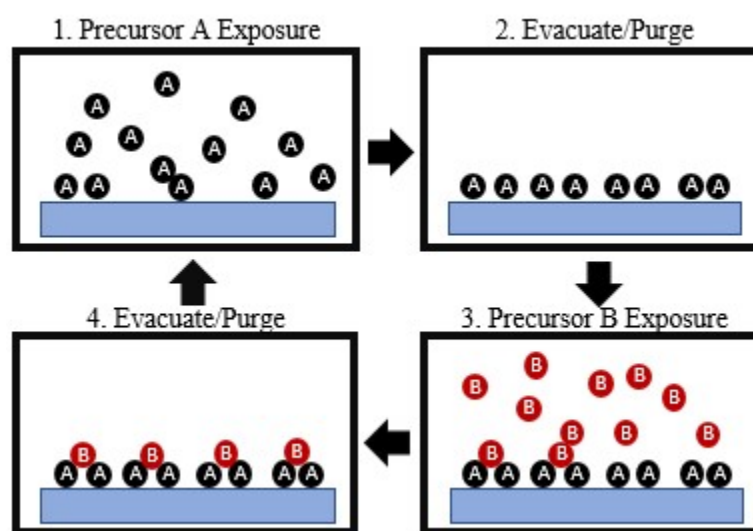
Figure 1.2 Pictorial representation of one ALD cycle using precursors A and B to synthesize monolayer A_2B

As opposed to traditional CVD, ALD is based on chemical reactants pulsed alternatively in two self-limiting half cycle reactions. The four main steps that make up an ALD cycle are: (1) The first pulse exposes the substrate to precursor A (often a metal-organic molecule), which reacts with and adsorbs to the substrate surface (2) The un-adsorbed precursor is evacuated (purged) using an inert carrier gas. (3) The second half-

cycle exposes the substrate to precursor B (often an oxidizing or reducing agent), which reacts with precursor A. (4) the excess, unreacted precursor B is purged from the chamber, thus completing one ALD cycle (Figure 1.2). Since each cycle deposits at most one monolayer of material, the sub-nm control that marks ALD is gained by repeating this cycle until desired thickness is reached. The substrate and chamber are kept under vacuum (often on the order of 10 mT) at a designated temperature, the precursors each pulsed for a designed amount of time such that the reaction takes place completely, and the chamber evacuated/purged for a sufficient amount of time to evacuate excess reactant material. While possibly most associated with the growth of aluminum oxide dielectric materials, an extensive list including ultra-thin oxide, nitride and sulfide materials have been fabricated using this technique.[29, 31]

Traditionally, ALD reactions take place between two vapor-phase precursors and the energy for surface reaction is supplied by thermal energy. However, replacing a vapor phase precursor with a plasma, first demonstrated in 1991[32], has many advantages over the traditional thermal method.[33-34] The use of high energy radicals allows for common ALD reactions to occur at lower temperatures. The presence of ions and electrons within the plasma result in different film properties and can achieve higher film density and reduced impurity concentration compared to thermal growths. Additionally, the stoichiometry of many materials, such as metal oxides and nitrides, can be precisely controlled by changing the plasma mixture, power and duration.[33]

Herein, Plasma Enhanced ALD (PE-ALD) is the synthesis technique for two different materials systems. The first is for the metal oxides for solar water splitting applications. Iron oxide is synthesized using ferrocene and oxygen plasma, as detailed in

2.5. Titanium dioxide is synthesized via titanium isopropoxide and oxygen plasma, as detailed in 3.2. The second utilizes PE-ALD for the synthesis of plasmonic transition metal nitride thin films, as detailed in 4.2. All PE-ALD experiments were conducted on an Arradiance GEMStar XT-P Thermal- and PE- ALD instrument equipped with an air cooled, 300 W Inductively Coupled Plasma RF System.

1.5   Outline & Organization

Chapter 1 discusses the motivation of studying solar water splitting for sustainable hydrogen generation and makes a case for hematite based materials as an optimal photoanode to study solar water splitting enhancement techniques, and discusses recent progresses in hematite materials for PEC. It also gives an overview of atomic layer deposition, a unique synthesis technique for producing inorganic thin films.

Chapter 2 discusses the importance of nanostructuring and doping in hematite photoanodes and methods to synthesize nanostructured hematite photoanodes. It also outlines using Raman spectroscopy as a characterization technique to differentiate between various iron oxide products. Chapter 2 goes on to detail the procedure and characterization of the following hematite synthesis methods: chemical synthesis from iron salts, high temperature decomposition of ferrocene and plasma enhanced atomic layer deposition using ferrocene and oxygen plasma precursors. Synthesis parameters, film morphology and applicability to 1D nanostructured substrates are discussed.

Chapter 3 demonstrates the potential of using single layer graphene (SLG) as an overlayer on nanostructured hematite photoanodes to enhance the solar water oxidation reaction. The photocurrent density is compared with and without the SLG overlayer. The mechanism of enhancement is studied in detail using electrical impedance spectroscopy

and intensity modulated photocurrent spectroscopy. It is discovered that although the SLG overlayer inhibits charge transfer, it improves photocurrent density by 1.6 times by decreasing the surface recombination rate by over 80%.

Chapter 4 discusses using emerging plasmonic metal nitride materials, ZrN and TiN, for plasmon enhanced solar water splitting with hematite. Metal nitride/hematite core-shell and semiconductor/metal nitride/hematite core-multishell NW architectures are proposed and their photocurrent densities theoretically demonstrated. In pursuit fabricating these structures, a novel, low temperature ALD synthesis of TiN on silicon is achieved. Importantly, it is demonstrated that the synthesized TiN retains its plasmonic optical properties as the TiN film thickness is decreased to nearly10 nm, therefore making it suitable for the optimized core-multishell nanowire design.

Chapter 5 summarizes the research conducted and the results of this dissertation, and puts this work in the greater context of the field and future of nanostructured hematite and metal oxide nanomaterials for sustainable, solar driven hydrogen production. Additionally, it suggests future experimentation related to: optimization of graphene and graphitic overlayers on metal oxide photoanodes; further mechanistic studies into the role of carbon films on hematite; fabrication techniques for experimental analysis of semiconductor-metal nitride-hematite core multishell nanowires.

CHAPTER 2.   CHEMICAL SYNTHESIS OF HEMATITE

2.1   Introduction

To achieve good water oxidation efficiency, hematite photoanodes should have both efficient charge transport and sufficient optical absorption. Synthesizing hematite with a high degree of nanostructuring can help overcome its physical limitations and result in improved solar to hydrogen conversion. This can be accomplished by a variety of nanostructured morphologies including: synthesizing nanoparticles of various size and shape, fabricating precisely designed nanostructures such as core-shell or core shell-shell nanowires, or deposition of ultra-thin, conformal films. The structure is highly dependent on the synthesis method. It is desirable to use an environmentally friendly, safe, reproducible and cost-effective method that results in high quality hematite with high photocurrent density when possible.

A variety of synthesis techniques have been used to make hematite photoelectrodes. Previously established is that hematite with a high degree of nanostructuring improves upon its photocurrent density by both increasing the photoanode surface area and retarding charge recombination. For example, electrodeposited nanocrystalline thin films show enhanced charge separation compared uniform thin films.[35-36] Particle crystallinity, size, shape and collective film thickness all contribute to achieving high photocurrent densities Dopants also play a unique role, increasing charge lifetime in nanostructured films, and high performance hematite often combines nanostructuring with doping.[37] Examples of high performance anodes include silicon doped "cauliflower" shaped hematite nanostructures with excellent photooxidation properties prepared by APCVD;[12, 15] and worm-like single crystal hematite nanostrucutres doped with platinum via hydrothermal

synthesis.[38] Therefore, a synthesis method with the potential incorporate transition metals dopants into the nanomaterial is desirable.

Alternative synthesis mythologies must be employed if the goal is to achieve thin, conformal films or nano-scale coatings. Though costlier than some other methods, atomic layer deposition (ALD) can be utilized. This method has been demonstrated to produce hematite with sub-nanometer thickness control and can be modified to allow for the incorporation of titanium dopants.[39-41] One specific type of nanostructuring that is often desirable is 1D nanostructures, such as thin hematite shells on silicon nanowires. For the deposition of hematite around high-aspect ratio NW arrays, ALD can do so with greater precision and conformality [42] than chemical synthesis from iron salts.[24]

This chapter will discuss and characterize iron oxide from three different synthesis methods in detail: wet chemical syntheses from iron salts, a unique deposition of hematite from ferrocene, and ALD of hematite using the novel precursor combination ferrocene and oxygen plasma.

2.2   Characterization of Iron Oxide Nanomaterials

Hematite is the only of iron oxide compound with demonstrated photocatalytic activity. Therefore, to ensure that the synthesis is successful in producing α-Fe_2O_3, it is important to have a technique to characterize iron's many oxidation products: iron (II) oxide (FeO called wustite), iron (II/III) oxide (Fe_3O_4 called magnetite), and the iron (III) oxides γ-Fe_2O_3 (maghmite) from α-Fe_2O_3 (hematite). One tool for distinguishing between different iron oxide compounds is Raman spectroscopy.

The "Raman Effect" relies on the inelastic scattering of light from a material which then undergoes a frequency shift by the energy of its molecular vibrations.[43] Therefore

Raman spectroscopy can be used to characterize low frequency vibrational modes in a system. Observing these characteristic vibrational modes allow us to use this non-invasive, non-destructive technique to get structural information to identify molecules, materials and crystals.[43-44] Raman spectroscopy is used throughout this thesis to identify the vibrational modes of metal oxide, metal nitride and carbon based nanomaterials. In this section, Raman spectroscopy's primary use is to differentiate α-Fe_2O_3 from the variety of alternative iron oxide products.

Hematite has seven Raman active phonon modes: $2A_{1g}+ 5E_g$. A forbidden E_u mode also appears in some Raman analysis of hematite. While in some samples it may be due to the presence of iron (II) oxides such as magnetite or wustite,[45] it is generally recognized in samples of pure hematite to be caused by disorder or the presence of nanocrystals in the hematite lattice.[46] Additionally, as hematite is a ferromagnetic material, its collective spin movement can be excited; this is known as a magnon. The interaction of two magnons created on antiparallel close spin sites is a particularly intense feature in the hematite Raman spectrum.[47] Though variations in exact Raman shift frequencies have been reported, the Raman shifts appear on the spectrum as follows: 226 (A_{1g}), 245 (E_g), 293 (E_g), 413 (E_g), 500 (A_{1g}), 612 (E_g), 660 (E_u) and 1315 (2nd order magnon scattering) cm^{-1}.[45, 47-48]

This is in contrast to the gamma-phase iron (III) oxide maghemite, which demonstrates poorly defined, broad bands at 350 (T_{2g}), 500 (E_g), and 700 (A_{1g}) cm^{-1}; additional peaks at 1400 and 1585 cm^{-1} have also been observed.[47-49] The iron (II) oxides magnetite and wustite have Raman signals indistinguishable from one another but unique from other iron oxides, with modes at 300 (T_{2g}), 532 (T_{2g}) and 661 (A_{1g}).[47]

Raman spectroscopy is used throughout to evaluate iron oxide products. One concern with this analysis technique is localized annealing caused by the excitation laser, which may make it difficult to accurately characterize the as-prepared iron oxide prodcut.[47] Therefore, laser power and acquisition time are crucial in the measurement of iron oxide samples. In all cases, the laser power is kept sufficiently low (≤ 6 mW) to avoid any phase conversion or crystallinity changes to the as prepared the iron oxide products.

2.3   Chemical Synthesis from Iron Salts

With hematite's growing popularity as a photocatalytic material, it is essential to have cost effective, safe, reliable methods of synthesis. One popular method for nanostructured hematite is to use aqueous solutions of iron salts such as $FeCl_3$ and $Fe(NO_3)_3$. The exact parameters for hydrothermal synthesis can vary widely. In general, this method involves heating the aqueous salt solution in a closed container at temperatures above 80° C for 4-24 hours, where the heating duration controls the size of the nanoparticles (NPs).[50-51] This can either be done to form free nanoparticles or, if the synthesis takes place in the presence of a substrate such as ITO, a thin film. The resulting film is an accumulation of iron oxy-hydroxide or iron oxide NPs, which often undergo anneal to complete the transformation to hematite and to improve the material's photoactivity.

The morphology of an annealed hematite film on FTO produced via hydrothermal deposition is represented in Figure 2.1, which depicts nanorods with average lengths of 332 ± 29.3 nm and average widths of 68.1 ± 9.43 nm. By varying the synthesis parameters and/or post-synthesis anneal conditions, a variety of intricate nanostructures have been reported[52] including vertically aligned nanorods and nanotubes[53-54], and urchin-like[55-57]

nanostructures. Different morphologies affect the PEC performance due to increased surface area, differences in charge transport and exposing the most photocatalytically active crystal face.
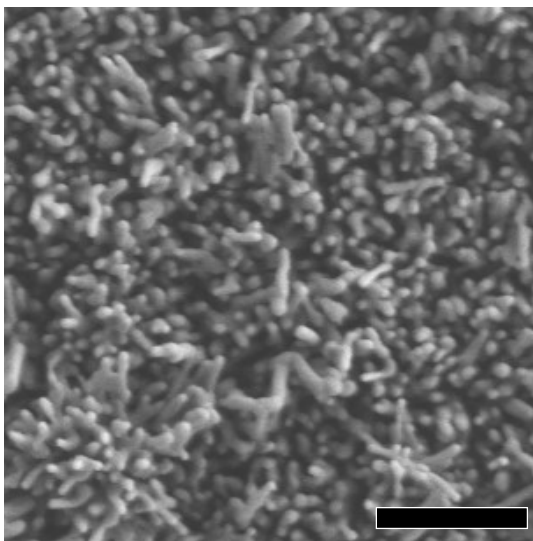
Figure 2.1 Representative SEM of nanostructured hematite thin film synthesized via hydrothermal deposition from an aqueous solution of 0.15 M $FeCl_3$, 1 M $NaNO_3$ and HCl at a pH between one and two. Reacted in a Teflon lined stainless steel autoclave at 90° C for four hours and annealed in air at 500° C for 30 minutes and 700° C for 15 minutes. Scale bar is 1 μm.

In addition to controlling NP morphology and crystallinity, another versatility of this method is that it allows for elemental doping with nonmetals[12, 58-59] and transition metals such as Ti[60] and Sn[61-62]. Doping may change the NP morphology, and often results in higher photocurrent density due to an increase and the number of charge carriers and an increase in the charge carrier lifetime in nanostructured films.[63] Intensity modulated photocurrent spectroscopy (IMPS) shows that hydrothermally synthesized hematite doped with titanium has overall lower rates of recombination and higher rates of charge transfer, resulting in higher charge transfer efficiencies. Specifically, at 1.2 V_{RHE} a sample of intrinsic hematite has a charge transfer efficiency (CTE) of 38% compared to Ti-doped

hematite with a CTE of over 77% (Figure 2.2). This thesis will use hydrothermal synthesis of titanium doped hematite to study hematite with and without surface modification. The exact parameters of the synthesis are detailed in 3.2
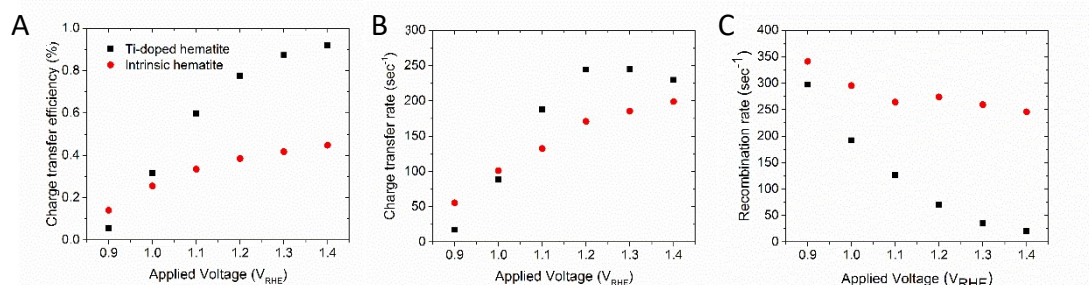
Figure 2.2 IMPS results depicting the (a) charge transfer efficiency, (b) rate of charge transfer and (c) rate of charge recombination for intrinsic (red circles) and Titanium doped (black squares) hematite photoanodes

Related to hydrothermal synthesis is the deposition-anneal (DA) method developed by *Wang et al.*[37] This involves drop-depositing $FeCl_3$ on the surface of FTO and annealing the substrate at 350° C to create a yellow film of β-FeOOH. This makes up one DA cycle. After the desired number of DA cycles have been completed, that β-FEOOH film is annealed at high temperature in air to form the nanostructured hematite film. Unlike hydrothermal synthesis, in which the baking time and temperature affect film parameters[64], the film thickness here is controlled by the number of DA cycles and the individual particle size by the $FeCl_3$ concentration.[24, 37] Films with closely packed, small NP sizes result in the best photocurrent densities. Additionally, this method first demonstrated incorporation of titanium as a dopant to enhance the PEC properties from 0.91 mA/cm^2 to 2.38 mA/cm^2 at $1.23V_{RHE}$.[37]

While solution based synthesis form iron salts have distinct advantages and may be optimal for FTO and similar substrates, it is limited when conducting the synthesis of

hematite shells on high-aspect ratio nanowires. Though it has previously been demonstrated to individually coat Si NW arrays, randomly aligned Si NWs synthesized via CVD provide unique challenges.

To test the effectiveness of this method on 1-D nanostructures, silicon nanowires are prepared by CVD, similar to previously described.[65] In short, a silicon substrate undergoes treatment in 30% HF to remove native oxide. PMMA and gold nanoparticles (40 nm) are drop deposited on the substrate onto the surface of the wafer. It is blown dry under a gentle, steady stream of nitrogen before being loaded into the CVD chamber. The CVD synthesis is performed at 460° C under vacuum using 10% silane and hydrogen. The chamber is cooled to room temperature before the silicon nanowire substrates are removed.
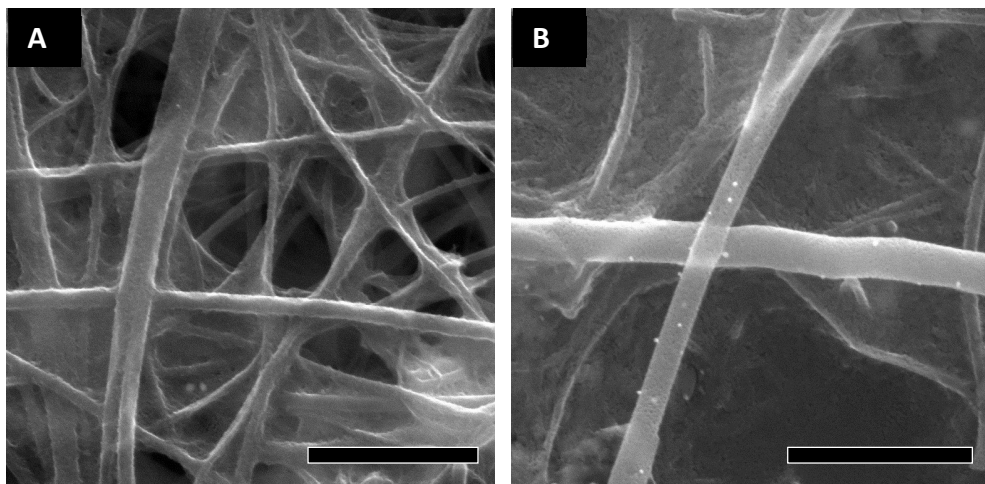
Figure 2.3. Hematite synthesis from ferric chloride on randomly aligned silicon nanowires using (a) 20 mM and (b) 40 mM aqueous solutions, followed by annealing at 500° C. Scale bars 1 μm.

Here we demonstrate hematite synthesis from iron salts similar to *Wang et al.*[37] Solid FeCl$_3$ (98%, Sigma Aldrich) is prepared into an aqueous solution of 20 and 40 mM. The solution is deposited directly onto the SiNW substrate. The solution-coated substrate

is annealed at 100 C in air fo5 five minutes, followed by 550 °C in air for one hour. Though this method has been used before to form silicon/hematite core/shell structures on vertical SiNW arrays[24], the randomly aligned NWs mats provide unique challenges to fabricating uniform core-shell nanostructures.

As seen in Figure 2.3, hematite shells on randomly aligned SiNWs can be synthesized from iron salts. However, unlike with ferrocene pyrolysis, the wires are not individually coated. Higher molarity solutions (40 mM $FeCl_3$, Figure 2.3b) result in hematite accumulating on the substrate surface, creating a webbing effect and coating a large percentage of the NWs together. The core/shell NWs that are individually coated have a hematite radius average of 43 ± 9.7 nm. The synthesis using 20 mM $FeCl_3$ (Figure 2.3a) results in a webbing effect to a lesser degree, but the shell thickness is non-uniform with an average of 22 ± 14 nm. the lack of control over shell thickness and large degree of inter-wire coupling make wet chemical synthesis non ideal for the fabrication of silicon-core hematite-shell nanowire structures.

2.4   Vapor Phase Synthesis from Ferrocene

2.4.1   Hematite Deposition on Planar Substrates

While hydrothermal synthesis of hematite from iron salts provide an inexpensive and straight-forward deposition process, it is not suitable for all substrates. For example, iron (III) salts are highly reactive with many metals, and in solution have acidic byproducts HCl and HNO_3. Additionally, as demonstrates, achieving a uniform hematite film via the hydrothermal method on hydrophobic substrates such as silicon proves challenging. This is especially important when considering a method to synthesize hematite shells on silicon nanowires for solar water splitting applications.[42]

Ferrocene ($FeC_{10}H_{10}$, abbreviated $FeCp_2$) is a metal organic iron (II) compound that can be oxidized to iron oxide, and is less reactive than many iron salt solutions. Pyrolysis of ferrocene has been demonstrated to synthesize iron oxide nanoparticle thin films on FTO and titanium foil.[66-67] This is done by heating ferrocene in a partially-closed container, where the sublimation of ferrocene onto FTO results in partially oxidized iron oxide (Fe_2O_{3-x}) nanoparticles, arranged as a thin film of 20 nm thickness, coated in a 2 nm carbon film.[66] While this method has been demonstrated on FTO for these partially oxidized iron oxide films, the controllability of the particle size, film thickness, and usability on a variety of substrates is explored herein.

Silicon and specifically Si NWs have previously been demonstrated to decrease the overpotential needed to perform the water oxidation reaction.[42] In this section, ferrocene pyrolysis is used for synthesizing hematite thin films growth on planar silicon wafers and randomly aligned silicon nanowires. The methodology used is detailed as follows:

Solid ferrocene (98%, Sigma Aldirch) is placed beside the substrate (FTO, Si, Si NW) on a quartz plate and covered with a quartz top (total container volume 30 mL). The reaction vessel is heated to $500°$ C for 1 hour. The substrate is removed from the hot plate and annealed in air at $750°$ C for one hour. Post annealing, the substrate cools naturally to room temperature, is removed from the furnace and characterized.
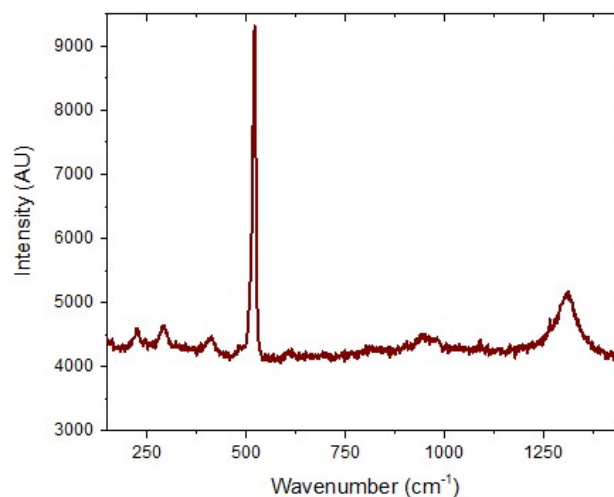
Figure 2.4 Raman spectrum of hematite derived from ferrocene annealed at 600° C for 30 minutes on silicon substrate.

Structural characterization using Raman spectroscopy (Figure 2.4) depicts peaks corresponding to hematite's vibrational transitions: 224, 244, 294, 402, 614 and 1300 cm^{-1}, in agreement with the reference spectra for hematite.[47] The absence of a strong peak at 660 cm^{-1} is indicative of a lack of iron (II) oxide present in the film, making it inconsistent with Fe_3O_4 or FeO.[45] This is of particular importance for this synthetic method as Ferrocene is an iron (II) molecule, and only the iron (III) oxide α-Fe_2O_3 is photocatalytically active. The absence of a strong peak at 1100 cm^{-1}, which would correspond to the Fe-C_5H_5 ring deformation vibration, suggests all ferrocene has decomposed and oxidized. The sharp peak at 520 cm^{-1}, overlapping a hematite A_{1g} mode, and broad peak at 925 cm^{-1} are contributed by the Si substrate.

Based on the mechanism of ferrocene vapor deposition to hematite determined by *Deng et al.*,[68] this procedure is determined to sythensize hematite via a two-step process:

$$Fe(C_5H_5)_2 + O_2 \rightarrow Fe_2O_{3-x} + C_{(s)} + CO_2$$

$$Fe_2O_{3-x} + O_2 + C \rightarrow \alpha \cdot Fe_2O_3 + CO_2$$
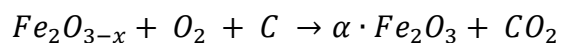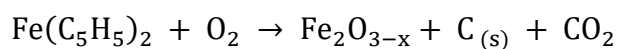
In step one, the ferrocene vaporizes and decomposes, coating the surface of the substrate and the reaction chamber. The partial oxidation of ferrocene (Fe_2O_{3-x}) is due to the limited oxygen supply in the reaction chamber.[66] In step two, when the sample is annealed at 750° C in air, the iron oxide reacts with the oxygen in the air, burning off any residual carbon and allowing for synthesis of fully oxidized hematite.
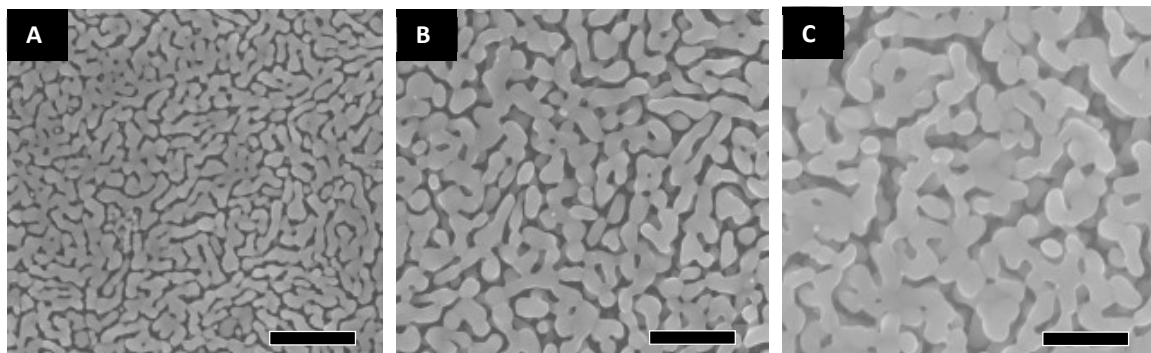
Figure 2.5 SEM images of hematite thin films on silicon substrates. Films synthesized from ferrocene precursor amounts of: (a) 0.015g, (b) 0.025 g, (c) 0.10 g. Scale bars 500 nm.

To observe the morphology of the resulting film, structural characterization is performed using SEM. It is observed that the thin films on Si wafers are an agglomeration of petal-shaped nanoparticles (Figure 2.5). For hematite thin films, particle size and inter-particle spacing is dependent on the concentration of ferrocene precursor in the 30 mL reaction chamber (Table 2.1). Increasing precursor amount from 0.015 g (Figure 2.5a) to 0.025 g (Figure 2.5b) to 0.10g (Figure 2.5) increases both size and spacing of the nanoparticles: when the precursor concentration is quadrupled, for example, the particle spacing is doubled and the particle size increases approxamately1.5 times.

This result mimics previous findings from DA synthesis of hematite from iron chloride. *Wang et al*. concluded that hematite particle size and spacing of NP thin films are dependent on $FeCl_3$ precursor concentration.[37]

Table 2.1 Particle length and particle spacing for ferrocene derived hematite thin films on planar silicon substrates

Ferrocene (g)	Particle Length (nm)	Particle Spacing (nm)
0.10	430 ± 76	70 ± 22
0.025	290 ± 54	35 ± 9.6
0.020	240 ± 38	39 ± 12
0. 015	210 ± 29	24 ± 7.7

In addition to concentration precursor, the substrate material affects the particle size and spacing. For identical synthesis and anneal conditions, it can be observed that hematite films synthesized on FTO are smaller and more closely packed than on planar silicon. On average, for a thin film synthesized from 0.020 g $FeCp_2$, particles are 214 ± 56 nm in length and 23.2 ± 7.6 nm apart, in contrast to 240 ± 38 nm in length and 39 ± 12 nm apart on planar silicon. This indicates that while this method is effective for deposition on hydrophobic substrates such as silicon, the deposition method is not substrate insensitive.
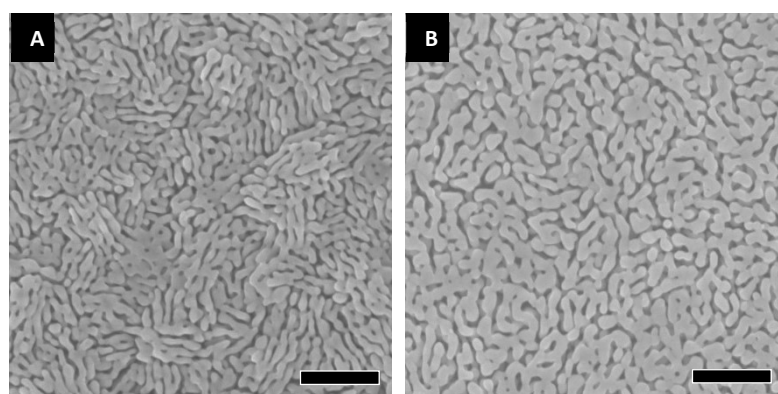
Figure 2.6 SEM of hematite synthesized via ferrocene pyrolysis from 0.020 g ferrocene on (a) FTO and (b) n-type silicon substrates. Scale bars 500 nm.

2.4.2   Self Assembled Hematite Shells on Silicon Nanowires

Si NWs are prepared by CVD, as described in 2.3. The as-prepared substrates are placed in the 30 mL vessel with various amounts of ferrocene (.025 g, .015 g), heated to 500º C and annealed for one hour in air at 750º C. The resulting wafers appeared uniformly red in both cases, with the higher ferrocene concentration resulting in darker a darker color compared to the lower concentration ferrocene sample. SEM images reveal NWs wrapped by hematite particles, formed as a nearly continuous shell (Figure 2.7).

Similar to the thin film samples, the dimensions and continuity of hematite shells on Si NWs are dependent on the ferrocene concentration. The core-shell structures derived from .025 g $FeCp_2$ had an average hematite radius of 135 nm (Figure 2.7c, d) ; while .015 g $FeCp_2$ yielded shell radii of 50 nm (Figure 2.7a, b). The average standard deviations in the NW radius are similar to the standard deviation of the average Si NW radius. Additionally, the size of the hematite nanoparticles composing the shell is linearly dependent on the precursor concentration, and the smaller precursor concentration resulted in a more continuous thin film.

The hematite thickness in the core-shell structures is essential to both its optical and electrical properties. Much like the hematite thin films, the core/shell structures with thicker shells are expected to absorb more visible light, but have poor charge separation. Therefore, one would expect the 50 nm shells to perform as better photoanodes than the corresponding core/shell NW with thicker, more porous shells.
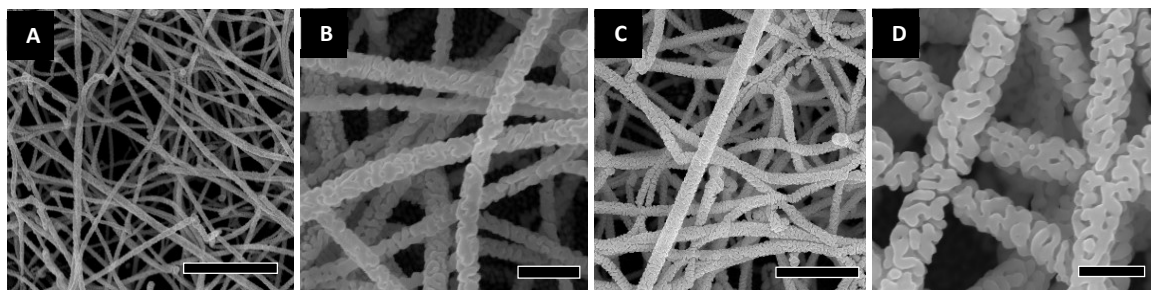
Figure 2.7 Silicon-Hematite Core-Shell nanowires synthesized using (a, b) 0.015 g FeCp$_2$ and (c, d) 0.025 g FeCp$_2$. Silicon NW diameters are 50 nm; scale bars are 3 μm (a, c) and 500 nm (b, d).

It is noteworthy that in all cases studied herein, the shells formed around the NWs via solution deposition (2.3) are less porous than those produced by ferrocene pyrolysis, and NP porosity is likely to encourage recombination. However, despite the larger inter-particle-spacing of ferrocene derived hematite, there is less inter-wire coupling. Separate NWs should facilitate of charge transport and result in less electron/hole recombination as the holes move to the surface and electrons are collected in the silicon.

It is worth mentioning the limitations of the ferrocene pyrolysis method. First, it must be conducted at or above 249° C, the boiling point of ferrocene, which may be unsuitable for material systems that are sensitive to oxidation or have lower melting points. Unlike hydrothermal synthesis, the hematite cannot be doped with transition metals during the synthesis. Though this may be overcome via post-deposition doping such as with titanium[67], this may not be suitable for a wide range of dopants. While ferrocene pyrolysis is a beneficial synthesis method compatible with hydrophobic and 1-dimsnsional nanostructured substrates, chemical synthesis from iron salts is advantageous for hematite thin films on transparent conducting oxide substrates, such as FTO.

2.5   Atomic Layer Deposition with Ferrocene and Oxygen Precursors

As discussed in 1.4, ALD is a unique synthesis approach for a wide variety of thin film materials. ALD hematite films alone do not typically have the highest photocurrent densities compared to other synthesis methods, in part due to anisotropic charge transport though the bulk of the hematite film.[35, 40-41] Therefore, the value in ALD is in depositing uniform thin films with that can be grown with precise thicknesses, which can help design the best PEC water splitting systems. For example, silicon-metal-hematite core-multishell nanowires where the metal is gold, silver or aluminum demonstrate the best photocurrent density improvement with hematite shell thicknesses of 30, 35 and 40 nm respectively.[21] Deviating from the ideal hematite thickness, the plasmon enhancement is less influential and therefore ideal photocurrents will not be achieved. Additionally, ALD results in conformal coverage over high aspect ratio nanostructures, making it ideal for coating NWs uniformly.

Ferrocene is a common and inexpensive iron precursor and several ALD recipes for iron oxide and hematite films via ferrocene have already been developed.[39-40] To oxidize ferrocene, ozone is used as neither molecular oxygen or water alone are sufficient to oxidize ferrocene and begin the ALD reaction. However, as PE-ALD opens the door to using precursors with high thermal and chemical stabilities, high energy oxygen plasma may be a suitable precursor.

Here, the ALD growth of iron oxide films is achieved using ferrocene and oxygen plasma. The effect of oxygen plasma exposure time and post deposition annealing are observed.

ALD was performed on silver foil and silicon substrates. The ALD conditions were as follows: 200° C chamber temperature, ferrocene exposure time 12 s (Figure A.4), purge

8 s, 300 W oxygen plasma exposure time is varied, followed by a 5 second purge, thus

completing one ALD cycle. The films are then annealed in air for 2 hours at 600^0 C.
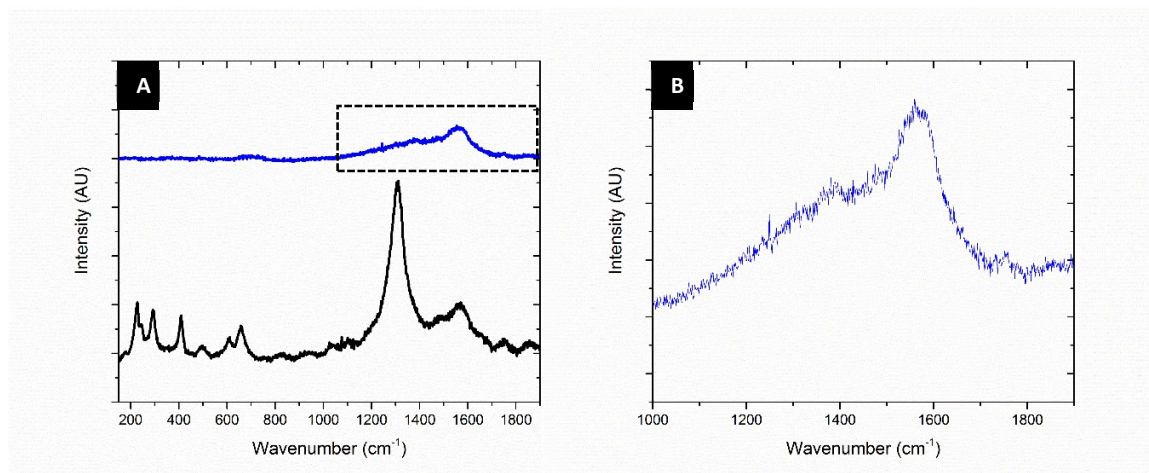
Figure 2.8 Raman spectra of ALD iron oxide using 20 second oxygen plasma (a) as prepared (blue) and after 600 C anneal (black) (b) as prepared sample from 1000-1900 cm^{-1} depicted by black box in (a)

Raman spectroscopy is performed to characterize the resulting thin films after a 400

cycle deposition. For oxygen plasma exposure time of 20 s (Figure 2.8a), the Raman

spectrum of the as prepared samples show no peaks consistent with hematite (blue). Closer

examination of the region 1000-1800 nm reveals Raman peaks located at 1584 and 1563

cm^{-1}, consistent the presence of amorphous carbon (Figure 2.8b).[69] After annealing (black),

the Raman spectrum has peaks consistent with the α and γ Fe2O3 phases, indicating a

mixed-phase iron oxide film.[47] The sharp band at 657 cm^{-1} is assigned to Fe^{2+} inclusion in

the lattice.[45-46] Therefore it is concluded that 20 s, 300 W oxygen plasma does is not

sufficient to break all C-C bonds of the ferrocene precursor, which prevents the full

oxidation of the Fe^{2+}.

Repeating the same ALD parameters and increasing the oxygen plasma exposure

time to 40 s, the Raman spectrum demonstrates no evidence of carbon-carbon bonding in

the thin film (Figure 2.9, blue). After anneal, only peaks consistent with hematite are observed (Figure 2.9, black). The absence of a strong peak near 660 cm^{-1} the majority of Fe^{2+} is oxidized. Therefore, after anneal, the iron (II) precursor is fully oxidized to iron (III) and film is majority α-phase. Ellipsometry is performed to confirm a growth rate of 0.450 angstrom/cycle (Figure A.4), resulting in sub-nm control of the film thickness for the fully oxidized iron oxide product.
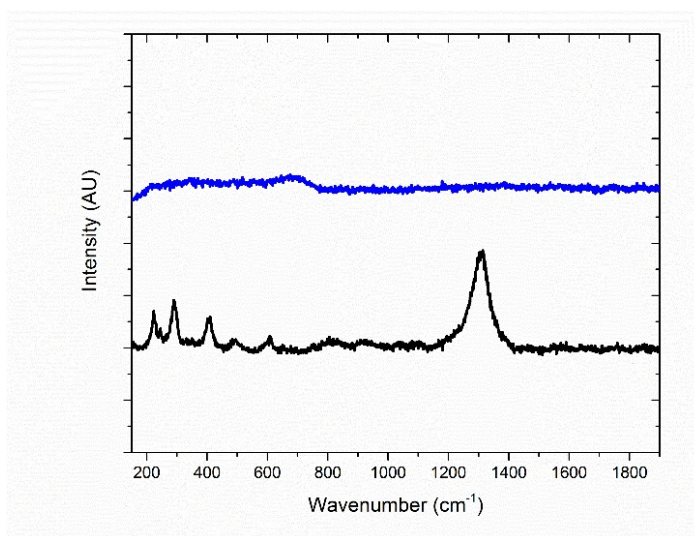
Figure 2.9 Raman spectra of ALD iron oxide using 40 second oxygen plasma (a) as prepared (blue) and after 600 C anneal (black)

It is noteworthy that the Raman spectrum for the as-deposited films does not directly conclude whether or not the α-phase iron oxide (hematite) has been deposited. The anneal in air my serve two functions (1) to fully oxidize the film to iron (III) oxide and (2) improve the crystallinity. To best determine the effect of the air anneal, the as prepared films is annealed in vacuum at 600 C for two hours, and the Raman spectrum compared to the as prepared and air-annealed films.
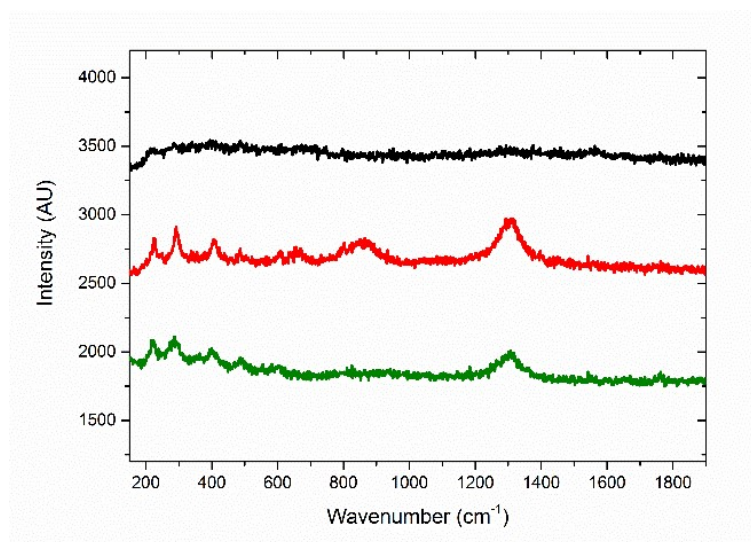
Figure 2.10. Raman spectra comparing ALD iron oxide as prepared (black), after vacuum anneal (red) and after air anneal at 600° C for 2 hours

As seen in Figure 2.10, the vacuum annealed sample (red) and the air anneal sample (green) contain seven peaks consistent with hematite: 224, 249, 292, 404, 607 and 1305 cm⁻¹. For the vacuum annealed sample, the disorder induced peak at 657, which disappears upon anneal in air, may represent the presence of iron (II) from wustite or maghemite.[45-46] Finally, the broad peak at 850 cm⁻¹ is inconsistent with a-phase iron oxide. Therefore, as-prepared film is of mixed iron oxide phases. The lack of Raman signal in the as-prepared sample (black) is due to low crystallinity, and an anneal in an oxidizing environment such as air is needed both the increase the crystallinity and fully oxidize the iron oxide to hematite.

Finally, we observe the hematite deposition on Si NWs prepared by CVD. The resulting Si/hematite is orange in color after the ALD synthesis and subsequent anneal in air. SEM is employed to observe the morphology of the Si and Si/hematite NWs (Figure 2.11). Under SEM, the hematite coating is visible and textured, not atomically smooth, making the core/shell NWs slightly rougher than their bare counterpart (Figure 2.10a). This

is similar in appearance to hematite shells on Si NWs produced by ALD using tert butyl ferrocene and water.[42] It is observed that the ALD method successfully coats each wire are conformally and individually.
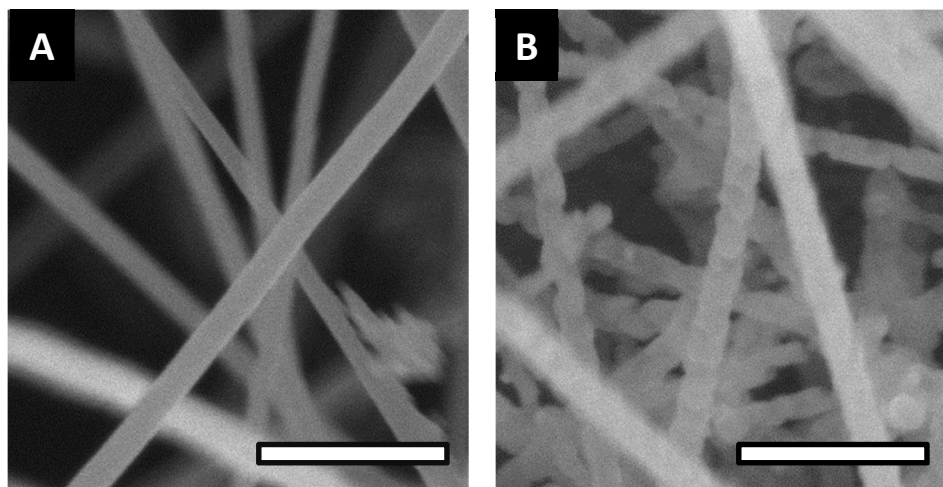
Figure 2.11 SEM of (a) bare silicon nanowires and (b) silicon/hematite core shell nanowires. Hematite coating synthesized by PE-ALD. Scale bars 500 nm.

Ferrocene and oxygen plasma are suitable ALD precursors for the synthesis of iron oxide. The oxygen plasma time must be sufficient to fully break the C-C bonds in the ferrocene precursor to allow full oxidation of the iron oxide. Here, we found that to be a 40 second exposure of 300 W oxygen plasma. When prepared at 200° C, the as prepared samples are mix-phase and require a high temperature anneal in an oxidizing environment to convert to α-Fe_2O_3 to be suitable for water splitting applications. This synthesis method results in conformal coverage of high aspect ratio silicon nanowires.

2.6   Summary

There are a variety of parameters to consider for synthesizing photoactive hematite nanomaterials. Properties important to the photoactivity include nanoparticle morphology,

film thickness, donor density concentration and doping ability and material design, which are all affected by the synthesis method.

This can be accomplished by low-cost bench top deposition methods. Reviewed here, chemical synthesis methods from iron salts, such as hydrothermal synthesis, can deposit hematite films with a variety of morphologies and allows for easy incorporation of dopants (Figure A.1). However, it is limited in its ability to conformally and individually coat 1-D nanostructures with precise thicknesses. High temperature decomposition of ferrocene is demonstrated here to be compatible with hydrophobic substrates: the morphology on Si wafers is similar, though not identical, to that on FTO. Importantly, the nanoparticle size and spacing can be controlled by the concentration of ferrocene precursor. This method also allows for a facile, low-cost method of self-assembling hematite nanoparticles on 1D nanostructures, in which the hematite shell radius can be controlled by the precursor concentration.

Alternatively, an ALD approach using ferrocene and oxygen plasma precursors is studied for the synthesis of ultra-thin hematite films and nm-scale thickness precision, allowing for uniform coating of silicon and silicon nanowires. The plasma time is essential to fully oxidizing the ferrocene precursor and eliminating resulting carbon contamination. Ultimately, it is demonstrated that hematite can be produced by this method with a 40 second, 300 W oxygen plasma, which produces mix-phased iron oxide. An anneal in air is required to fully convert this product to the α-phase.

CHAPTER 3.   UNDERSTANDING GRAPHENE AS AN OVERLAYER ON NANOSTRUCTURED HEMATITE PHOTOANODES FOR IMPROVED SOLAR WATER SPLITTING

The contents of this chapter have been reprinted or adapted with permission and were originally presented in *Materials Today Energy* (*Mater. Today Energy*. 2018, 8, 8-14)[70] in collaboration with Professor Dunwei Wang (Boston College) and Professor Yat Li (UC Santa Cruz). The titanium doped hematite for these experiments was produced by Mingyang Li; Solar Electrical Impedance Spectroscopy (EIS) and Intensity Modulated Photocurrent Spectroscopy (IMPS) experiments were conducted with Wei Li.

3.1   Introduction

To overcome hematite's poor oxygen evolution kinetics and high rates of recombination, much research has gone into modifying hematite's surface. While coating the hematite surface with inorganic materials has gained most attention, and has been shown to result in passivated surface states and improve charge transfer rates, carbon-based overlayers remain less investigated and less well understood.

Carbon overlayers have shown great promise for improving the photocurrent density in hematite photoanodes. Hematite with carbon coatings formed via ferrocene pyrolysis and electrodeposition techniques show four times and three times improvements in photocurrent density, respectively.[66, 71-72] Along with carbon coating the hematite surface, these synthesis techniques also increase the donor density in the hematite by one to two orders of magnitude. The increase in donor density makes the role of the carbon coating difficult to fully understand: *Deng et al*[66] attributes the PEC enhancement entirely to the increased donor density while reports from *Wang et al.*[71-72] attributes the PEC enhancement to carbon acting as a passivation layer. Additionally, synthesis dependent coating techniques such as these do not present a general technique to modify a catalytic surface with already optimized donor densities and morphologies.

The carbon derivative reduced graphene oxide (rGO) can improve hematite's photocurrent density when used as an overlayer.[73-74] These studies imply that the rGO makes the surface more conductive, which results in improved PEC properties. Alternatively, work from *Zhang et al*.[75] examined FTO/hematite nanowires wrapped in rGO and found that rGO acts as a co-catalyst, improving the charge transfer. The conflicting explanations in the literature point to the difficulty of identifying the mechanism behind photocurrent density enhancement.

While rGO allows for easy processing, it also has drawbacks as a carbon coating method; rGO has reduced conductivity due to surface functionality and high defects intrinsic to the process of reducing the graphene oxide precursor.[76] Additionally, an overlayer of rGO is made of micro- and nano-size flakes, and therefore the conductivity is controlled by the rGO inter-particle contacts.[77] To compensate for this, studies of rGO overlayers use multiple layers of rGO flakes on the electrode surface, which could interfere with optical absorbance in the hematite and limit its practical applications.

A single atomic layer of carbon (single layer graphene or SLG) potentially has more favorable properties than rGO and amorphous carbon for PEC applications. As it is transparent, absorbing approximately 2% of light over the entire solar spectrum, SLG will not significantly interfere with the absorption in the hematite electrode. Additionally, a single graphene sheet has high mobility charge carriers, demonstrating charge carrier motilities of $\mu = 10^5$ cm^2/(Vs), even in the presence of many defects,[78-80] and charge carriers can travel thousands of interatomic distances without scattering.[81-82] SLG is chemically inert and therefore resistant to oxidation in air and electrochemical environments, specifically previously showing photoelectrochemical stability as an overlayer on water

splitting silicon photoanodes.[83-85] One additional advantage is that graphene can be transferred to a variety of substrates, having the potential to act as a surface modification layer for a wide range of photocatalytic materials and morphologies. These are beneficial overlayer characteristics for circumventing the poor surface electrical properties of hematite.

This chapter demonstrates that conformal that single layer graphene as an overlayer enhances the photocurrent density of stable photoanodes such as titanium doped hematite. Importantly, we performed detailed solar electrical impedance spectroscopy (EIS) and intensity modulated photocurrent spectroscopy (IMPS) to identify and understand the mechanism of photocurrent improvement. Using solar EIS, the changes in charge movement and storage on hematite's surface are observed. Using IMPS, the kinetics of the photoanode surface are measured directly and show a decrease in charge recombination at the surface of hematite with graphene. Furthermore, these results suggest that a single layer graphene overlayer can be a general strategy to improve the surface of metal oxide photoanodes.

3.2   Photoanode Fabrication

Titanium doped hematite is synthesized similar to the previously described hydrothermal synthesis method.[37, 60-61] It has been shown that hematite prepared using this method demonstrated better photocurrent density compared to other deposition methods. Specifically, hematite is prepared on fluorine doped tin oxide (FTO) substrates using ferric chloride using sodium nitrate and tetrabutyl titanate in an autoclave. The FTO substrates are placed into the autoclave for one hour at 120° C. The substrates are removed, washed

with DI water and annealed in air at 550° C for 30 minutes, followed by a high temperature air anneal at 700° C for 20 minutes.

For the TiO_2 samples, titanium oxide (anatase) thin films are synthesized using PE-ALD, similar to a previously described thermal method.[17, 86] The substrate temperature was held constant at 225° C and the titanium isopropoxide precursor is heated to 70° C. One ALD cycle consists of the following: titanium isopropoxide is pulsed for 200 ms, followed by a 10 second evacuation of 20 sccm argon; next, the chamber is exposed to 300 W oxygen plasma (5 sccm oxygen to 5 sccm argon) for 20 seconds, followed by a second five second evacuation with 20 sccm argon. This was repeated for 550 cycles, corresponding to a 30 nm deposition. The samples were removed from the reaction chamber and immediately annealed in air at 425° C for two hours. For the hydrogen treated samples, an additional anneal was performed at 250° C for thirty minutes in a under 50 sccm hydrogen, similar to a previously described method.[87]

Single layer graphene (SLG) is synthesized via chemical vapor deposition (EasyTube 3000, First Nano). As reported[88], the graphene growth is performed at 1035° C using methane (20 sccm) and hydrogen (10 sccm) on a copper foil substrate. The SLG is transferred onto the hematite/FTO substrate using a previously reported transfer method.[88-89] The graphene is coated in PMMA and the back-side of the substrate is cleaned with oxygen plasma. The copper foil is then etched using an aqueous solution of ammonium persulfate and the remaining graphene is transferred to the hematite substrate. The graphene coated hematite is baked at 70° C for 30 minutes, and 180° C for 30 seconds. To remove the PMMA, the substrate is submerged in acetone for 30 minutes. To remove residual PMMA, the graphene coated hematite is annealed for one hour at 300°C. Typically,

this final anneal would be performed in vacuum or in an inert/reducing atmosphere. However, to avoid reducing or creating oxygen vacancies in the hematite and maintain consistency between the graphene-coated and bare samples, PMMA residue removal is performed in air.

Hematite and anatase thin films on FTO are fabricated into electrodes by attaching copper foil to the exposed FTO using conductive silver paint. Non-conductive epoxy was used to seal off the edges and expose an active area of $0.25–0.40$ cm^2.

3.3   Structural Characterization

To confirm the synthesis of nanostructured hematite, SLG and successful transfer of SLG to hematite, Raman Spectroscopy (Renishaw Raman, 633 nm excitation laser) is performed (Figure 3.1a). Eight peaks consistent with hematite (red) are observed: 220 (A_{1g}), 234 (E_g), 285 (E_g), 403 (E_g), 497 (A_{1g}), 602 (E_g), 650 (E_u) and 1317 (two magnon scattering) cm^{-1}.[48] Graphene was grown via CVD and transferred to SiO$_2$ (black), where bands are observed at 1320 (D), 1574 (G) and 2642 (2D) cm^{-1}. Graphene grown via CVD and transferred to the hematite (blue) has the same eight peaks as the bare hematite in addition to the characteristic graphene G and 2D bands located at 1572 and 2642 cm^{-1} respectively. The presence of all peaks associated with hematite and graphene confirms the graphene transfer process was successful.

The downshift of the G band and the broadening of the G and 2D bands for graphene on hematite as compared to that on the planar SiO$_2$ is consistent with previous studies that demonstrate the strain graphene undergoes upon conforming to nanostructures.[89-92] We expect this interaction between SLG and hematite to be dominated via van der Waals forces, as demonstrated in previous calculations of graphene on SiO$_2$.[93]
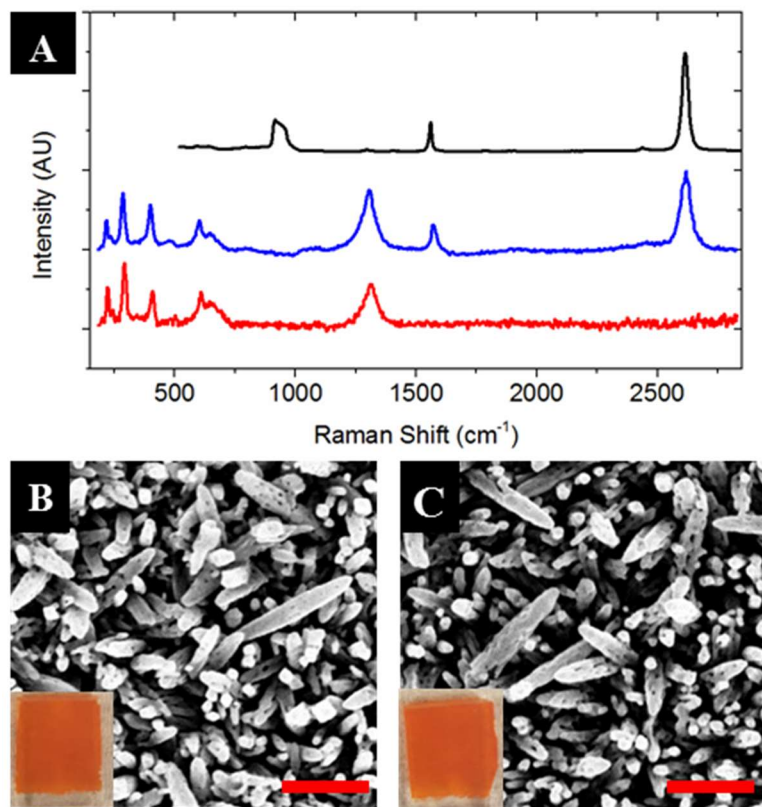
Figure 3.1 (a) Raman spectrum of SLG transferred to SiO_2 (black), bare hematite (red) and SLG transferred to Ti-doped hematite (blue); SEM images of (b) Ti-doped hematite, (c) SLG coated Ti-doped hematite. Scale bars are 500 nm. Insets (b,c): digital photographs corresponding to SEM images.

The intensity ratio of the G band to the 2D band (I_G/I_{2D}) obtained from graphene Raman spectrum of 0.32 (black) on SiO_2 and 0.36 (blue) on hematite is consistent with graphene that is single layer.[94-95] It is worth noting that the graphene D band cannot be resolved for the graphene coated hematite sample as it overlaps with the two-magnon scattering peak in hematite. For the SLG on SiO_2, the disorder-induced D band is low in intensity, with an I_D/I_G of 0.16, indicating that the graphene has only minor defects. This I_D/I_G ratio and the position of the G band at 1574 cm^{-1} for SLG on SiO_2 and 1572 cm^{-1} for SLG on hematite indicate that the graphene is primarily sp^2 and is inconsistent with

amorphous carbon or nanocrystalline graphite.[69, 96] Finally, the transferred graphene is expected to be continuous over the hematite substrate.[89]

To observe the hematite morphology, SEM images were taken of the samples with and without graphene (Figure 3.1 b, c). The synthesized hematite films have a textured, rod-like appearance similar to those previously reported.[60] The graphene transfer results in no apparent change on the nanostructure or visual appearance of the thin films (Figure 3.1 b, c insets).

3.4   Electrochemical Characterization

To evaluate the effect of the SLG overlayer on the photocatalytic properties of hematite, the photocurrent density of the hematite and SLG coated hematite is compared using linear sweep voltammetry (LSV). The photoelectrochemical measurements are carried out in 1 M NaOH using a three-electrode set up: hematite working electrode, Pt-wire counter electrode, and Ag/AgCl reference electrode. Photoelectrochemical analysis is performed using a solar simulator (Newport, Model 69907), an AM 1.5 G filter and 150 W Xenon lamp, calibrated to 1 sun illumination (100 mW/cm^2) and a Solarton Analytical Modulab XM electrochemical station. Linear sweep voltammetry is measured from -0.2 to 0.6 V$_{Ag/AgCl}$. All voltages are converted from Ag/AgCl to the reversible hydrogen electrode (RHE) scale using the Nernst equation:

$$E_{RHE} = E_{Ag/AgCl} + (0.059)(pH) + E^0_{Ag/AgCl}$$

Where E$^0_{Ag/AgCl}$ = 0.1976 V, E$_{Ag/AgCl}$ is measured experimentally against the Ag/AgCl reference electrode, and (pH) is the pH of the 1 M NaOH electrolyte.

Under 1 sun illumination, the photocurrent density of bare hematite is measured with and without the graphene overlayer (Figure 3.2). Comparing photocurrent densities

of the bare hematite with (solid blue) and without (dashed blue) the SLG overlayer, it is observed that the LSV curves are similar in their shape and onset voltage of 0.9 V_{RHE} (Figure 3.2a). However, hematite with the SLG overlayer has a greater photocurrent density from 1.0 to 1.6 V_{RHE}. The result of this is at 1.23 V_{RHE}, the hematite with the SLG overlayer shows a photocurrent density 1.61 times greater than bare hematite. This is comparable to the 1.52 and 1.47 times increase seen by optimizing the thickness of rGO overlayers on nanostructured hematite.[73-74]
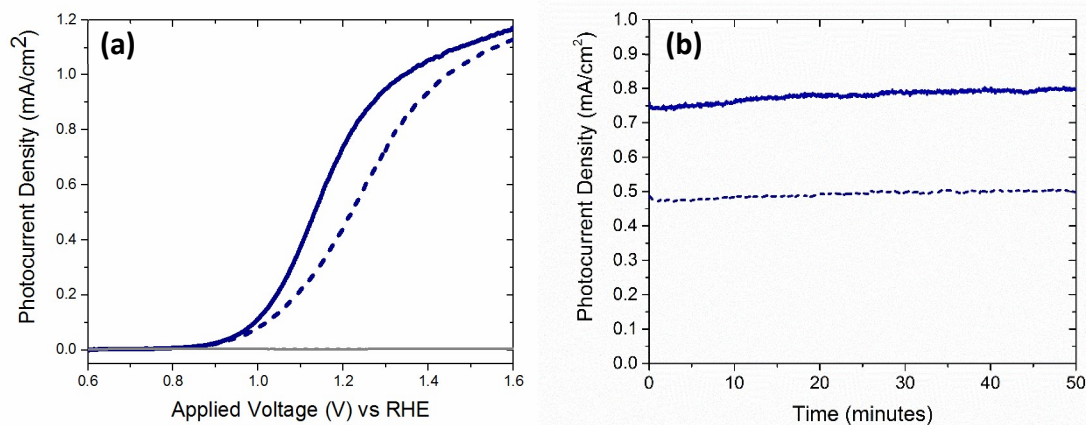
Figure 3.2 **(a)** Representative linear sweep voltammetry results comparing photocurrent densities of titanium doped hematite under one sun illumination (blue) and in the dark (gray) and (b) photocurrent density over time at 1.23 V_{RHE} for samples with (solid lines) and without (dashed lines) SLG overlayer.

The enhancement caused by the graphene coating shows good reproducibility despite sample-to-sample variation: at 1.23 V_{RHE}, bare hematite demonstrates an average photocurrent density of 0.46 ± 0.068 mA/cm^2; SLG coated hematite demonstrates a photocurrent density of 0.75 ± 0.094 mA/cm^2. To ensure the photocurrent density is stable over time, chronoamperometry is performed (Figure 3.2b). A slight rise in photocurrent density observed over 50 minutes of irradiation is demonstrated in both hematite with and without the graphene overlayer. As this occurs in both the SLG coated and bare hematite

samples, it is attributed to sample heating. This indicates that the SLG overlayer does not degrade during the oxygen evolution reaction.

Understanding the mechanism underlying the enhancement caused by the SLG overlayer is crucial for designing effective overalyers as a performance improvement strategy for photoelectrocataysis. To this end, we first determine if and how the SLG overlayer impacts the catalytic properties at (1) the surface-electrolyte interface and (2) depletion region. Therefore, the electrochemical properties of hematite with and without the SLG overlayer were investigated using electrical impedance spectroscopy (EIS).
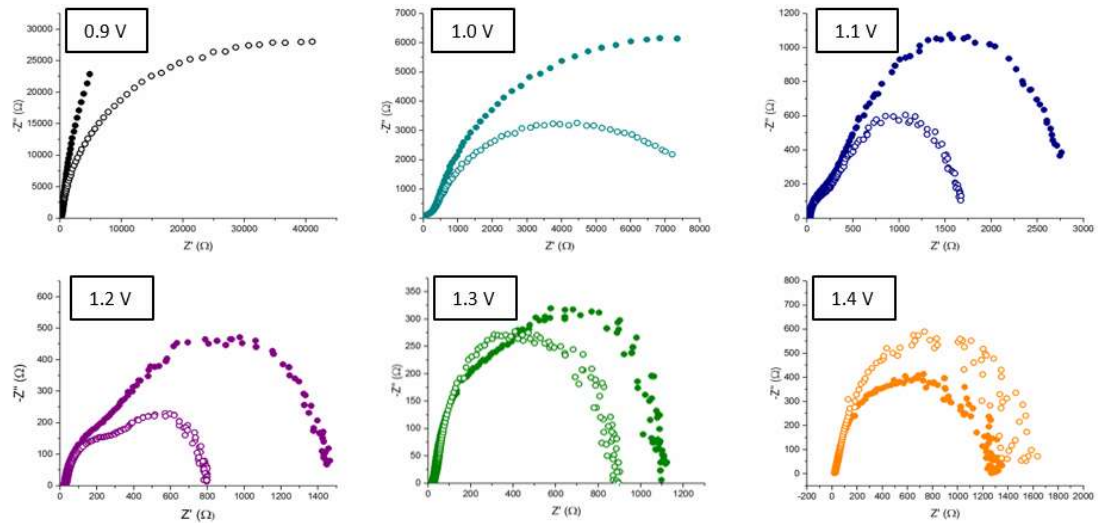
Figure 3.3. Nyquist plots from solar EIS analysis for titanium doped hematite with (open circles) and without (closed circles) a single layer graphene overlayer.

Nyquist plots (Figure 3.3) are constructed from the EIS analysis under 1 sun illumination, sweeping the frequency from 100,000 to 0.01 Hz, and are analyzed using an equivalent circuit. While we acknowledge that there are other fitting methods for this data,[97] we chose a 2RC equivalent circuit to model the surface and depletion region RC components of the photoanode (Figure 3.4a). This equivalent circuit was chosen because

for highly doped and nanostructured hematite, it cannot be assumed that the capacitance of the depletion region and surface are the same order of magnitude. Using the equivalent circuit with two RC elements in series accounts for processes occurring at both the surface and semiconductor bulk.[15, 98] The capacitance and resistance of the depletion (space charge) region are modeled by C_{SC} and R_{SC}, respectively. The RC components of the surface-electrolyte interfaces are the Helmholtz capacitance (C_H) and the charge transfer resistance (R_{CT}). R_s represents the series resistance.

EIS data is measured and analyzed from 0.9 to 1.4 V_{RHE}. C_H is plotted as a function of applied voltage to observe the change in bare and SLG coated hematite (Figure 3.4b). In the presence of the SLG overlayer at 1.2 V_{RHE}, C_H increases from 72.1 μF (blue squares) to 98.2 μF (open squares). This indicates that the charge carriers (holes) are collecting on the surface of the graphene/hematite electrode, meaning the graphene overlayer is more effective than bare hematite at storing photo-generated holes, especially at lower applied voltages.

R_{CT} is plotted over the same voltage range. R_{CT} is reduced by at least a factor of two in the presence of the SLG overlayer in the range of 0.9 to 1.3 V_{RHE} (Figure 3.4c). Specifically, at 1.2 V_{RHE}, R_{CT} decreases from 1005 Ω (red diamonds) to 456.7 Ω (open diamonds). This indicates that there is more charge movement on the graphene/hematite surface compared to bare hematite. It is worth noting that despite this overall trend, Figure 3.4c reveals that the R_{CT} for the bare Ti-doped hematite is 667 ± 40.1 Ω and the R_{CT} for SLG coated Ti-doped hematite is 753 ± 72.2 Ω. Therefore, statistically, the values for R_{CT} are equal at 1.4 V. An overall decrease in charge transfer resistance is consistent with previously demonstrated systems of rGO overlayers on hematite, which demonstrated an

R_{CT} of 357.6 Ω for bare hematite to 337.9 Ω for rGO coated hematite thin films at 0.05 V_{RHE} under dark conditions.[74] The greater decrease in R_{CT} in the presence of SLG seen here suggests that SLG more positively affects the hematite surface compared to rGO.
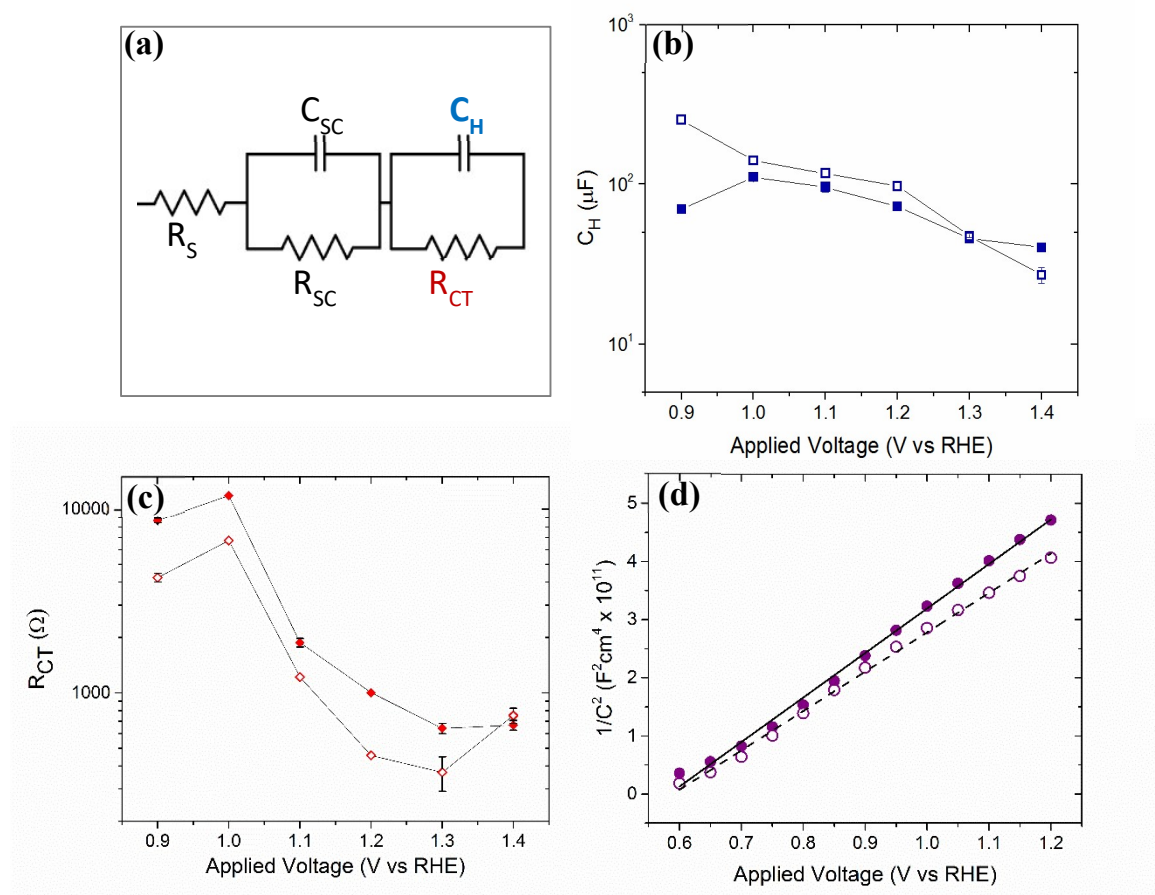
Figure 3.4 Electrical Impedance Spectroscopy: (a) equivalent circuit used as a model for the EIS Nyquist Plots (b) Helmholtz capacitance (C_H) (c) charge transfer resistance (R_{CT}). (d) Mott-Schottky plot obtained at 10 kHz frequency under dark conditions. All plotted for titanium doped hematite with (open markers) and without (filled markers) SLG overlayer

Since there is no significant change in the space charge resistance or capacitance in the presence of SLG over the range of 0.9-1.4 V_{RHE} (Figure A.5) the graphene overlayer does not affect the bulk of the thin film significantly and is therefore a surface-only

modification technique. This is further confirmed by the Mott-Schottky analysis (Figure 3.4d). The donor density (N_d) is calculated using the following equation:

$$N_d = \frac{2}{e_0 \varepsilon \varepsilon_0} \left(\frac{\partial C^{-2}}{\partial V} \right)^{-1}$$

Where e_0 is the electron charge, ε is the complex dielectric constant of hematite (80), ε_0 is the permittivity in vacuum and $\left(\frac{\partial C^{-2}}{\partial V} \right)$ is the slope of the Mott-Schottky plot.[99] From this, it is determined that N_d of the bare and SLG coated hematite are 1.12 x 10^{18} cm^{-3} and 2.75 x 10^{18} cm^{-3}, respectively, confirming that the SLG overlayer does not significantly affect the donor density of the photoanode material. This is unlike carbon-coated hematite systems synthesized via ferrocene pyrolysis or electrodeposition, where the carbon overlayer significantly increases the donor density, which may contribute the increase in photocurrent density, making it difficult to isolate the impact of the overlayer.[66, 71-72] In this SLG coated hematite system, the decreased charge transfer resistance is likely a main contributor to increased photocurrent density seen in hematite photoanodes with the SLG overlayer.

Though it is a standard technique for understanding the properties of semiconductor catalysts, EIS only gives partial insight into how exactly the SLG overlayer is improving hematite's photocurrent density, and has been reported previously to be most useful for demonstrating the modes of charge storage in hematite photoanodes.[100] Often, reduced charge transfer resistance is attributed an increase in the rate of charge transfer. However, it may also or instead be due to a decrease in the rate of charge recombination or increased charge mobility across a surface. With the results from EIS alone, it is impossible to conclude which mechanism best represents a given system.

3.5   Kinetic Measurements

To better understand the kinetic mechanism behind the reduced resistance of the oxygen evolution reaction measured by EIS, we employ Intensity Modulated Photocurrent Spectroscopy (IMPS) to directly measure the kinetics of the photoanode surface. IMPS, first demonstrated by *Peter et al.*[101], is a technique that involves measuring frequency responses of the photocurrent to small modulations in the illumination intensity. Using this information, rate constants for electron transfer and recombination are obtained. IMPS has been previously used to observe hematite and the effect of overlayers on hematite.[102-104] Here, for hematite photoanodes, IMPS is measured using a 405 nm illumination with 10% light modulation
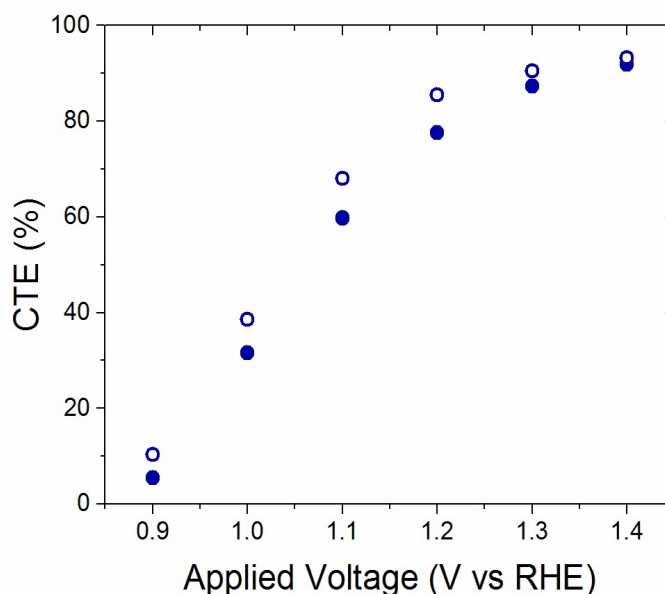
Figure 3.5 IMPS results depicting charge transfer efficiency (CTE) for titanium doped hematite with (open circles) and without (filled circles) SLG overlayer.

IMPS is used to measure and compare the charge transfer efficiency (CTE), charge transfer rate and recombination rate on the hematite surface with and without a graphene

overlayer. The results demonstrate an increase in the charge transfer efficiency in the range of 0.9-1.4 V_{RHE} for SLG coated hematite compared to bare hematite (Figure 3.5). At 1.2 V_{RHE}, CTE is 8% higher for graphene coated samples compared to the bare hematite. Consistent with the R_{CT} measurements, the CTE begins to converge at 1.4 V_{RHE}. Based on CTE, the rate constants for charge transfer (k_{tran}) and recombination ($k_{rec)}$ are calculated and related by:

$$CTE = \frac{k_{tran}}{k_{tran} + k_{rec}}$$

The SLG overlayer affects both rate constants (Figure 3.6). The rate of charge transfer, $k_{tran,}$ decreases in the presence of SLG, for instance from 244 sec^{-1} to 76 sec^{-1} at 1.2 V_{RHE} (Figure 3.6a). The rate of recombination, k_{rec}, decreases as voltage increases for Ti-doped hematite with and without the graphene overlayer (Figure 3.6b). Over all observed voltages, k_{rec} is lower for the graphene coated samples compared to the bare samples, specifically dropping from 71 s^{-1} to 13 s^{-1}, or 82%, at 1.2 V_{RHE}. Though the magnitude of k_{rec} decreases as voltage increases, the relative gap between bare and SLG coated k_{rec} the two does not decrease. This can be observed more clearly when the y-axis is plotted on a logarithmic scale (Figure 3.6c). From this information, we conclude that SLG as an overlayer on hematite suppresses charge recombination and inhibits charge transfer at the surface of the photoanode. This result is similar to previous studies on NiFeO and cobalt oxide overlayers on hematite, both of which conclude that suppressing the recombination rate results in more significant increases to the CTE, and therefore the photocurrent density, than a change in the charge transfer rate.[102, 104]

Based on the results from IMPS and the data presented herein, we demonstrate that the improved photocurrent density under 1 sun illumination is due to a graphene overlayer

dramatically decreasing the rate of charge recombination at the surface-electrolyte interface, which ultimately improves the charge transfer efficiency of the surface. This is likely due to graphene's high planar conductivity and charge mobility, resulting in an increase yield of holes on the surface of the photoanode to participate in the oxygen evolution reaction.
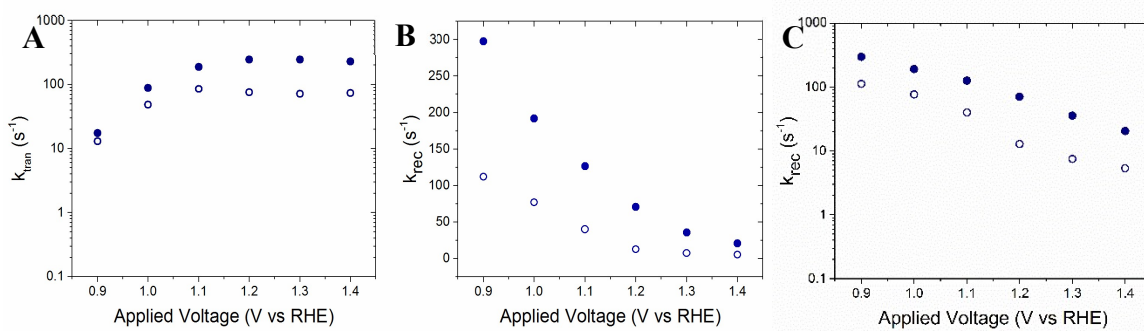
Figure 3.6 (a) Charge transfer rate constant (k_{tran}) (b) charge recombination rate constant (k_{rec}) plotted with a linear y-axis and (c) k_{rec} plotted with logarithmic y-axis. All plotted for titanium doped hematite with (open circles) and without (filled circles) single layer graphene; data measured under light illumination of 405 nm.

3.6 SLG Overlayer as a General PEC Enhancement Technique

To further assess if a single layer graphene overlayer can be used as a general method for improving the surface of metal oxide photoanodes, we investigate its effect on titanium oxide photoanodes. To this end, TiO_2 is deposited on FTO substrates using ALD. After deposition, the TiO_2 photoanodes are annealed at 400° C in air. To further improve the performance, the TiO_2 is annealed at 250° in hydrogen for 30 minutes.

To confirm the synthesis of the TiO_2 and the graphene transfer to TiO_2, Raman spectroscopy is utilized (Figure 3.7a). The bare TiO_2 demonstrates peaks consistent with five Raman active modes: 144 (E_g), 248 (E_g), 395 (B_{1g}), 516 (B_{1g}) and 634 (E_g) cm^{-1}, which are consistent with reference spectra for anatase-phase TiO_2 (black).[105] Similar to graphene

on hematite, the D, G and 2D bands consistent with single layer graphene[94-95] are observed in addition to the anatase signal after graphene transfer (blue).

To observe the effect of the graphene overlayer on TiO_2 photocurrent density, LSV under 1-sun illumination is performed on three samples: anatase TiO_2 (dashed green), hydrogen treated anatase (dashed blue), and hydrogen treated anatase with graphene overlayer (solid blue) (Figure 3.7b). Hydrogen treatment is a common method of improving the photocurrent density in TiO_2. As expected, hydrogen treated TiO_2 demonstrates a higher photocurrent density than untreated TiO_2, likely due to oxygen deficiency in the TiO_2 lattice which increases the donor density in the bulk of the film.[87] At 1.23 V_{RHE} untreated anatase demonstrates a photocurrent density of 30.7 $\mu A/cm^2$ where hydrogen treated anatase photocurrent density is 38.0 $\mu A/cm^2$.

The graphene overlayer further improves on the hydrogen treatment: at 1.23 V_{RHE} SLG coated anatase has a photocurrent density of 46.9 $\mu A/cm^2$, an approximately 1.2 times greater photocurrent density compared to the bare, hydrogen treated photoanode. The photocurrent improvement observed in anatase is smaller than the 1.6 times enhancement is seen in the graphene coated hematite. This likely means that the degree of surface passivation caused by the graphene on hematite is greater than that on anatase. Possibly this is because the surface recombination in hydrogen treated TiO_2 is less than the titanium doped hematite. Even so, the photocurrent density enhancement on both anatase and hematite indicates that SLG overlayers have the potential to be used as a general method for improving surface recombination, and therefore photoelectrochemical performance, of nanostructured metal oxide photoanodes.
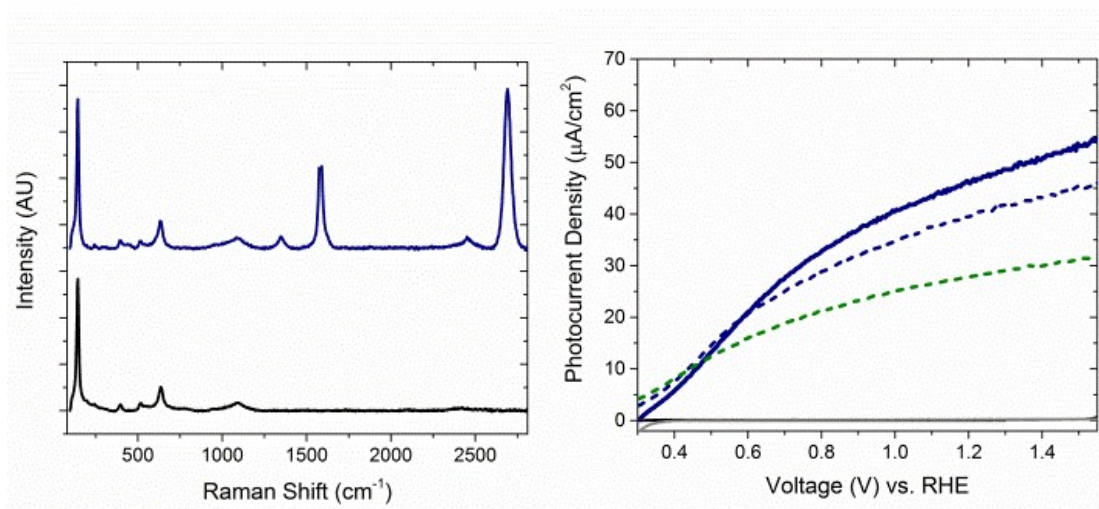
Figure 3.7 (a) Raman spectrum of anatase phase TiO$_2$ with (blue) and with out (black) graphene overlayer; (b) LSV under 1-sun illumination for TiO$_2$ (green dashed), hydrogen treated TiO$_2$ (blue dashed) and hydrogen treated TiO$_2$ with (solid blue) and without (dashed blue) graphene overlayer under and dark conditions (gray)

3.7   Conclusion

In conclusion, single layer graphene grown on copper foils via CVD can be successfully transferred onto doped, metal oxide nanostructured films, and these novel graphene/hematite heterostructures show an increased photocurrent density 1.61 times greater than bare hematite at 1.23V$_{RHE}$. We gained understanding regarding the mechanism through which the graphene overlayer improves hematite's photocurrent density. Through EIS we have demonstrated that the SLG overlayer impacts the RC components at the surface electrolyte interface while not significantly modifying the space charge region. SLG reduces the charge transfer resistance compared to the bare hematite film. Using IMPS, we show an 8% increase in charge transfer efficiency in the presence of the graphene overlayer. The increased CTE and decreased charge transfer resistance results from the reduction in k$_{rec}$. Because IMPS also demonstrates a decrease in k$_{tran}$ in the presence of the SLG overlayer, the decreased charge transfer resistance observed via EIS cannot be

attributed to an increase in the charge transfer rate, but can be attributed to the increased charge transfer efficiency and the decrease in the surface recombination rate. Therefore, CVD grown single layer graphene transferred to nanostructured hematite acts as a passivation layer, and not as a co-catalyst.

From results gathered on both hematite and anatase photoanodes, it is concluded that single layer graphene transferred to photocatalysts has the potential to be used as a general method of improving solar water splitting on metal oxide photoanodes. Future studies are needed to optimize the layer number and quality of graphene overlayers to achieve the best charge transfer rates while maintaining low recombination rates to best enhance the photocurrent density of these photoelectrodes.

CHAPTER 4.   OPTICAL ENHANCEMENT OF PHOTOELECTRODES USING EMERGING PLASMONIC METALS

Photocurrent density simulations for TiN based nanowires presented in this chapter were conducted with and nanowire dimensions were optimized by Katherine Hansen.

4.1   Motivation

A semiconductor's photocatalytic properties rely on electron/hole pairs migrating to the surface of an electrode to participate in the water splitting reaction. Therefore, a technique to improve photocurrent density involves generating a higher yield of electron/hole pairs, an effect that can be achieved using metallic nanomaterials. Plasmonic metal nanostructures can be used to increase charge separation and migration. In wide bandgap semiconductor, this mechanism is dominated by hot electron generation, or charge carriers of high energy, which can improve electron/hole separation and improve charge collection. For smaller bandgap semiconductors such as hematite, plasmon resonances may have the additional effect of improving photocurrent density by enhancing visible light absorption efficiency in the surrounding semiconductor material, if nanomaterial architectures are properly designed.

Noble metals have been extensively demonstrated as a plasmonic materials to improve hematite's PEC properties. [21-25] In the case of gold, a commonly studied plasmonic metal due to its chemical and thermal stability, the absorption enhancement is minimal due to gold's narrow plasmon resonance, located around 600 nm, which lies outside of hematite band absorption edge, 560-580 nm. Neither gold nor silver are not-cost effective solutions for large-scale applications, leading researchers look for alternative plasmonic materials. It has been theoretically demonstrated that alternative plasmonic metals aluminum and

copper improve the absorbance in photocatalysts such as hematite by using them as the metal layer in semiconductor-metal-hematite CMS nanowire architectures.[21, 25] Though low in cost compared to noble metals, these materials' are limited by their chemical and thermal instability, resulting in structures that are difficult to fabricate. Additionally, thermal instability results in surface oxide formation, which inhibit movement of electrons to the charge collector or optically shift the wavelength of or diminish the intensity of their plasmon resonances.[106-107]

Transition metal nitrides are emerging as alternative materials to traditional plasmonic metals. Specifically TiN and ZrN, which can have real and imaginary permittivity and LSPR that are tunable in the visible region.[108-109] Though these are wide-band gap materials, low resistance and plasmonic properties have been reported for non-stoichiometric TiN_x (where is $x < 1$ or $x > 1$) and ZrN_x (where $x < 1$).[108, 110] Unlike aluminum and copper, transition metal nitrides are thermally stable and compatible with a wide range of fabrication techniques. And unlike noble metals, the plasmon wavelength and optical constants of transition metal nitrides are tunable. This can be achieved by altering deposition conditions such as temperature, nitrogen-source ratios and substrate[109, 111-112], allowing the optical properties to be tuned to meet the individual needs of the device. Finally, plasmonic properties of TiN have been demonstrated film thicknesses below 10 nm.[113-114] These characteristics make these emerging plasmonic materials optimal for PEC applications.

TiO_2 photoanodes decorated with TiN NPs perform the solar water oxidation reaction more efficiently than TiO_2 decorated with AuNPs, both of which display higher photocurrent density than bare TiO_2. The enhancement is attributed to TiN's more

broadband absorption efficiency, resulting in improved incident photon conversion efficiency due to hot-charge carriers over a larger portion of the visible region. Additionally, the TiN forms a Plasmonic Ohmic Interface with TiO_2, which promotes efficient charge transfer compared to the Plasmonic Schottky Interface of gold/TiO_2. [26]

Properly designing the nanostructured architecture is essential for fabricating efficient hematite photoanodes. One-dimensional nanostructures and nanowires have unique optical resonances and electrical properties compared to bulk and zero-dimensional materials. Plasmonic NWs coated in a hematite shell and semiconductor-metal-hematite CMS NWs for PEC applications have previously been experimentally demonstrated by *Ramadurgam et al in 2014*, which demonstrated plasmonic metals using this 1D architecture increase the visible light absorbance in hematite.[21, 25] Plasmonic metals Al, Ag, Au and Cu are studied, and all are found to theoretically increase the absorbance in the surrounding semiconductor. To expand on that work, metal-hematite and semiconductor-metal-hematite nanostructures are proposed, studying TiN and ZrN as the plasmonic metal. The ideal photocurrent densities of the CS and CMS NWs are theoretically studied. Experiments are carried out in the pursuit of low-temperature synthesis of ultra-thin metal nitride materials with visible-light plasmon wavelengths.

4.2   Simulations for Core-Shell and Core-Multishell Nanowire Architectures

In this section, theoretical studies to calculate ideal photocurrent density and CS and CMS NWs were conducted using the nanoHUB.com tool *Optical Properties of Single Coaxial Nanowires*[115], which evaluates the effectiveness of the CS and CMS NW architectures using Mie formalism to obtain rigorous solutions to Maxwell's equations for a single NW under TE, TM and unpolarized light for a single NW, as detailed previously.[21]

Real and imaginary parts of the dielectric constant (ε_1 and ε_2, respectively) were taken from Nanohub,[115] and specifically the values for TiN and ZrN can be viewed graphically in Figure A.6. The resulting data is presented as ideal photocurrent density as a function of hematite shell thickness (Figure 4.1) for core, CS and CMS NW structures.
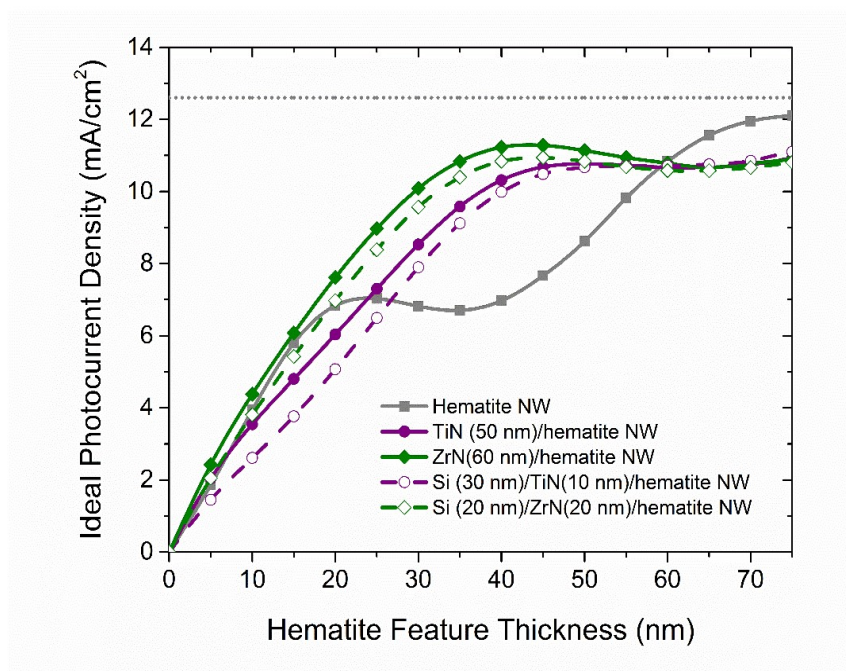
Figure 4.1 Ideal photocurrent density for hematite NW (gray) core/shell (purple, green solid lines) and core multi-shell (purple, green dashed lines) nanowire structures as a function of hematite radius / shell thickness. Dotted gray line at 12.6 mA/cm^2 represents the theoretical bulk maximum photocurrent density for hematite.

The NWs containing plasmonic metal nitrides demonstrate improved photocurrent density compared to a single hematite NW. A TiN/hematite CS NW with core diameter of 50 nm (solid purple line) shows improved photocurrent for hematite shell thicknesses of 30 to 55 nm compared to a single hematite wire (gray squares). Though the peak photocurrent density is 10.8 mA/cm^2 for a hematite shell thickness of 50 nm, to meet the condition of ultra-thin hematite shells to promote charge transport, hematite shells less than or equal to 40 nm are considered. At a hematite shell thickness of 40 nm, the TiN results

in a photocurrent density 1.62 times greater than that of a single hematite wire with a comparable hematite radius. Similarly, photocurrent density is improved in a ZrN/hematite CS NW (solid green line) with a core diameter of 60 nm for hematite shell thicknesses of 20 to 55 nm, with a maximum photocurrent density of 11.3 mA/cm^2. At a hematite shell radius of 40 nm, the ideal photocurrent density is 1.8 times greater than that predicted for an 80 nm diameter hematite NW.

Despite the promise of TiN/hematite and ZrN/hemaite CS NWs, there are fabrication difficulties in synthesizing metal nitride nanowires. As an alternative, CMS NWs using a silicon core, metal nitride shell, and hematite outer shell are proposed. Silicon is considered as the core material due to ease of fabrication via established methods such as CVD,[65, 116] compatibility with metal nitride materials,[109] and results from previous reports which indicate that Si NWs act as a duel-absorber to reduce the required overpotential of the oxygen evolution reaction.[21, 24, 42, 109, 117] Here we use Si NW diameters of 20 nm (in the case of Si/ZrN/hematite) and 30 nm (in the case of Si/TiN/hematite).

As seen in Figure 4.1, a Si/TiN/hematite CMS NW (dashed purple line) shows enhanced photocurrent density compared to a single hematite NW, with an ideal photocurrent density of 9.78 mA/cm^2 for sub-50 nm hematite feature thicknesses. Similarly, a Si/ZrN/hematite CMS NW (green dashed line) is predicted to generate a maximum of 10.8 mA/cm^2 photocurrent. In both cases, it is predicted that the CMS NW generates less photocurrent density than its CS counterpart. Regardless, for hematite feature thickness of 40 nm, both CMS NW structures perform more efficiently than the 6.97 mA/cm^2 predicted for a hematite NW.

Both CS and CMS NWs with plasmonic metal nitrides reach photocurrent densities over 8.2 mA/cm^2, corresponding to a solar-to-hydrogen higher than 10%, making them viable for commercialization. Additionally, the photocurrent densities predicted using metal nitride nanomaterials are comparable to Si/Al/hematite (11.8 mA/cm^2) and greater than Si/Au/hematite (< 9.0 mA/cm^2) CMS NW calculations previously reported.[21]

The calculations clearly show that ZrN may be the more promising plasmonic material for improving the solar to hydrogen efficiency of hematite. However, plasmonic TiN is a more commonly synthesized, understood material with already-confirmed fabrication methods and tunable plasmon resonances.[109, 112, 118-119] TiN is also unique in that is exhibits plasmonic properties with either nitrogen-rich or nitrogen-vacant, allowing for ease of fabrication compared to other metal nitride plasmonic material. Additionally, hot electron generation has been demonstrated by TiN nanoparticles to improve solar water oxidation efficiency,[26] an effect these simulations do not consider. Therefore, both TiN and ZrN should be considered for future experimentation.

4.3   Synthesis of Thin Plasmonic Titanium Nitride Thin Films

4.3.1   Plasma-Enhanced ALD for TiN

To fabricate TiN/hematite and Si/TiN/hematite CMS NWs, there is a need for a method to synthesize thin TiN features with plasmonic optical properties and plasmon wavelengths. Additionally, this method must allow for conformal synthesis of TiN on 1D silicon nanostructures.

Though TiN is a wide bandgap material (E_g = 3.35-3.45 eV), metallic and plasmonic titanium nitride thin films have been synthesized using a variety of techniques which result in nonstoichiometric TiN$_x$. One technique previously demonstrated is ALD,

where the TiN properties are dependent on the non-stoichiometry and TiN film purity.[120] ALD can achieve conformal deposition of TiN on a 1-D nanostructure and thicknesses on the order of 10 nm.[111] Finally, deposition conditions and post-deposition high temperature annealing of TiN films can change the optical properties and blue-shift the resonance to below 600 nm, giving the TiN plasmon resonance better alignment with hematite's absorption band edge.[111-112] For these reasons, ALD is the preferred technique for the synthesis of the intermediate TiN shell for CMS NW photoanodes.

At present, high temperatures, such as those over 400^0 C, are often used for thermal ALD of plasmonic TiN,[111] which may not be ideal for a variety of applications. Instead, here is propose a lower temperature ($< 300^0$ C) PE-ALD using tetrakisdimethylamido titanium (TDMATi) as the titanium precursor and NH_3 plasma as the nitrogen precursor to synthesize metallic titanium nitride thin films with plasmon wavelengths in the visible region, which retain their plasmonic properties at thickness of 10 nm.

The ALD reaction is performed under similar conditions as that of previously reported for TiN.[121] The substrates, Si <100> and MgO, is placed in the reaction chamber under vacuum and heated to 250 C. The TDMATi precursor is heated to 60^0 C and exposed to the substrate for a 2 s exposure time followed by a 10 s purge. The 300 W plasma consisting of 200 sccm Ar and 10 sccm NH_3 is pulsed for 20 s, followed by a 10 s purge. This completes one ALD cycle, which is repeated until desired thickness is achieved.

4.3.2   Structural Characterization

To determine the growth rate and physical characteristics of the as deposited TIN thin films, X-Ray Reflectivity (XRR) is employed (Figure A.7). The as prepared thin films appears as the characteristic gold/pink color of metallic TiN on silicon.[112] As the film

thickness increases the color of the TiN appears to change from yellow to orange/gold to pink (Figure 4.2).

Figure 4.2 Digital images of ALD titanium nitride on silicon for thickness of (a) 89 nm (b) 55 and (c) 28 nm .

To quantitatively ensure successful synthesis of TiN using these ALD conditions, Raman Spectroscopy is employed (Figure 4.3). Four peaks consistent with TiN are observed: 220 (TA), 310 (LA), 570 (TO) cm^{-1} are consistent with first order Raman Scattering and a small shoulder at 830 cm^{-1} (LA+TO), consistent with second order Raman scattering in TiN.[122] The acoustic scattering is associated with vibrations from heavy titanium ions while the optical scattering is contributed to by the lighter nitrogen ions.[122-123] On both Si <100> and MgO, the TO peak is lower in intensity than the acoustic peaks, indicating that there are some nitrogen vacancies in the film.[122, 124] Therefore, nitrogen-vacant TiN$_{1-x}$ thin film is the product of TDMATi and NH$_3$ plasma.

To observe the optical properties and plasmon wavelength of the thin film TiN, multi-angle, multi-wavelength Spectroscopic Ellipsometry is employed. The spectroscopic ellipsometry data is measured at incident angles of 65°, 70° and 75° from wavelengths of 400-1000 nm. The raw data is modeled using a Drude-Lorentz Function with one Lorentz operator to obtain the real (ε_1) and imaginary (ε_2) values of the permittivity. The plasmon wavelength is determined by $\lambda(\varepsilon_1=0)$.
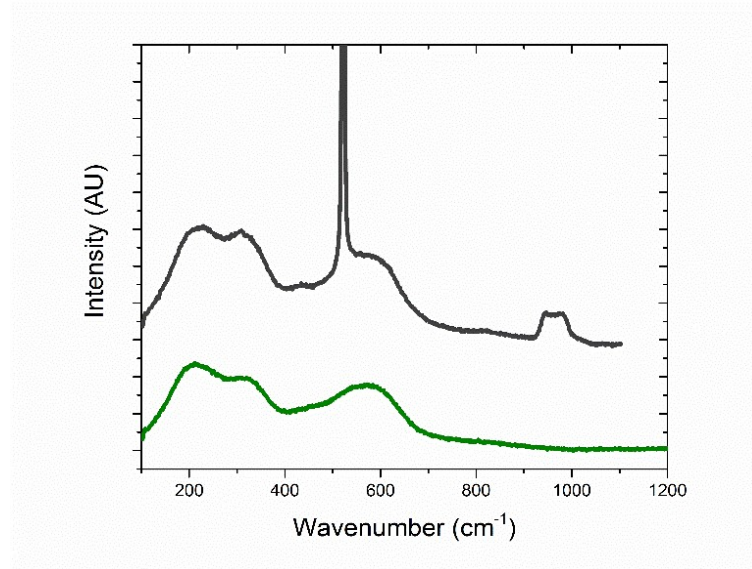
Figure 4.3 Raman spectrum of as-deposited 50 nm TiN thin film on MgO (green) and Si <100> (gray). The sharp peak at 521 cm^{-1} and broad peak at 960 cm^{-1} are attributed to the Si <100> substrate.

4.3.3   Optical Characterization

To determine the plasmonic and optical properties of the TiN thin films, dielectric functions ε_1 and ε_2 are measured for TiN on Si <100> and MgO substrates for TiN thin films of approximately 50 nm and 10 nm (Figure 4.4). First, the MgO substrate is analyzed (Figure 4.4a) which is of interest due to its lattice parameter (a = 0.421 nm) being nearly identical to that of TiN (a = 0.424 nm), promoting epitaxial growth and TiN with good crystallinity. On MgO, a steep negative value of ε_1 is observed through the visible and near infrared region of the spectrum, indicating that the film is optically metallic. The real value of the dielectric function is red-shifted and smaller in magnitude (i.e. less metallic) in the 10 nm thin film compared to the 55 nm film. This is likely due to the increased presence of oxygen in the 10 nm film, as established previously.[114, 118]
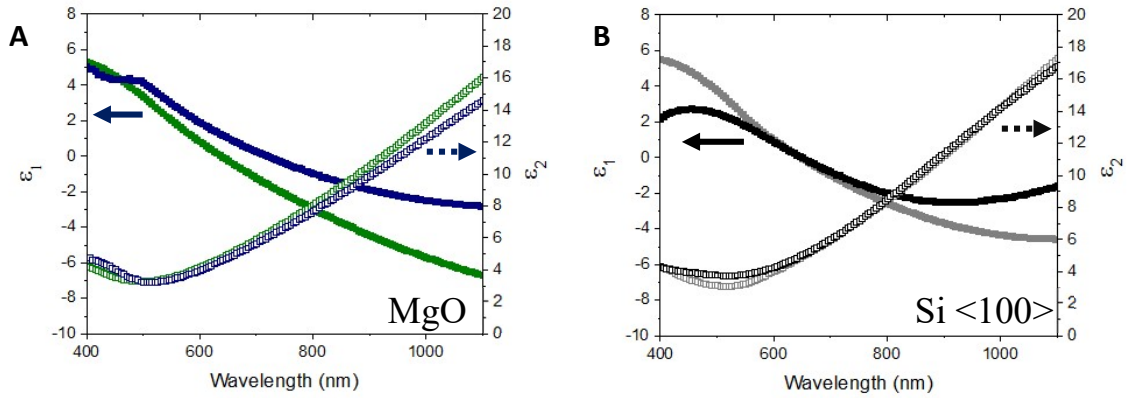
Figure 4.4 Real (solid symbols) and imaginary (open symbols) of the dielectric function for ALD grown TiN thin films on (a) MgO and (b) Si <100> for 50 nm (green, gray) and 10 nm (blue, black)

On Si <100>, the ε_1 of 50 nm TiN has a negative slope over the visible and near-IR region. However, this slope is of lower magnitude in the NIR region, indicating it has less metallic quality. In the case of the 10 nm film, ε_1 is negative. It is noteworthy that ε_1 is smaller in magnitude, especially in the near-IR, and therefore shows more dielectric quality than its 50 nm counterpart. Additionally, TiN grown on silicon has a less intense, broader plasmon resonance compared to TiN deposited on MgO in both the 55 and 10 nm cases. TiN grown on Si also has a higher value of ε_2, and therefore greater optical losses compared to films grown on MgO. The substrate dependence of both ε_1 and ε_2 are likely due to the lattice mismatch between Si (a = 0.543 nm) and TiN, resulting in poorer crystal quality in TiN on Si compared to TiN on MgO.

In addition to the values of ε_1 and ε_2, the plasmon wavelength is also dependent on the substrate and TiN thickness (Table 4.1). For MgO, the red-shift in the plasmon wavelength that occurs when the film thickness is reduced is likely caused by a higher concentration and greater influence of oxygen in the 10 nm film compared to the 55 nm film.[113-114] Interestingly, despite the change in magnitude of ε_1 at higher wavelengths

observed for the Si substrate, the plasmon wavelength is similar for thicknesses of 55 and 10 nm, red-shifting by 5 nm. That the thin film retains its visible-region plasmon wavelength even at 10 nm indicates that it should be viable for PEC enhancement applications when deposited on a silicon substrate.

Table 4.1 Plasmon wavelengths for TiN thin films deposited on MgO and Silicon substrates

Substrate	TiN thickness (nm)	λ_{ps} (nm)
MgO	54.8 nm	639
MgO	10.5 nm	719
Si	53.2 nm	646
Si	10.2 nm	651

4.4   Conclusion

In conclusion, emerging plasmonic materials TiN and ZrN have many advantages over both traditional and other alternative plasmonic metals. It is theoretically demonstrated that emerging plasmonic materials TiN and ZrN are promising candidates to improve the ideal photocurrent density hematite photoanodes using core-shell and core-multishell nanowire deigns. For the CS NW case, hematite photocurrent densities at 40 nm shell thicknesses are improved by 1.62 times using TiN and 1.8 times using ZrN plasmonic cores. Alternatively, using silicon-core, mental nitride plasmonic shell and hematite outer shell also results in comparable, improved ideal photocurrent density for 40 nm hematite features. Thus these plasmonic materials may allow hematite to remain electrically thin enough to effectively transport charge carriers while absorbing light similar to thick hematite features.

Experimental results demonstrate that nitrogen vacant TiN thin films can be synthesized on silicon using a PE-ALD method utilizing precursors TDMATi and NH_3 plasma. These thin films retain their visible plasmonic properties down to film thicknesses of 10.5 nm, which has a slightly red-shifted visible light plasmon wavelength of 651 nm compared to thicker films. Further optimization can be performed, such as modifying the NH_3 flow rate of the plasma precursor or changing the plasma duration, to fabricate TiN thin films with stronger, sharper plasmon resonances or fewer optical losses. The films synthesized herein are predicted to be suitable for fabrication into TiN cores for the CS NW architecture, or depositing on Si NWs for the CMS NWs, to improve the photocurrent density of very thin hematite. Future work is needed to experimentally demonstrate the effect of TiN on hematite's photocurrent density.

CHAPTER 5.   SUMMARY & OUTLOOK

5.1   Summary

In this dissertation, I make the case for using hematite as a test material to study enhancement techniques for metal oxide solar water splitting, due to its earth abundance, low cost, and small bandgap. Hematite's limited electronic properties keep it from reaching its theoretical potential. The synthesis of nanostructured hematite is versatile and various techniques can be utilized depending on the morphology and design needs of the photoanode (CHAPTER 2). The enhancement of hematite nanomaterials for solar water splitting is accomplished using techniques to increase the lifetime and number of electron/hole pairs. This is achieved experimentally through surface modification with single layer graphene to decrease the rate of recombination (CHAPTER 3) and theoretically expanding its visible light absorption efficiencies (CHAPTER 4).

It is demonstrated that single layer graphene synthesized via CVD can be successfully transferred to nanostructured, doped hematite to improve its photocurrent density. We prove this is a surface-only modification technique that does not affect the hematite bulk and is therefore suitable for pre-optimized photoelectrodes. Electrochemical experiments were carried out to conclusively prove the mechanism by which a single layer graphene overlayer enhances the water splitting reaction. SLG improves charge transfer efficiency by dramatically retarding the recombination rate, from 71 to 13 s^{-1} at 1.2 V_{RHE}. Interestingly, the rate of charge transfer decreases compared to bare hematite, therefore showing that the SLG overlayer acts as a passivation layer (similar to previous reports of TiO_2 and Al_2O_3)[15-17] and not a co-catalyst. Finally, it is shown that this may be a general

technique for improving the photocurrent density of nanostructured, metal oxide photoanodes.

Second, this dissertation expanded on work previously conducted by *Ramadurgam et al*[21, 25] to explore plasmon enhancement of hematite photoanodes using CS and CMS NW architectures by utilizing emerging plasmonic materials. Theoretically it is demonstrated for the first time that plasmonic TiN and ZrN can be used to improve hematite's photocurrent density. For sub-50 nm hematite features, STH efficiencies greater than 10% are achieved, making this a viable method for commercialization. In pursuit of fabricating CS and CMS NWs, a low temperature ALD method to synthesize ultra-thin films of plasmonic TiN on silicon was developed. The 55 nm TiN has a visible light plasmon resonance of 646 nm, and retains its plasmonic properties below 10 nm thickness ($\varepsilon_1 < 0$ with $\lambda_{ps} = 651$ nm). Thereby making the fabrication of TiN for both CS and CMS NW possible.

5.2   Outlook

This dissertation contributes to the large body of work on semiconductor nanomaterials for the solar-powered generation of hydrogen. Hematite, by many accounts, is of great promise to perform the oxygen evolution half reaction for solar water splitting. Recent work in 2017 by *Jeun et al* has demonstrated that a combination of techniques – nanostructuring, non-metal doping, and surface modification by both passivation and co-catalyst materials - can result in a stable hematite photoanode with 6 mA/cm^2 at 1.23 V_{RHE}, is nearly half its calculated ideal value.[125] Furthermore, another future outlook for hematite based nanomaterials for solar hydrogen generation is hybrid PV-PEC tandem cells.[126]

Despite recent accomplishments, whether hematite is being employed for PEC alone or part of a PV-PEC tandem set-up, there is much to be understood to achieve a hematite photoanode with 15% solar to hydrogen efficiency. Continuing to pursue and understand nanomaterials to enhance hematite's solar to hydrogen efficiency also has the potential to assist in enhancing other semiconductor materials for solar water splitting. Here, further research objectives are discussed to further this understanding and result in greater enhancement.

5.2.1   Carbon Overlayers on Metal Oxide Photoelectrodes

Further research directions can expand on the current study of SLG as an overlayer on nanostructured hematite. Optimizing the layer number and quality of the graphene on hematite, with the goal suppressing the recombination rate (k_{rec}) without inhibiting the rate of charge transfer (k_{tran}), is an important future step to obtain the best performance. Additionally, while results from IMPS and EIS were used herein to conclusively demonstrate that SLG acts as a passivation layer, other researchers have speculated that overlayers made of rGO act as a co-catalyst due to decreased resistance of charge transfer in the presence of rGO due largely to EIS results demonstrating reduced charge transfer resistance. As results here and elsewhere indicate, reduced R_{CT} does not conclusively correlate with co-catalyst functionality, future work may be conducted to better ascertain the role of rGO and amorphous carbon overlayers. By employing the technique IMPS on these modified photoanodes, the mechanism by which rGO flakes assembled as an overlayer and amorphous carbon coatings improve hematite's photocurrent and overall efficiency can be confirmed. This insight would allow for researchers to configure the

optimal carbon coatings to obtain the best solar-to-hydrogen efficiency of hematite photoanodes.

5.2.2   Semiconductor-Metal Nitride-Hematite CMS NWs

Fabricating the proposed core-shell and core-multishell nanowires in 4.2 is the first of many outlooks for utilizing Si-TiN-hematite CMS NWs as highly efficient photoanodes. The proposed fabrication method is as follows: Silicon nanowire cores with precise diameters can be fabricated via chemical vapor deposition, and 10 nm TiN shells can be uniformly deposited on these 1D nanomaterials using ALD (described in 4.3). Ferrocene vapors (described in 2.4) can be evaporated and utilized to assemble conformal hematite shells around the 1D nanostructures. Alternatively, ALD could be used to synthesize the hematite outer shell.

The optical properties of the fabricated CMS NWs can be experimentally determined using dark field spectroscopy on single NWs and UV-vis-NIR spectroscopy to measure total hemispherical reflectance on NW arrays. Electrochemical experiments to measure photocurrent density and incident photon conversion efficiency (IPCE) can be carried out to experimentally determine the photocurrent density and quantum efficiency, to ensure TiN does improve solar to hydrogen efficiency.

Future work should also involve synthesis of plasmonic ZrN thin films and nanowires, as ZrN/hematite and Si/ZrN/hematite theoretically demonstrate higher photocurrent densities than their TiN NW counterparts. Previous work has synthesized plasmonic ZrN via sputtering,[108] but this technique may not be optimal to deposit conformal, 20 nm shells on 1-D silicon nanostructures. Preliminary studies in our lab are ongoing to develop an ALD synthesis using tetrakisdimethylamido zirconium (TDMAZr)

and NH_3 plasma for the deposition of ZrN thin films with visible light plasmon resonances. These films have variety of potential applications including visible light plasmon enhancement of photoelectrocatalytic semiconductors.

APPENDIX
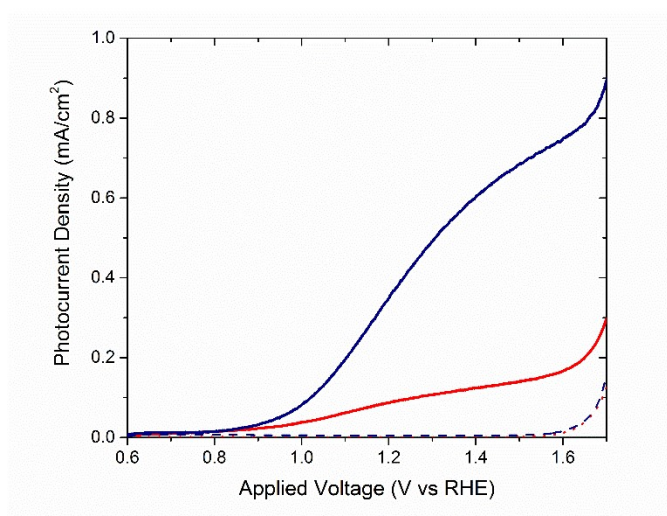
Figure A.1 Representative linear sweep voltammetry results comparing photocurrent densities of undoped (red) and Sn-doped (blue) hematite prepared by identical hydrothermal synthesis conditions, under one sun illumination (solid lines) and in the dark (dashed lines).
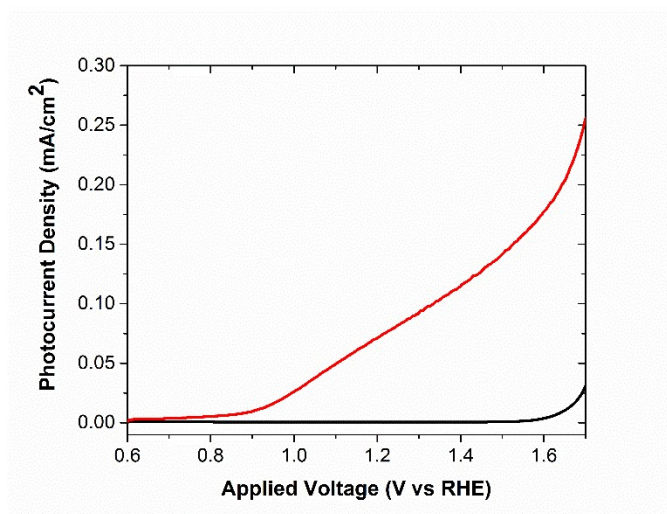
Figure A.2 Representative linear sweep voltammetry results for hematite synthesized via ferrocene pyrolysis using 50 mg ferrocene precursor
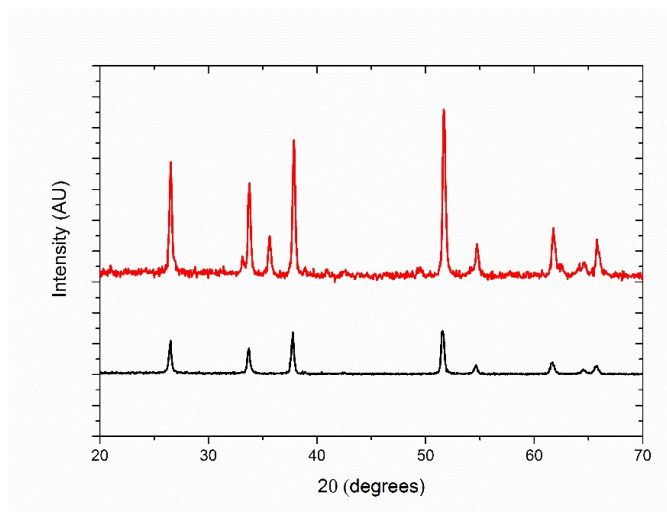
Figure A.3 XRD spectrum of hematite (red) synthesized via hydrothermal deposition on FTO (black)
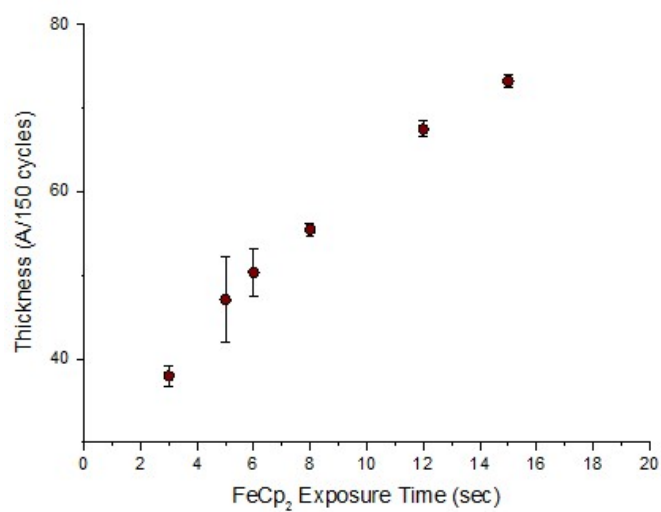
Figure A.4 Iron oxide thin film growth per 150 ALD cycles as a function of ferrocene (FeCp2) precursor exposure time. Growth parameters include 40 s exposure, 300 W oxygen plasma at a chamber temperature of 200° C
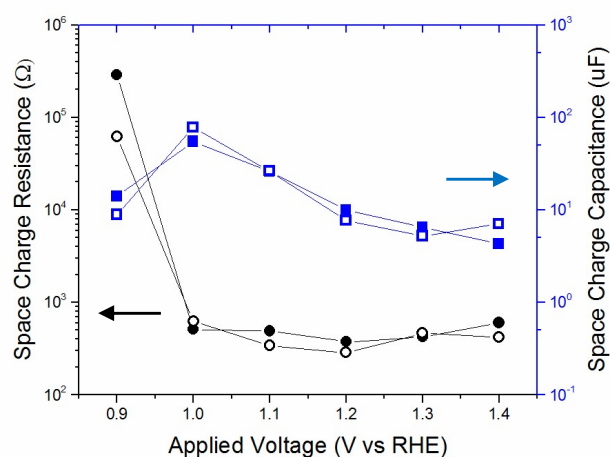
Figure A.5 EIS analysis displaying R_{SC} (black) and C_{SC} (blue) with (open markers) and without (closed markers) single layer graphene overlayer. There is no significant change in either parameter with the addition of the SLG overlayer, indicating that the overlayer does not affect the resistance or capacitance of the bulk of the hematite.
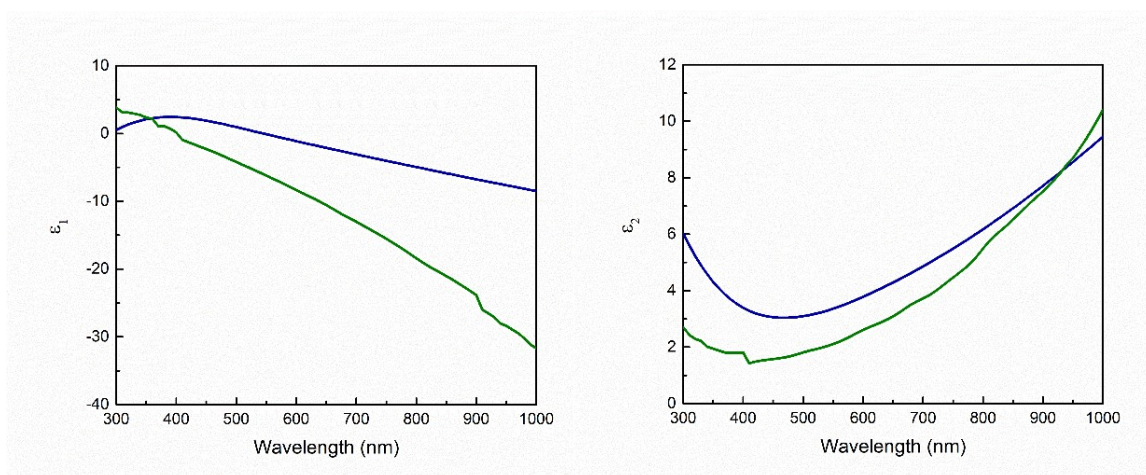
Figure A.6 Real (left) and imaginary (right) values of the dielectric constant for TiN (blue) and ZrN (green) as used to calculate theoretical photocurrent densities in 4.2. Values extracted from Nanohub tool "Optical Properties of Single Coaxial Nanowires".[115]
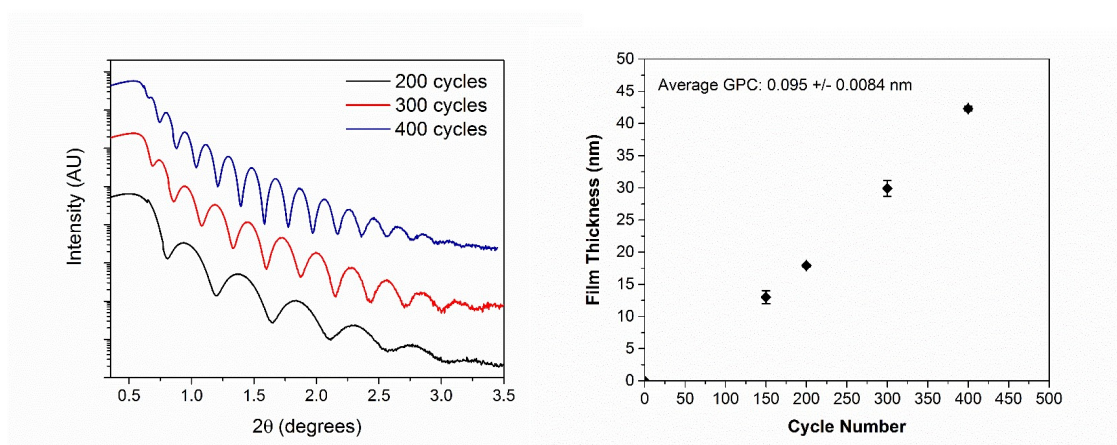
Figure A.7 Representative XRR spectra for TiN on silicon for 200, 300 and 400 cycles (left) and TiN film thickness as a function of cycle number (right)

REFERENCES

1. *Hydrogen Hydrogen Posture Plan An Integrated Research, Development and Demonstration Plan*; United States Department of Energy, United States Department of Transportation 2006.

2. Joseck, F.; Nguyen, T.; Klahr, B.; Talapatra, A. *Current U.S. Hydrogen Production* DOE Hydrogen and Fuel Cells Program Record: United States 2016; pp 1-2.

3. *Distributed Hydrogen Production from Natrual Gas - Independent Review*; https://www.hydrogen.energy.gov/pdfs/40382.pdf; National Renewable Energy Laboratory October 2006.

4. Hydrogen Production Pathways. https://www.energy.gov/eere/fuelcells/hydrogen-production-pathways.

5. Fujishima, A.; Honda, K., ELECTROCHEMICAL PHOTOLYSIS OF WATER AT A SEMICONDUCTOR ELECTRODE. *Nature* **1972,** *238* (5358).

6. Ni, M.; Leung, M. K. H.; Leung, D. Y. C.; Sumathy, K., A review and recent developments in photocatalytic water-splitting using TiO2 for hydrogen production. *Renewable and Sustainable Energy Reviews* **2007,** *11* (3), 401-425.

7. Shon, H.; Puhuntsho, S.; Okour, Y.; Cho, D.; Kim, K.; Li, H.; Na, S.; Kim, J.; Kim, J., Visible Light Responsive Titanium Dioxide (TiO2). *Journal of the Korean Industrial and Engineering Chemistry* **2008,** *19*, 1-16.

8. Zhang, H.; Chen, G.; Bahnemann, D. W., Photoelectrocatalytic materials for environmental applications. *Journal of Materials Chemistry* **2009,** *19* (29), 5089-5121.

9. Hardee, K. L.; Bard, A. J., Semiconductor Electrodes: V . The Application of Chemically Vapor Deposited Iron Oxide Films to Photosensitized Electrolysis. *Journal of The Electrochemical Society* **1976,** *123* (7), 1024-1026.

10. Kennedy, J. H.; Frese Jr., K. W., Photooxidation of Water at a-Fe2O3 Electrodes. *J. Electrochem. Soc.* **1978,** *125*, 709-714.

11. Zhong, D. K.; Gamelin, D. R., Photoelectrochemical water oxidation by cobalt catalyst ("Co-Pi")/a-Fe2O3 Composite photoanodes: Oxygen Evolution and Resolution of Kinetic Bottleneck. *JACS* **2011,** *132*, 4202-4207.

12. Zhong, D. K.; Cornuz, M.; Sivula, K.; Gratzel, M.; Gamelin, D. R., Photo-assisted electrodoposition of cobalt-phosphate (Co-Pi) catalyst on hematite photoanodes for solar water oxidation. *Energy Environ. Sci* **2011,** *4*, 1759-1764.

13. Tilley, D. S.; Cornuz, M.; Sivula, K.; Gratzel, M., Light-Induced Water Splitting with Hematite: Improved Nanostructure and Iridium Oxide Catalyst. *Angewandte Chemie, International Edition* **2010,** *49* (36), 1433-7851.

14. Klahr, B.; Gimenez, S.; Fabregat-Santiago, F.; Hamann, T.; Bisquert, J., Water Oxidation at Hematite Photoelectrodes: The Role of Surface States. *Journal of the American Chemical Society* **2012,** *134* (9), 4294-4302.

15. Le Formal, F.; Tétreault, N.; Cornuz, M.; Moehl, T.; Gratzel, M.; Sivula, K., Passivating surface states on water splitting photoanodes with alumina overlayers. *Chem. Sci.* **2011,** *2*, 737-743.

16. Ahmed, M. G.; Kretschmer, I. E.; Kandiel, T. A.; Ahmed, A. Y.; Rashwan, F. A.; Bahnemann, D. W., A facile surface passivation of hematite photoanodes with TiO2 overlayers for efficient solar water splitting *ACS Appl. Mater. Interfaces* **2015,** *7* (43), 24053-24062

17. Yang, X.; Liu, R.; Du, C.; Dai, P.; Zheng, Z.; Wang, D., Improving Hematite-based photoelectrochemical water splitting with ultrathin TiO2 by Atomic Layer Deposition. *ACS Appl. Mater. Interfaces* **2014,** *6* (15), 12005-12011.

18. Yang, Y.; Forster, M.; Ling, Y.; Wang, G.; Zhai, T.; Tong, Y.; Cowan, A.; Li, Y., Acid treatment enables suppression of electron-hole recombination in hematite for photoelectrochemical water splitting. *Angew. Chem.* **2016,** *128*, 3464-3468.

19. Dias, P.; Andrade, L.; Mendes, A., Hematite-based photoelectrode for solar water splitting with very high photovoltage. *Nano Energy* **2017,** *38*, 218-231.

20. Cushing, S. K.; Li, J.; Meng, F.; Senty, T. R.; Suri, S.; Zhi, M.; Li, M.; Bristow, A. D.; Wu, N., Photocatalytic Activity Enhanced by Plasmonic Resonant Energy Transfer from Metal to Semiconductor. *Journal of the American Chemical Society* **2012,** *134* (36), 15033-15041.

21. Ramadurgam, S.; Lin, T.-G.; Yang, C., Aluminum Plasmonics for Enhanced Visible Light Absorption and High Efficiency Water Splitting in Core-Multishell Nanowire Photoelectrodes with Ultrathin Hematite Shells. *Nano Letters* **2014,** *14* (8), 4517-4522.

22. Archana, P. S.; Pachauri, N.; Shan, Z.; Pan, S.; Gupta, A., Plasmonic Enhancement of Photoactivity by Gold Nanoparticles Embedded in Hematite Films. *The Journal of Physical Chemistry C* **2015,** *119* (27), 15506-15516.

23. Gao, H.; Liu, C.; Jeong, H. E.; Yang, P., Plasmon-Enhanced Photocatalytic Activity of Iron Oxide on Gold Nanopillars. *ACS Nano* **2012,** *6* (1), 234-240.

24. Wang, X.; Peng, K.-Q.; Hu, Y.; Zhang, F.-Q.; Hu, B.; Li, L.; Wang, M.; Meng, X.-M.; Lee, S.-T., Silicon/Hematite Core/Shell Nanowire Array Decorated with Gold Nanoparticles for Unbiased Solar Water Oxidation. *Nano Letters* **2014,** *14* (1), 18-23.

25. Ramadurgam, S.; Yang, C. In *Aluminum and copper plasmonics for enhancing internal quantum efficiency of core-shell and core-multishell nanowire photoelectrodes*, SPIE NanoScience + Engineering, SPIE: 2014; p 7.

26. Naldoni, A.; Guler, U.; Wang, Z.; Marelli, M.; Malara, F.; Meng, X.; Besteiro, L. V.; Govorov, A. O.; Kildishev, A. V.; Boltasseva, A.; Shalaev, V. M., Broadband Hot-Electron Collection for Solar Water Splitting with Plasmonic Titanium Nitride. *Advanced Optical Materials* **2017,** *5* (15), 1601031.

27. Shevjakov, A.; Kuznetsova, G.; Aleskovskii, V. In *Chemistry of high temperature materials*, Proceedings of the second USSR conference on high-temperature chemistry of oxides, Leningrad, USSR, 1965; pp 26-29.

28. Suntola, T.; Antson, J. Method for Producing Compound Thin Films. 1977.

29. Johnson, R. W.; Hultqvist, A.; Bent, S. F., A brief review of atomic layer deposition: from fundamentals to applications. *Materials Today* **2014,** *17* (5), 236-246.

30. Elam, J. W., Coatings on High Aspect Ratio Structures. In *Atomic Layer Deposition of Nanostructured Materials*.

31. Puurunen, R. L., Surface chemistry of atomic layer deposition: A case study for the trimethylaluminum/water process. *Journal of Applied Physics* **2005,** *97* (12), 121301.

32. De Keijser, M.; Van Opdorp, C., Atomic layer epitaxy of gallium arsenide with use of atomic hydrogen. *Appl. Phys. Lett.* **1991,** *58*, 1187-1189.

33. Profijt, H. B.; Potts, S. E.; van de Sanden, M. C. M.; Kessels, W. M. M., Plasma-Assisted Atomic Layer Deposition: Basics, Opportunities, and Challenges. *Journal of Vacuum Science & Technology A* **2011,** *29* (5), 050801.

34. Hyungjun, K.; Il-Kwon, O., Review of plasma-enhanced atomic layer deposition: Technical enabler of nanoscale device fabrication. *Japanese Journal of Applied Physics* **2014,** *53* (3S2), 03DA01.

35. Zandi, O.; Schon, A. R.; Hajibabaei, H.; Hamann, T. W., Enhanced Charge Separation and Collection in High-Performance Electrodeposited Hematite Films. *Chemistry of Materials* **2016,** *28* (3), 765-771.

36. Spray, R. L.; Choi, K.-S., Photoactivity of Transparent Nanocrystalline Fe2O3 Electrodes Prepared via Anodic Electrodeposition. *Chemistry of Materials* **2009,** *21* (15), 3701-3709.

37. Wang, G.; Ling, Y.; Wheeler, D. A.; George, K. E. N.; Horsley, K.; Heske, C.; Zhang, J. Z.; Li, Y., Facile Synthesis of Highly Photoactive α-Fe2O3 based Films for Water Oxidation. *Nano Lett.* **2011,** *11*, 3503-3509.

38. Kim, J. Y.; Magesh, G.; Youn, D. H.; Jang, J.-W.; Kubota, J.; Domen, K.; Lee, J. S., Single-crystalline, wormlike hematite photoanodes for efficient solar water splitting. *Scientific Reports* **2013,** *3*.

39. Klahr, B. M.; Martinson, A. B. F.; Hamann, T. W., Photoelectrochemical Investigation of Ultrathin Film Iron Oxide Solar Cells Prepared by Atomic Layer Deposition. *Langmuir* **2011,** *27* (1), 461-468.

40. Zandi, O.; Klahr, B. M.; Hamann, T. W., Highly photoactive Ti-doped alpha-Fe2O3 thin film electrodes: resurrection of the dead layer. *Energy & Environmental Science* **2013,** *6* (2), 634-642.

41. Kronawitter, C. X.; Zegkinoglou, I.; Shen, S. H.; Liao, P.; Cho, I. S.; Zandi, O.; Liu, Y. S.; Lashgari, K.; Westin, G.; Guo, J. H.; Himpsel, F. J.; Carter, E. A.; Zheng, X. L.; Hamann, T. W.; Koel, B. E.; Mao, S. S.; Vayssieres, L., Titanium incorporation into hematite photoelectrodes: theoretical considerations and experimental observations. *Energy & Environmental Science* **2014,** *7* (10), 3100-3121.

42. Mayer, M. T.; Du, C.; Wang, D., Hematite/Si Nanowire Dual-Absorber System for Photoelectrochemical Water Splitting at Low Applied Potentials. *Journal of the American Chemical Society* **2012,** *134* (30), 12406-12409.

43. Kneipp, K.; Kneipp, H.; Itzkan, I.; Dasari, R. R.; Feld, M. S., Ultrasensitive Chemical Analysis by Raman Spectroscopy. *Chemical Reviews* **1999,** *99* (10), 2957-2976.

44. Loudon, R., The Raman effect in crystals. *Advances in Physics* **1964,** *13* (52), 423-482.

45. Thibeau, R. B. C. H. R. H., Raman Spectra of Possible Corrosion Products of Iron. *Applied Spectroscopy* **1978,** *32*, 532-535.

46. Bersani, D.; Lottici, P. P.; Montenero, A., Micro-Raman investigation of iron oxide films and powders produced by sol–gel syntheses. *Journal of Raman Spectroscopy* **1999,** *30* (5), 355-360.

47. deFaria, D. L. A.; de Oliveira, M. T.; Silva, S. V., Raman Microspectroscopy of some iron oxides and oxyhydroxides. *Journal of Raman Spectroscopy* **1997,** *28*, 873-878.

48. Jubb, A. M.; Allen, H. C., Vibrational Spectroscopic Characterization of Hematite, Maghemite and Magnetite Thin Films Produced by Vapor Deposition. *ACS Appl. Mater. Interfaces* **2010,** *2*, 2804-2812.

49. Sirivisoot, S.; Harrison, B. S., Magnetically stimulated ciprofloxacin release form polymeric microspheres entrapping iron oxide nanoparticles. *International Journal of Nanomedicine* **2015,** *10* (1), 4447-4458.

50. Wu, C.; Yin, P.; Zhu, X.; OuYang, C.; Xie, Y., Synthesis of hematite (alpha-Fe2O3) nanorods: diameter-size and shape effects on their applications in magnetism, lithium ion battery, and gas sensors. *J Phys Chem B* **2006,** *110* (36), 17806-17812.

51. Li, Y.; Liao, H.; Qian, Y., Hydrothermal Synthesis of Ultrafine α-Fe2O3 and Fe3O4 Powders. *Materials Research Bulletin* **1998,** *33* (6), 841-844.

52. Ahmad, W. R. W.; Mamat, M. H.; Zoolfakar, A. S.; Khusaimi, Z.; Rusop, M. In *A review on hematite α-Fe2O3 focusing on nanostructures, synthesis methods and applications*, 2016 IEEE Student Conference on Research and Development (SCOReD), 13-14 Dec. 2016; 2016; pp 1-6.

53. Mulmudi, H. K.; Mathews, N.; Dou, X. C.; Xi, L. F.; Pramana, S. S.; Lam, Y. M.; Mhaisalkar, S. G., Controlled growth of hematite (α-Fe2O3) nanorod array on fluorine doped tin oxide: Synthesis and photoelectrochemical properties. *Electrochemistry Communications* **2011,** *13* (9), 951-954.

54. Mao, A.; Shin, K.; Kim, J. K.; Wang, D. H.; Han, G. Y.; Park, J. H., Controlled Synthesis of Vertically Aligned Hematite on Conducting Substrate for Photoelectrochemical Cells: Nanorods versus Nanotubes. *ACS Applied Materials & Interfaces* **2011,** *3* (6), 1852-1858.

55. Zhang, F.; Yang, H.; Xie, X.; Li, L.; Zhang, L.; Yu, J.; Zhao, H.; Liu, B., Controlled synthesis and gas-sensing properties of hollow sea urchin-like α-Fe2O3 nanostructures and α-Fe2O3 nanocubes. *Sensors and Actuators B: Chemical* **2009,** *141* (2), 381-389.

56. Tamirat, A. G.; Su, W.-N.; Dubale, A. A.; Pan, C.-J.; Chen, H.-M.; Ayele, D. W.; Lee, J.-F.; Hwang, B.-J., Efficient photoelectrochemical water splitting using three dimensional urchin-like hematite nanostructure modified with reduced graphene oxide. *Journal of Power Sources* **2015,** *287*, 119-128.

57. Zeng, S.; Tang, K.; Li, T.; Liang, Z., Hematite with the Urchinlike Structure: Its Shape-Selective Synthesis, Magnetism, and Enhanced Photocatalytic Performance after TiO2 Encapsulation. *The Journal of Physical Chemistry C* **2010,** *114* (1), 274-283.

58. Liu, J.; Liang, C.; Zhang, H.; Zhang, S.; Tian, Z., Silicon-doped hematite nanosheets with superlattice structure. *Chemical Communications* **2011,** *47* (28), 8040-8042.

59. Chemelewski, W. D.; Hahn, N. T.; Mullins, C. B., Effect of Si Doping and Porosity on Hematite's (α-Fe2O3) Photoelectrochemical Water Oxidation Performance. *The Journal of Physical Chemistry C* **2012,** *116* (8), 5255-5261.

60. Zeng, Y.; Han, Y.; Zhao, Y.; Zeng, Y.; Yu, M.; Liu, Y.; Tang, H.; Tong, Y.; Lu, X., Advanced Ti-Doped Fe2O3@PEDOT Core/Shell Anode for High-Energy Asymmetric Supercapacitors. *Adv. Energy Mater.* **2015,** *5*.

61. Ling, Y.; Li, Y., Review of Sn-Doped Hematite Nanostructures for Photoelectrochemical Water Splitting. *Particle & Particle Systems Characterization* **2014,** *31* (11), 1113-1121.

62. Ling, Y.; Wang, G.; Wheeler, D. A.; Zhang, J. Z.; Li, Y., Sn-Doped Hematite Nanostructures for Photoelectrochemical Water Splitting. *Nano Lett.* **2011,** *11*, 2119-2125.

63. Liao, P.; Toroker, M. C.; Carter, E. A., Electron Transport in Pure and Doped Hematite. *Nano Letters* **2011,** *11* (4), 1775-1781.

64. Colombo, C.; Palumbo, G.; Di Iorio, E.; Song, X.; Jiang, Z.; Liu, Q.; Angelico, R., Influence of hydrothermal synthesis conditions on size, morphology and colloidal properties of Hematite nanoparticles. *Nano-Structures & Nano-Objects* **2015,** *2*, 19-27.

65. Chung, S. H.; Ramadurgam, S.; Yang, C., Effect of dopants on epitaxial growth of silicon nanowires. *Nature Materials and Nanotechnology* **2014,** *4* (3), 1847-9804.

66. Deng, J.; Lv, X.; Gao, J.; Pu, A.; Li, M.; Sun, X.; Zhong, J., Facile synthesis of carbon-coated hematite nanostructures for solar water splitting. *Energy Environ. Sci.* **2013,** *6*, 1965-1970.

67. Li, S.; Zhang, P.; Song, X.; Gao, L., Ultrathin Ti-doped hematite photoanode by pyrolysis of ferrocene. *International Journal of Hydrogen Energy* **2014,** *39* (27), 14596-14603.

68. Deng, J.; Lv, X.; Gao, J.; Pu, A.; Li, M.; Sun, X.; Zhong, J., Facile synthesis of carbon-coated hematite nanostructures for solar water splitting. *Energy & Environmental Science* **2013,** *6* (6), 1965-1970.

69. Ferrari, A. C.; Robertson, J., Interpretation of Raman spectra of disordered and amorphous carbon. *Physical Review B* **2000,** *61*, 14095-14107.

70. Cardona, M. P.; Li, M.; Li, W.; McCall, J.; Wang, D.; Li, Y.; Yang, C., The role of graphene as an overlayer on nanostructured hematite photoanodes for improved solar water oxidation. *Materials Today Energy* **2018,** *8*, 8-14.

71. Wang, T.; Chen, Y.-N.; Chiang, C.-C.; Hsieh, Y.-K.; Li, P.-C.; Wang, C.-F., Carbon coated hematite electrodes with enhanced photoelectrochemical performance obtained through an electrodeposition method with a citric acid additive. *ChemElectroChem* **2016,** *3*, 966-975.

72. Wang, T. H.; Chiang, C.-C.; Wu, Y.-L.; Lin, C.; Cheng, Y.-J.; Hsieh, Y.-K.; Wang, C.-F.; Huang, C. P., Characteristics of elemental carbon overlayers on hematite electrodes prepared by electrodeposition with organic acid additives. *Appl. Catal., B* **2017,** *207*, 1-8.

73. Tamirat, A. G.; Su, W.-N.; Dubale, A. A.; Pan, C.-J.; Chen, H.-M.; Ayele, D. W.; Lee, J.-F.; Hwang, B.-J., Efficient photoelectrochemical water splitting using three dimensional urchin-like hematite nanostructure modified with reduced graphene oxide. *J. Power Sources* **2015,** *287*, 119-128.

74. Wu, Q.; Zhao, J.; Liu, K.; Wang, H.; Sun, Z.; Li, P.; Xue, S., Ultrathin hematite film for photoelectrochemical water splitting enhanced with reducing graphene oxide. *International Journal of Hydrogen Energy* **2015,** *40* (21), 6763-6770.

75. Zhang, Z.; Gao, C.; Li, Y.; Han, W.; Fu, W.; He, Y.; Xie, E., Enhanced charge separation and transfer through Fe 2 O 3 /ITO nanowire arrays wrapped with reduced graphene oxide for water-splitting. *Nano Energy* **2016,** *30*, 892-899.

76. Verdejo, R.; Bernal, M. M.; Romasanta, L. J.; Lopez-Manchado, M. A., Graphene filled polymer nanocomposites. *J. Mater. Chem.* **2011,** *21*, 3301-3310.

77. Stankovich, S.; Dikin, D. A.; Piner, R. D.; Kohlhaas, K. A.; Kleinhammes, A.; Jia, Y.; Wu, Y.; Nguyen, S. T.; Ruoff, R. S., Synthesis of graphene based nanosheets via chemical reduction of exfoliated graphite oxide. *Carbon* **2007,** *45*, 1558-1565.

78. Schedin, F.; Geim, A. K.; Morozov, S. V.; Hill, E. W.; Blake, P.; Katsnelson, M. I.; Novoselov, K. S., Detection of individual gas molecules adsorbed on graphene. *Nat. Mater.* **2007,** *6*, 652-655.

79. Berger, C.; Song, Z.; Li, X.; Wu, X.; Brown, N.; Naud, C.; Mayou, D.; Li, T.; Hass, J.; Mirchenkov, A. N.; Conrad, E. H.; First, P. N.; de Heer, W. A., Electronic Confinement and Coherence in Patterned Epitaxial Graphene. *Science* **2006,** *312*, 1191-1196.

80. Berger, C.; Song, Z.; Li, T.; Li, X.; Ogbazghi, A. Y.; Feng, R.; Dia, Z.; Marchenkov, A. N.; Conrad, E. H.; First, P. N.; de Heer, W. A., Ultrathin Epitaxial Graphite: 2D Electron Gas Properties and a Route toward Graphene-based Nanoelectronics. *J. Phys. Chem. B* **2004,** *108*, 19912-19916.

81. Novoselov, K. S.; Geim, A. K.; Morozov, S. V.; Jiang, D.; Zhang, Y.; Dubonos, S. V.; Grigorieva, I. V.; Firsov, A. A., Electric Field Effect in Atomically Thin Carbon Films. *Science* **2004,** *306*, 666-669.

82. Novoselov, K. S.; Jiang, D.; Schedin, F.; Booth, T. J.; Khotkevich, V. V.; Morozov, S. V.; Geim, A. K., Two Dimensional Atomic Crystals. *Proc. Natl. Acad. Sci. U. S. A.* **2005,** *102*, 10451-10453.

83. Chen, S.; Brown, L.; Levendorf, M.; Cai, W.; Ju, S.-Y.; Edgeworth, J.; Li, X.; Magnuson, C. W.; Velamakanni, A.; Piner, R. D.; Kang, J.; Park, J.; Ruoff, R. S., Oxidation Resistance of Graphene-Coated Cu and Cu/Ni Alloy. *ACS Nano* **2011,** *5* (2), 1321-1327.

84. Prasai, D.; Tuberquia, J. C.; Harl, R. R.; Jennings, G. K.; Bolotin, K. I., Graphene: Corrosion-inhibiting coating. *ACS Nano* **2012,** *6*, 1102-1108.

85. Nielander, A. C.; Bierman, M. J.; Petrone, N.; Strandwitz, N. C.; Ardo, S.; Yang, F.; Hone, J.; Lewis, N. S., Photoelectrochemical behavior of n-type Si(111) Electrodes coated with a single layer of graphene. *J. Am. Chem. Soc.* **2013,** *135*, 17246-17249.

86. Ritala, M.; Leskelä, M.; Nykänen, E.; Soininen, P.; Niinistö, L., Growth of titanium dioxide thin films by atomic layer epitaxy. *Thin Solid Films* **1993,** *225* (1), 288-295.

87. Wang, G.; Wang, H.; Ling, Y.; Tang, Y.; Yang, X.; Fitzmorris, R. C.; Wang, C.; Zhang, J. Z.; Li, Y., Hydrogen-Treated TiO2 Nanowire Arrays for Photoelectrochemical Water Splitting. *Nano Letters* **2011,** *11* (7), 3026-3033.

88. Li, X.; Cai, W.; An, J.; Kim, S.; Nah, J.; Yang, D.; Piner, R.; Velamakanni, A.; Jung, I.; Tutuc, E.; Banerjee, S. K.; Colombo, L.; Ruoff, R. S., Large-Area Synthesis of High-Quality and Uniform Graphene Films on Copper Foils. *Science* **2009,** *324*, 1312-1314.

89. Suk, J. W.; Kitt, A.; Mangnuson, C. W.; Hao, Y.; Ahmed, S.; An, J.; Swan, A. K.; Goldberg, B. B.; Ruoff, R. S., Transfer of CVD-Grown Monolayer Graphene onto Arbitrary Substrates. *ACS Nano* **2011,** *5*, 6916-6924.

90. Bunch, J. S.; Dunn, M. L., Adhesion mechanics of graphene membranes. *Solid State Communications* **2012,** *152*, 1359-1364.

91. Koenig, S. P.; Boddeti, N. G.; Dunn, M. L.; Bunch, J. S., Ultrastrong adhesion of graphene membranes. *Nature Nanotechnology* **2011,** *6*, 543-546.

92. Metzger, C.; Re, S.; Liu, M.; Kusminskiy, S. V.; Neto, A. H. C.; Swan, A. K.; Goldberg, B. B., Biaxial Strain in Graphene Adhered to Shallow Depressions. *Nano Lett.* **2010,** *10*, 6-10.

93. Gao, W.; Xiao, P.; Henkelman, G.; Leichti, K. M.; Huang, R., Interfacial adhesion between graphene and silicon dioxide by density functional theory with van der Waals corrections. *J. Phys. D: Appl. Phys.* **2010,** *47*, 1-6.

94. Das, A.; Chakraborty, B.; Sood, A. K., Raman Spectroscopy of graphene on different substrates and influence of defects. *Indian Academy of Sciences* **2008,** *31*, 579-584.

95. Ferrari, A. C.; Meyer, J. C.; Scardaci, V.; Chairaghi, C.; Lazzeri, M.; Mauri, F.; Piscance, S.; Jiang, D.; Novoselov, K. S.; Roth, S.; Geim, A. K., Raman Spectrum of Graphene and Graphene Layers. *Phys. Rev. Lett.* **2006,** *97*, 187401-187404.

96. Ferrari, A. C.; Robertson, J., Raman spectroscopy of amorphous , nanostructured , diamond-like carbon , and nanodiamond. *Phil. Trans. R. Soc. Lond. A* **2004,** *362*, 2477-2512.

97. Klahr, B.; Gimenez, S.; Fabregat-Santiago, F.; Bisquert, J.; Hamann, T. W., Photoelectrochemical and Impedance Spectroscopic Investigation of Water Oxidation with "Co-Pi"-Coated Hematite Electrodes. *J. Am. Chem. Soc.* **2012,** *134*, 16693-16700.

98. Hu, Y.-S.; Kleiman-Shwarsctein, A.; Forman, A. J.; Hazen, D.; Park, J.-N.; McFarland, E. W., Pt-Doped a-Fe2O3 Thin Films for Photoelectrochemical Water Splitting. *Chem. Mater.* **2008,** *20*, 3803-3805.

99. Cesar, I.; Sivula, K.; Kay, A.; Zboril, R.; Grätzel, M., Influence of Feature Size, Film Thickness, and Silicon Doping on the Performance of Nanostructured Hematite Photoanodes for Solar Water Splitting. *The Journal of Physical Chemistry C* **2009,** *113* (2), 772-782.

100. Bertoluzzi, L.; Bisquert, J., Investigating the consistency of models for water splitting systems b light and voltage modulated techniques. *J. Phys. Chem. Lett* **2017,** *8*, 172-180.

101. Ponomarev, E. A.; Peter, L. M., A comparison of intensity modulated photocurrent spectroscopy and photoelectrochemical impedance spectroscopy in a study of photoelectrochemical hydrogen evolution at p-InP. *J. Electroanal. Chem.* **1995,** *396*, 45-52.

102. Peter, L. M.; Wijayantha, K. G.; Tahir, A. A., Kinetics of light-driven oxygen evolution at alpha-Fe2O3 electrodes. *Faraday Discuss.* **2012,** *155*, 309-322.

103. Li, W.; He, D.; Sheehan, S. W.; He, Y.; Thorne, J. E.; Yao, X.; Brudvig, G. W.; Wang, D., Comparison of heterogenized molecular and heterogeneous oxide catalysts for photoelectrochemical water oxidation. *Energy Environ. Sci.* **2016,** *9*, 1794-1802.

104. Thorne, J. E.; Jang, J.-W.; Liu, E. Y.; Wang, D., Understanding the origin of photoelectrode performance enhancement by probing surface kinetics. *Chem. Sci.* **2016,** *7*, 3347-3354.

105. Zhang, W. F.; He, Y. L.; Zhang, M. S.; Yin, Z.; Chen, Q., Raman scattering study on anatase TiO 2 nanocrystals. *Journal of Physics D: Applied Physics* **2000,** *33* (8), 912.

106. Knight, M. W.; King, N. S.; Liu, L.; Everitt, H. O.; Nordlander, P.; Halas, N. J., Aluminum for Plasmonics. *ACS Nano* **2014,** *8* (1), 834-840.

107. Chan, G. H.; Zhao, J.; Hicks, E. M.; Schatz, G. C.; Van Duyne, R. P., Plasmonic Properties of Copper Nanoparticles Fabricated by Nanosphere Lithography. *Nano Letters* **2007,** *7* (7), 1947-1952.

108. Naik, G. V.; Kim, J.; Boltasseva, A., Oxides and nitrides as alternative plasmonic materials in the optical range [Invited]. *Optical Materials Express* **2011,** *1* (6), 1090-1099.

109. Naik, G. V.; Schroeder, J. L.; Ni, X.; Kildishev, A. V.; Sands, T. D.; Boltasseva, A., Titanium nitride as a plasmonic material for visible and near-infrared wavelengths. *Optical Materials Express* **2012,** *2* (4), 478-489.

110. Benia, H. M.; Guemmaz, M.; Schmerber, G.; Mosser, A.; Parlebas, J. C., Optical properties of non-stoichiometric sputtered zirconium nitride films. *Applied Surface Science* **2003,** *211* (1), 146-155.

111. Yu, I.-S.; Cheng, H.-E.; Chang, C.-C.; Lin, Y.-W.; Chen, H.-T.; Wang, Y.-C.; Yang, Z.-P., Substrate-insensitive atomic layer deposition of plasmonic titanium nitride films. *Optical Materials Express* **2017,** *7* (3), 777-784.

112. Wang, Y.; Capretti, A.; Dal Negro, L., Wide tuning of the optical and structural properties of alternative plasmonic materials. *Optical Materials Express* **2015,** *5* (11), 2415-2430.

113. Shah, D.; Reddy, H.; Kinsey, N.; Shalaev, V. M.; Boltasseva, A., Optical Properties of Plasmonic Ultrathin TiN Films. *Advanced Optical Materials* **2017,** *5* (13), 1700065.

114. Shah, D.; Catellani, A.; Reddy, H.; Kinsey, N.; Shalaev, V.; Boltasseva, A.; Calzolari, A., Controlling the Plasmonic Properties of Ultrathin TiN Films at the Atomic Level. *ACS Photonics* **2018,** *5* (7), 2816-2824.

115. Ramadurgam, S.; Hansen, K. E.; Lin, T.-g.; Dutta, A.; Abdul-Hadi, s.; Yang, C., Optical Properties of Single Coaxial Nanowires. 2015.

116. Hochbaum, A. I.; Fan, R.; He, R.; Yang, P., Controlled Growth of Si Nanowire Arrays for Device Integration. *Nano Letters* **2005,** *5* (3), 457-460.

117. Du, C.; Yang, X.; Mayer, M. T.; Hoyt, H.; Xie, J.; McMahon, G.; Bischoping, G.; Wang, D., Hematite-Based Water Splitting with Low Turn-On Voltages. *Angewandte Chemie International Edition* **2013,** *52* (48), 12692-12695.

118. Zgrabik, C. M.; Hu, E. L., Optimization of sputtered titanium nitride as a tunable metal for plasmonic applications. *Optical Materials Express* **2015,** *5* (12), 2786-2797.

119. Secondo, R.; Avrutin, V.; Özgür, Ü.; Kinsey, N. In *Optimization of Titanium Nitride Films using Plasma Enhanced Atomic Layer Deposition*, Conference on Lasers and Electro-Optics, San Jose, California, 2018/05/13; Optical Society of America: San Jose, California, 2018; p JTh2A.75.

120. Musschoot, J.; Xie, Q.; Deduytsche, D.; Van den Berghe, S.; Van Meirhaeghe, R. L.; Detavernier, C., Atomic layer deposition of titanium nitride from TDMAT precursor. *Microelectronic Engineering* **2009,** *86* (1), 72-77.

121. Longrie, D.; Deduytsche, D.; Haemers, J.; Smet, P. F.; Driesen, K.; Detavernier, C., Thermal and Plasma-Enhanced Atomic Layer Deposition of TiN Using TDMAT and NH3 on Particles Agitated in a Rotary Reactor. *ACS Applied Materials & Interfaces* **2014,** *6* (10), 7316-7324.

122. Chen, C. C.; Liang, N. T.; Tse, W. S.; Chen, I. Y.; Duh, J. G., Raman Spectra of Titanium Nitride Thin Films. *Chinese Journal of Physics* **1994,** *32* (2), 205-210.

123. Barshilia, H. C.; Rajam, K. S., Raman spectroscopy studies on the thermal stability of TiN, CrN, TiAlN coatings and nanolayered TiN/CrN, TiAlN/CrN multilayer coatings. *Journal of Materials Research* **2004,** *19* (11), 3196-3205.

124. Ponon, N. K.; Appleby, D. J. R.; Arac, E.; King, P. J.; Ganti, S.; Kwa, K. S. K.; O'Neill, A., Effect of deposition conditions and post deposition anneal on reactively sputtered titanium nitride thin films. *Thin Solid Films* **2015,** *578*, 31-37.

125. Jeon, T. H.; Moon, G.-h.; Park, H.; Choi, W., Ultra-efficient and durable photoelectrochemical water oxidation using elaborately designed hematite nanorod arrays. *Nano Energy* **2017,** *39*, 211-218.

126. Gurudayal; Sabba, D.; Kumar, M. H.; Wong, L. H.; Barber, J.; Grätzel, M.; Mathews, N., Perovskite–Hematite Tandem Cells for Efficient Overall Solar Driven Water Splitting. *Nano Letters* **2015,** *15* (6), 3833-3839.

VITA

Melissa Pittman Cardona was born in 1991 and grew up in Chappaqua, NY where she attended Horace Greeley High School. She graduated from the University of Rochester in 2013 with a Bachelor of Science degree in Chemistry. It was at the University of Rochester she was first introduced to interdisciplinary chemistry research and its applications to nanoscience and nanotechnology. Her undergraduate research, conducted in the Department of Chemical Engineering under the supervision of Professor Alexander Shestopalov, involved synthesis and characterization of self assembled monolayers for organic photovoltaic devices and fabrication of inorganic multi-component microparticles. In the fall of 2013 she went on to pursue her doctoral degree in Chemistry at Purdue University, where she joined Professor Chen Yang's group. In 2017, she relocated with the Yang Laboratory to Boston University where she continued her doctoral work as a Research Fellow. Her primary research area involves synthesizing, optimizing and understanding semiconductor nanomaterials for energy applications.

PUBLICATION

Contents lists available at ScienceDirect

Materials Today Energy

The role of graphene as an overlayer on nanostructured hematite photoanodes for improved solar water oxidation

Melissa P. Cardona [a, b], Mingyang Li [d], Wei Li [e], Jeremy McCall [a], Dunwei Wang [e], Yat Li [d], Chen Yang [b, c, *]

[a] Department of Chemistry, Purdue University, Indiana, United States
[b] Department of Electrical and Computer Engineering, Boston University, Massachusetts, United States
[c] Department of Chemistry, Boston University, Massachusetts, United States
[d] Department of Chemistry and Biochemistry, University of California at Santa Cruz, California, United States
[e] Department of Chemistry, Boston College, Massachusetts, United States

ARTICLE INFO

ABSTRACT

Photocatalysis is a clean, sustainable method of producing hydrogen fuel. Hematite (α-Fe$_2$O$_3$) is a promising photocatalytic material due to its favorable band gap, earth abundance and low cost. However, overcoming hematite's poor surface and electrical properties is crucial for reaching its theoretical potential. To this end, we show that single layer graphene transferred to the surface of nanostructured, titanium doped hematite results in a photocurrent density 1.6 times greater than bare hematite. Understanding the mechanism behind this enhancement is important for optimizing graphene coatings on photocatalysts. Electrical Impedance Spectroscopy reveals that graphene affects the surface-electrolyte interface without modifying the bulk of the hematite. Kinetic studies were performed using Intensity Modulated Photocurrent Spectroscopy, revealing that hematite with the graphene overlayer is able to transfer charge more efficiently due to a decrease in the surface recombination rate. Therefore, the main contribution of graphene on hematite is reduced surface recombination, resulting in a higher yield of charge carriers on the catalytic surface to participate in the oxygen evolution reaction. Single layer graphene overlayers have the potential to act as a general surface-modification technique to improve the photocurrent density of other metal oxide photocatalysts.

© 2018 Elsevier Ltd. All rights reserved.

1. Introduction

Today there is an imminent need for sustainable, cost-effective production of hydrogen to use as an alternative to fossil fuel. Solar water splitting, also known as photocatalysis, the process of using the sun's energy to decompose water into hydrogen and oxygen, is one method of sustainable hydrogen production. Among a long list of photocatalytic materials are semiconductor metal oxides such as TiO$_2$ [1] and α-Fe$_2$O$_3$ [2]. These are attractive photocatalysts due to their stability under basic conditions and low cost. Often, however, the photocurrent density of these materials is limited due to poor charge transfer kinetics and high rates of charge recombination. Much research has gone into overcoming these limitations [3–6].

* Corresponding author. Department of Electrical and Computer Engineering, Department of Chemistry, Boston University, Massachusetts, United States
E-mail address: cheyang@bu.edu (C. Yang).

Hematite (α-Fe$_2$O$_3$) is an optimal test material to study enhancement techniques for photoelectrochemical (PEC) applications. Its band alignment makes it a promising material to perform the oxygen evolution half-reaction, and its favorable band gap of 2.2 eV correlates to visible light absorption up to 560 nm. Despite its promising optical properties, compared to other photocatalytic materials it has particularly poor electrical properties, with a short electron/hole diffusion length 2–4 nm leading to high recombination rates [7]. Therefore, hematite underperforms compared its theoretical photocurrent density.

Carbon overlayers have shown promise for improving hematite photocurrent density. Hematite with carbon coatings formed via ferrocene pyrolysis and electrodeposition techniques using organic additives show a 4$\times$ and 3$\times$ improvement in photocurrent density, respectively [8–10]. Along with carbon coating the hematite surface, these synthesis techniques also increase hematite's donor density by one to two orders of magnitude. The increase in donor density makes the role of the carbon coating difficult to

fully understand: *Deng* et al. [8] attributes the PEC enhancement entirely to the increased donor density while *Wang* et al. [9,10] attributes the PEC enhancement to carbon acting as a passivation layer. Additionally, synthesis dependent coating techniques such as these do not present a general technique to modify a catalytic surface with already optimized donor densities and morphologies.

The carbon derivative reduced graphene oxide (rGO) can improve hematite's photocurrent density when used as an overlayer [11,12]. These studies imply that the rGO makes the surface more conductive, resulting in improved PEC properties. Alternatively, *Zhang* et al. [13] examined fluorine doped tin oxide (FTO)/hematite nanowires wrapped in rGO and found that rGO acts as a co-catalyst, improving the charge transfer. The conflicting explanations in the literature point to the difficulty of identifying the mechanism behind photocurrent density enhancement. While rGO allows for easy processing, it also has drawbacks as a carbon coating method; rGO has reduced conductivity due to surface functionality and high defects intrinsic to the process of reducing the graphene oxide precursor [14]. Additionally, an overlayer of rGO is made of nano- and micro-scale rGO flakes, and therefore the conductivity is controlled by the inter-particle contacts [15]. To compensate for this, studies of rGO overlayers use multiple layers of rGO flakes on the electrode surface, which could interfere with optical absorbance in the hematite and limit its practical applications.

A single atomic layer of carbon (single layer graphene or SLG) potentially has more favorable properties than rGO and amorphous carbon for PEC applications. As it is transparent, absorbing only 2% of light over the entire solar spectrum, SLG will not significantly interfere with the absorption in the hematite electrode. Additionally, a single graphene sheet has high mobility charge carriers, demonstrating charge carrier motilities of $\mu = 10^5$ cm^2/(Vs), even in the presence of many defects such as dopants [16—18], and charge carriers can travel thousands of interatomic distances without scattering [19,20]. SLG is chemically inert and therefore resistant to oxidation in air and electrochemical environments, specifically previously showing photoelectrochemical stability as an overlayer on water splitting silicon photoanodes [21—23]. One additional advantage is that graphene can be transferred to a variety of substrates, having the potential to act as a surface modification layer for a wide range of photocatalytic materials and morphologies. These are beneficial overlayer characteristics for circumventing the poor surface electrical properties of hematite.

In this work, we demonstrate for the first time that conformal, single layer graphene as an overlayer enhances the photocurrent density of stable photoanodes such as hematite doped with titanium. Importantly, we also performed detailed electrical impedance spectroscopy (EIS) and intensity modulated photocurrent spectroscopy (IMPS) to identify the mechanism of photocurrent improvement. Using EIS we demonstrate the changes in charge movement and storage on hematite's surface. Using IMPS, we studied the kinetics of the photoanode surface to directly show reduced recombination at the surface of hematite with graphene. Our studies suggest that the graphene overlayer can be a general strategy to improve the surface of metal oxide photoanodes.

2. Material and methods

2.1. Hematite thin film synthesis

Titanium doped hematite is synthesized similar to wet chemistry methods previously described [24—26]. It has been shown that hematite prepared using this method demonstrated better photocurrent density compared to other deposition methods. Specifically, hematite is prepared on fluorine doped tin oxide (FTO) substrates using ferric chloride using sodium nitrate and tetrabutyl titanate in an autoclave. The FTO substrates are placed into the autoclave for 1 h at 120 °C. The substrates are removed, washed with DI water and annealed in air at 550 °C for 30 min, followed by a high temperature air anneal at 700 °C for 20 min.

2.2. Synthesis and transfer of single layer graphene

Single layer graphene (SLG) is synthesized via chemical vapor deposition (EasyTube 3000, First Nano). As reported [27], the graphene growth is performed at 1035 °C using methane (20 sccm) and hydrogen (10 sccm) on a copper foil substrate. The SLG is transferred onto the hematite/FTO substrate using a previously reported transfer method [27,28]. The graphene is coated in poly methyl methacrylate (PMMA) and the back-side of the substrate is cleaned with oxygen plasma. The copper foil is then etched using an aqueous solution of ammonium persulfate and transferred to the hematite substrate. The graphene coated hematite is baked at 70 °C for 30 min, and 180 °C for 30 s. To remove the PMMA, the substrate is submerged in acetone for 30 min. To remove residual PMMA, the graphene coated hematite is annealed in air for 1 h at 300 °C. Typically, this final anneal would be performed in vacuum or in an inert/reducing atmosphere. However, to avoid reducing or creating oxygen vacancies in the hematite and maintain consistency between the graphene-coated and bare samples, PMMA residue removal is performed in air.

2.3. Structural characterization

Hematite with and without graphene is characterized using Raman Spectroscopy (Renishaw Raman) with 633 nm excitation laser. Scanning electron microscopy (SEM) images were taken to observe the hematite nanoparticle morphology (FEI NOVA nanoSEM).

2.4. Electrochemical characterization

Hematite thin films on FTO are fabricated into electrodes by attaching copper foil to the exposed FTO using conductive silver paint. Non-conductive epoxy was used to seal off the edges and exposed an active area of 0.25—0.40 cm^2. The photoelectrochemical measurements are carried out in 1 M NaOH using a three-electrode set up: Hematite working electrode, Pt-wire counter electrode, and Ag/AgCl reference electrode. Photoelectrochemical analysis is performed using a solar simulator (Newport, Model 69907), an AM 1.5 G filter and 150 W Xenon lamp, calibrated to 1 sun illumination (100 mW/cm^2) and a Solarton Analytical Modulab XM electrochemical station. Linear sweep voltammetry is measured from −0.2 to 0.6 V$_{Ag/AgCl}$. Solar electrical impedance spectroscopy (EIS) is performed using the same three-cell set up, sweeping the frequency from 100,000 Hz−0.01 Hz at voltages of −0.1 to 0.4 V$_{Ag/AgCl}$. Mott—Schottky analysis is performed at a constant 10,000 Hz under dark conditions, sweeping the voltage from −0.4 to 0.3 V$_{Ag/AgCl}$. All voltages are converted from Ag/AgCl to the reversible hydrogen electrode (RHE) scale using the Nernst equation:

$$E_{RHE} = E_{Ag/AgCl} + (0.059)(pH) + E^0_{Ag/AgCl}$$

where $E^0_{Ag/AgCl} = 0.1976$ V, $E_{Ag/AgCl}$ is measured experimentally against the Ag/AgCl reference electrode, and (pH) is the pH of the 1 M NaOH electrolyte.

2.5. Intensity modulated photocurrent spectroscopy (IMPS)

IMPS is measured under 405 nm illumination with 10% light modulation from −0.1 to 0.4 $V_{Ag/AgCl}$ using the same 3-electrode set-up described in section 2.4.

3. Results and discussion

To confirm the synthesis of nanostructured hematite, SLG and successful transfer of SLG to hematite, where all hematite samples are synthesized with the addition of tetrabutyl titanate and are therefore titanium doped, Raman Spectroscopy is performed (Fig. 1a). Eight peaks consistent with hematite (red) are observed: 220 (A_{1g}), 234 (E_g), 285 (E_g), 403 (E_g), 497 (A_{1g}), 602 (E_g), 650 (E_u) and 1317 (two magnon scattering) cm^{-1} [29]. Graphene was grown via CVD and transferred to SiO_2 (black), where bands are observed at 1320 (D), 1574 (G) and 2642 (2D) cm^{-1}. Graphene grown via CVD and transferred to the hematite (blue) has the same eight peaks as the bare hematite in addition to the characteristic graphene G and 2D bands located at 1572 and 2642 cm^{-1} respectively. The presence of all peaks associated with hematite and graphene confirms the graphene transfer process was successful. The downshift of the G band and the broadening of the G and 2D bands for graphene on hematite as compared to that on the planar SiO_2 is consistent with previous studies that demonstrate the strain graphene undergoes upon conforming to nanostructures [28,30–32]. We expect this interaction between SLG and hematite to be dominated via van der Waals forces, as demonstrated in previous calculations of graphene on SiO_2 [33].

The intensity ratio of the G band to the 2D band (I_G/I_{2D}) of 0.32 (black) on SiO_2 and 0.36 (blue) on hematite is consistent with graphene that is single layer [34,35]. It is worth noting that the graphene D band cannot be resolved for the graphene coated hematite sample as it overlaps with the two-magnon scattering peak in hematite. For the SLG on SiO_2, the disorder-induced D band is low in intensity, with an I_D/I_G of 0.16, indicating that the graphene has only minor defects. This I_D/I_G ratio and the position of the G band at 1574 cm^{-1} for SLG on SiO_2 and 1572 cm^{-1} for SLG on hematite indicate that the graphene is primarily sp^2 and is inconsistent with amorphous carbon or nanocrystalline graphite [36,37]. Finally, the transferred graphene is expected to be continuous over the hematite substrate [28].

To observe the hematite morphology, SEM images were taken of the samples with and without graphene (Fig. 1b and c). The synthesized hematite films have a textured, rod-like appearance similar to those previously reported [26]. The graphene transfer results in no apparent change on nanoparticle morphology or visual appearance of the thin films (Fig. 1 b, c insets).

To evaluate the effect of the SLG overlayer on the photocatalytic properties of hematite, the photocurrent density of the hematite and SLG coated hematite is compared using linear sweep voltammetry (LSV). Using 1 sun illumination, the photocurrent density of bare hematite is measured with and without the graphene overlayer (Fig. 2). Comparing photocurrent densities of the bare
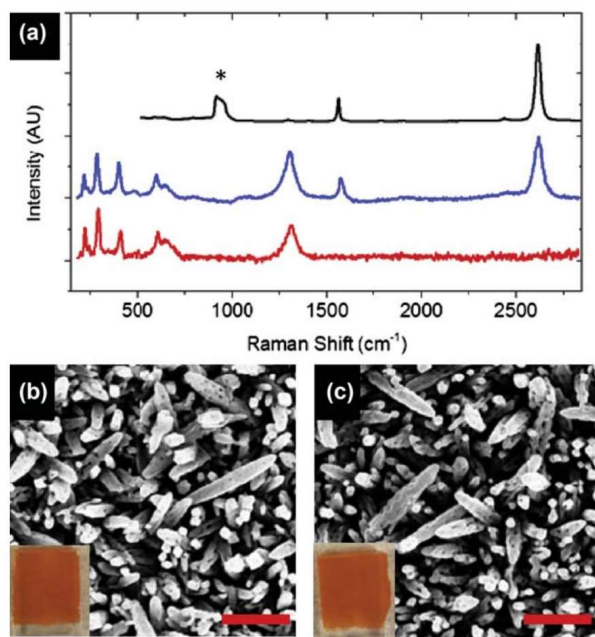
Fig. 1. (a) Raman spectrum of SLG transferred to SiO_2 (black) where * denotes peak from SiO_2 substrate, bare hematite (red) and SLG transferred to Ti-doped hematite (blue); SEM images of (b) Ti-doped hematite, (c) SLG coated Ti-doped hematite. Insets (b,c): digital photographs corresponding to SEM images. Scale bars are 500 nm. (For interpretation of the references to color/colour in this figure legend, the reader is referred to the Web version of this article.)

Fig. 2. Representative linear sweep voltammetry results comparing photocurrent densities of titanium doped hematite under one sun illumination (blue) and in the dark (gray) with (solid lines) and without (dashed lines) SLG overlayer. (For interpr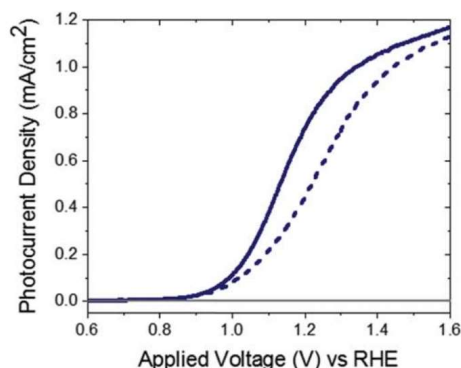etation of the references to color/colour in this figure legend, the reader is referred to the Web version of this article.)

hematite with (solid blue) and without (dashed blue) the SLG overlayer, it is observed that the LSV curves are similar in their shape and onset voltage of 0.9 V_{RHE} (Fig. 2). However, hematite with the SLG overlayer has a greater photocurrent density from 1.0 to 1.6 V_{RHE}. The result of this is at 1.23 V_{RHE}, the hematite with the SLG overlayer shows a photocurrent density 1.61 times greater than bare hematite. This is comparable to the 1.52 and 1.47 times increase seen by optimizing the thickness of rGO overlayers on nanostructured hematite [11,12].

The enhancement caused by the graphene coating shows good reproducibility despite sample-to-sample variation: at 1.23 V_{RHE}, bare hematite demonstrates an average photocurrent density of 0.46 ± 0.068 mA/cm^2; SLG coated hematite demonstrated a photocurrent density of 0.75 ± 0.094 mA/cm^2.

Understanding the mechanism underlying the enhancement caused by the SLG overlayer is crucial for designing effective overlayers as a performance improvement strategy for photoelectrocatalysis. To this end, we first determine if and how the SLG overlayer impacts the catalyst's properties at (1) the surface-electrolyte interface and (2) depletion region. Therefore, the electrochemical properties of hematite with and without the SLG overlayer were investigated using electrical impedance spectroscopy (EIS) (Fig. 3).

Nyquist plots (SI, Fig. S1) are constructed from the EIS analysis under 1 sun illumination and are analyzed using an equivalent circuit. While we acknowledge that there are other fitting methods for this data [6], we chose a 2RC equivalent circuit to model the surface and depletion region RC components of the photoanode (Fig. 3a). This equivalent circuit was chosen because for highly doped and nanostructured hematite, it cannot be assumed that the capacitance of the depletion region and surface are the same order of magnitude. Using the equivalent circuit with two RC elements in series accounts for processes occurring at both the surface and semiconductor bulk [5,38]. The capacitance and resistance of the depletion region are modeled by C_{SC} and R_{SC}, respectively. The RC components of the surface-electrolyte interface are the Helmholtz capacitance (C_H) and the charge transfer resistance (R_{CT}). R_s represents the series resistance.

EIS data is measured and modeled from 0.9 to 1.4 V_{RHE}. C_H is plotted as a function of applied voltage to observe the change in

bare and SLG coated hematite (Fig. 3b). In the presence of the SLG overlayer at 1.2 V_{RHE}, C_H increases by 26%, from 72.1 μF (blue squares) to 98.2 μF (open squares). This indicates charge carriers (holes) are collecting on the surface of the graphene/hematite electrode, meaning the graphene overlayer is more effective than bare hematite at storing photogenerated holes, especially at lower applied voltages. R_{CT} is plotted over the same voltage range. R_{CT} is found to be reduced at least a factor of two in the presence of the SLG overlayer in the range of 0.9–1.3 V_{RHE} (Fig. 3c). Specifically, at 1.2 V_{RHE}, R_{CT} decreases from 1005 Ω (red diamonds) to 456.7 Ω (open diamonds). This indicates that there is more charge movement on the graphene/hematite surface compared to bare hematite. It is worth noting that despite this overall trend, Fig. 3c shows that the R_{CT} for the bare Ti-doped hematite is 667 ± 40.1 Ω and the R_{CT} for SLG coated Ti-doped hematite is 753 ± 72.2 Ω. Therefore, statistically, the values for R_{CT} are equal at 1.4 V. A decrease in charge transfer resistance is consistent with previously demonstrated systems of rGO overlayers on hematite, which demonstrated an R_{CT} of 357.6 Ω for bare hematite to 337.9 Ω for rGO coated hematite thin films at 0.05 V_{RHE} under dark conditions [6]. The greater decrease in R_{CT} in the presence of SLG seen here suggests that SLG more positively affects the hematite surface compared to rGO.

Since there is no significant change in the space charge resistance or capacitance in the presence of SLG over this same voltage range (SI, Fig. S2), the graphene overlayer does not affect the depletion region significantly and is therefore a surface-only modification technique. This is further confirmed by the Mott–Schottky plot (Fig. 3d). The donor density (N_d) is calculated using the following equation:

$$N_d = \frac{2}{e_0 \varepsilon \varepsilon_0} \left(\frac{\partial C^{-2}}{\partial V} \right)^{-1}$$

where e_0 is the electron charge, ε is the dielectric constant of hematite, ε_0 is the permittivity in vacuum and $\left(\frac{\partial C^{-2}}{\partial V} \right)$ is the slope of the Mott–Schottky plot [39]. N_d of the bare hematite is 1.12×10^{18} cm^{-3} and the N_d of hematite with the SLG overlayer is 2.75×10^{18} cm^{-3}, confirming that the SLG overlayer does not significantly affect the donor density of the photoanode material. This is unlike carbon-coated hematite systems synthesized via ferrocene pyrolysis or electrodeposition, where the carbon overlayer significantly increases the donor density, which may contribute the increase in photocurrent density, making it difficult to isolate the impact of the overlayer [8–10]. In this SLG coated hematite system, the decreased charge transfer resistance is likely a main contributor to increased photocurrent density seen with the SLG overlayer.

Though it is a standard technique for understanding catalyst properties, EIS only gives partial insight into how exactly the SLG overlayer is improving hematite's photocurrent density. EIS has previously reported to be most useful for demonstrating the modes of charge storage in hematite photoanodes [40]. Reduced R_{CT} is often attributed an increase in the rate of charge transfer, but it may also or instead be due to a decrease in the rate of electron/hole recombination or charge mobility across a surface. With EIS alone, it is impossible to conclude which mechanism is most accurate for a given system.

To better understand the kinetic mechanism behind the reduced resistance of the oxygen evolution reaction measured by EIS, we employ Intensity Modulated Photocurrent Spectroscopy (IMPS) to directly measure the kinetics of the photoanode surface. IMPS, first demonstrated by *Peter* et al. [41], is a technique that involves measuring frequency responses of the photocurrent to small
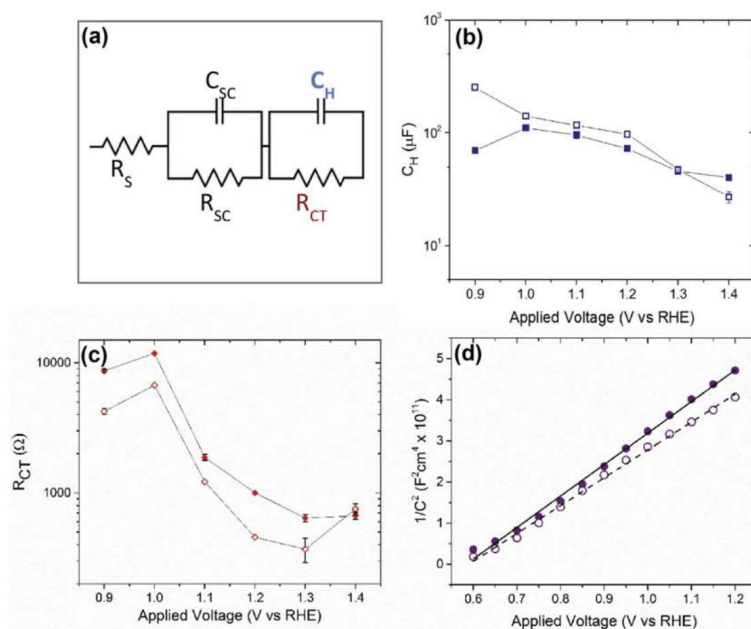
Fig. 3. Electrical Impedance Spectroscopy: (a) equivalent circuit used to model EIS Nyquist Plots (b) Helmholtz capacitance (C_H) (c) charge transfer resistance (R_{CT}). (d) Mott−Schottky plot obtained at 10 kHz frequency under dark conditions. All plotted for titanium doped hematite with (open markers) and without (filled markers) SLG overlayer.

modulations in the illumination intensity. Using this information, rate constants for electron transfer and recombination are obtained. IMPS has been previously used to observe hematite and the effect of overlayers on hematite [42−44].

Here, IMPS is used to measure and compare the charge transfer efficiency (CTE), charge transfer rate and recombination rate on the hematite surface with and without a graphene overlayer. The results demonstrate an increase in the charge transfer efficiency in the range of 0.9−1.4 V_{RHE} for SLG coated hematite compared to bare hematite (Fig. 4). At 1.2 V_{RHE}, CTE is 8% higher for graphene coated samples compared to the bare hematite. Similar to the R_{CT} measurements, the CTE values begin to converge at 1.4 V_{RHE}. Based on CTE, the rate constants for charge transfer (k_{tran}) and recombination (k_{rec}) are calculated. CTE and the rate constants are related by:

$$CTE = \frac{k_{tran}}{k_{tran} + k_{rec}}$$

The SLG overlayer affects both rate constants (Fig. 5). The rate of charge transfer, k_{tran}, decreases in the presence of SLG, a 69% difference at 1.2 V_{RHE} compared to bare hematite (Fig. 5a). The rate of recombination, k_{rec}, decreases as voltage increases for Ti-doped hematite with and without the graphene overlayer (Fig. 5b). For all voltages, k_{rec} is lower for the graphene coated samples compared to the bare samples, specifically dropping from 71 s^{-1} to 13 s^{-1}, or 82%, at 1.2 V_{RHE}. Though the magnitude of k_{rec} decreases as voltage increases, the relative gap between the two does not decrease. This can be observed more clearly when the y-axis is plotted on a logarithmic scale, as seen in Fig. 5c. From this
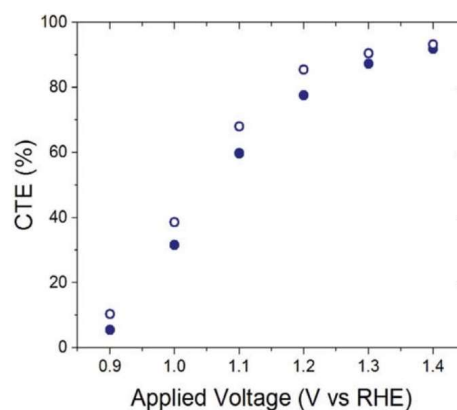

Fig. 4. IMPS results depicting charge transfer efficiency (CTE) for titanium doped hematite with (open circles) and without (filled circles) SLG overlayer.

information, we conclude that SLG as an overlayer on hematite suppresses charge recombination and inhibits charge transfer at the surface of the photoanode. This result is similar to those of NiFeO and cobalt oxide overlayers on hematite, both of which conclude that suppressing the recombination rate results in more
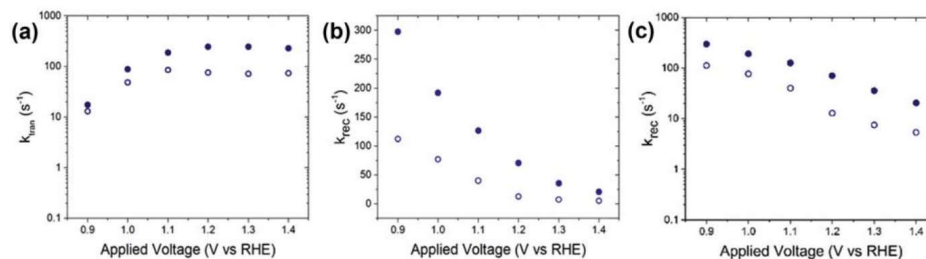
Fig. 5. Effect of the single layer graphene overlayer on the kinetic rate constants (a) Charge transfer rate constant (k_{tran}) (b) charge recombination rate constant (k_{rec}) plotted with a linear y-axis and (c) k_{rec} plotted with logarithmic y-axis. All plotted for titanium doped hematite with (open circles) and without (filled circles) single layer graphene; data measured under light illumination of 405 nm.

significant increases to the CTE, and therefore the photocurrent density, than the charge transfer rate [42,44].

Based on the results from IMPS and the data presented herein, we demonstrate that the improved photocurrent density under 1 sun illumination is due to a graphene overlayer dramatically decreasing the rate of charge recombination at the surface-electrolyte interface, which ultimately improves the charge transfer efficiency of the surface. This is likely due to graphene's high planar conductivity and charge mobility, resulting in an increase yield of holes on the surface of the photoanode to participate in the oxygen evolution reaction.

4. Conclusion

In conclusion, single layer graphene grown on copper foils via CVD can be successfully transferred onto titanium doped hematite nanostructured films, and these novel graphene/hematite heterostructures show an increased photocurrent density 1.61 times greater than bare hematite at 1.23 V vs RHE. Additionally, we gained understanding regarding the mechanism through which the graphene overlayer improves hematite's photocurrent density. Through EIS we have demonstrated that the SLG overlayer impacts the RC components at the surface electrolyte interface while not significantly modifying the space charge region. SLG reduces the charge transfer resistance compared to the bare hematite film. Using IMPS, we show an 8% increase in charge transfer efficiency in the presence of the graphene overlayer. The increased CTE and decreased charge transfer resistance results from the reduction in k_{rec}. Because IMPS also demonstrates a decrease in k_{tran} in the presence of the SLG overlayer, the decreased charge transfer resistance observed via EIS cannot be attributed to an increase in the charge transfer rate, but can be attributed to the increased charge transfer efficiency and the decrease in the surface recombination rate. Therefore, CVD grown single layer graphene transferred to nanostructured hematite acts as a passivation layer, and not as a co-catalyst.

Using graphene transferred to photocatalysts has the potential to be used as a general method of improving solar water splitting on metal oxide photoanodes. Future studies are needed to optimize the layer number and quality of graphene overlayers to achieve the best charge transfer rates while maintaining low recombination rates to best improve the photocurrent density of these photoelectrodes.

Acknowledgements

The authors would like to acknowledge Professor Christina W. Li at Purdue University for access to instrumentation for some of the electrochemical measurements and Professor Jinliang Jia for help with sample preparation during his time as a visiting scholar in Professor Yang's group.

Appendix A. Supplementary data

Supplementary data related to this article can be found at https://doi.org/10.1016/j.mtener.2018.02.002.

References

[1] A. Fujishima, K. Honda, Electrochemical photolysis of water at a semiconductor electrode, Nature 238 (1972) 37–38, https://doi.org/10.1038/238037a0.
[2] K.L. Hardee, A.J. Bard, Semiconductor electrodes: V. The application of chemically vapor deposited iron oxide films to photosensitized electrolysis, J. Electrochem. Soc. 123 (1976) 1024–1026, https://doi.org/10.1149/1.2132984.
[3] K. Zhang, L. Wang, J.K. Kim, M. Ma, G. Veerappan, C. Lee, K. Kong, H. Lee, J.H. Park, An order/disorder/water junction system for highly efficient co-catalyst-free photocatalytic hydrogen generation, Energy Environ. Sci. 9 (2016) 499–503, https://doi.org/10.1039/C5EE03100A.
[4] K. Zhang, X. Shi, J.K. Kim, J.S. Lee, J.H. Park, Inverse opal structured a-Fe₂O₃ on graphene thin films: enhanced photo-assisted water splitting, Nanoscale 5 (2013) 1939–1944, https://doi.org/10.1039/c2nr33036a.
[5] F. Le Formal, N. Tétreault, M. Cornuz, T. Moehl, M. Gratzel, K. Sivula, Passivating surface states on water splitting photoanodes with alumina overlayers, Chem. Sci. 2 (2011) 737–743.
[6] B. Klahr, S. Gimenez, F. Fabregat-Santiago, J. Bisquert, T.W. Hamann, Photoelectrochemical and impedance spectroscopic investigation of water oxidation with "Co-Pi"-Coated hematite electrodes, J. Am. Chem. Soc. 134 (2012) 16693–16700.
[7] J.H. Kennedy, K.W. Frese Jr., Photooxidation of water at a-Fe₂O₃ electrodes, J. Electrochem. Soc. 125 (1978) 709–714.
[8] J. Deng, X. Lv, J. Gao, A. Pu, M. Li, X. Sun, J. Zhong, Facile synthesis of carbon-coated hematite nanostructures for solar water splitting, Energy Environ. Sci. 6 (2013) 1965–1970, https://doi.org/10.1039/c3ee00066d.
[9] T. Wang, Y.-N. Chen, C.-C. Chiang, Y.-K. Hsieh, P.-C. Li, C.-F. Wang, Carbon coated hematite electrodes with enhanced photoelectrochemical performance obtained through an electrodeposition method with a citric acid additive, ChemElectroChem 3 (2016) 966–975.
[10] T.H. Wang, C.-C. Chiang, Y.-L. Wu, C. Lin, Y.-J. Cheng, Y.-K. Hsieh, C.-F. Wang, C.P. Huang, Characteristics of elemental carbon overlayers on hematite electrodes prepared by electrodeposition with organic acid additives, Appl. Catal. B 207 (2017) 1–8.
[11] A.G. Tamirat, W.-N. Su, A.A. Dubale, C.-J. Pan, H.-M. Chen, D.W. Ayele, J.-F. Lee, B.-J. Hwang, Efficient photoelectrochemical water splitting using three dimensional urchin-like hematite nanostructure modified with reduced graphene oxide, J. Power Sources 287 (2015) 119–128.
[12] Q. Wu, J. Zhao, K. Liu, H. Wang, Z. Sun, P. Li, S. Xue, Ultrathin hematite film for photoelectrochemical water splitting enhanced with reducing graphene oxide, Int. J. Hydrogen Energy 40 (2015) 6763–6770.

[13] Z. Zhang, C. Gao, Y. Li, W. Han, W. Fu, Y. He, E. Xie, Enhanced charge separation and transfer through Fe 2 O 3/ITO nanowire arrays wrapped with reduced graphene oxide for water-splitting, Nano Energy 30 (2016) 892–899.

[14] R. Verdejo, M.M. Bernal, L.J. Romasanta, M.A. Lopez-Manchado, Graphene filled polymer nanocomposites, J. Mater. Chem. 21 (2011) 3301–3310.

[15] S. Stankovich, D.A. Dikin, R.D. Piner, K.A. Kohlhaas, A. Kleinhammes, Y. Jia, Y. Wu, S.T. Nguyen, R.S. Ruoff, Synthesis of graphene based nanosheets via chemical reduction of exfoliated graphite oxide, Carbon. 45 (2007) 1558–1565.

[16] F. Schedin, A.K. Geim, S.V. Morozov, E.W. Hill, P. Blake, M.I. Katsnelson, K.S. Novoselov, Detection of individual gas molecules adsorbed on graphene, Nat. Mater. 6 (2007) 652–655.

[17] C. Berger, Z. Song, T. Li, X. Li, A.Y. Ogbazghi, R. Feng, Z. Dia, A.N. Marchenkov, E.H. Conrad, P.N. First, W.A. de Heer, Ultrathin epitaxial graphite: 2D electron gas properties and a route toward graphene-based nanoelectronics, J. Phys. Chem. B 108 (2004) 19912–19916.

[18] C. Berger, Z. Song, X. Li, X. Wu, N. Brown, C. Naud, D. Mayou, T. Li, J. Hass, A.N. Mirchenkov, E.H. Conrad, P.N. First, W.A. de Heer, Electronic confinement and coherence in patterned epitaxial graphene, Science (80-.) 312 (2006) 1191–1196. http://science.sciencemag.org/content/312/5777/1191.long.

[19] K.S. Novoselov, A.K. Geim, S. V Morozov, D. Jiang, Y. Zhang, S. V Dubonos, I. V Grigorieva, A.A. Firsov, Electric field effect in atomically thin carbon films, Science (80-.) 306 (2004) 666–669.

[20] K.S. Novoselov, D. Jiang, F. Schedin, T.J. Booth, V.V. Khotkevich, S.V. Morozov, A.K. Geim, Two dimensional atomic crystals, Proc. Natl. Acad. Sci. U. S. A 102 (2005) 10451–10453.

[21] S. Chen, L. Brown, M. Levendorf, W. Cai, S.Y. Ju, J. Edgeworth, X. Li, C.W. Magnuson, A. Velamakanni, R.D. Piner, J. Kang, J. Park, R.S. Ruoff, Oxidation resistance of graphene-coated Cu and Cu/Ni alloy, ACS Nano 5 (2011) 1321–1327, https://doi.org/10.1021/nn103028d.

[22] D. Prasai, J.C. Tuberquia, R.R. Harl, G.K. Jennings, K.I. Bolotin, Graphene: corrosion-inhibiting coating, ACS Nano 6 (2012) 1102–1108, https://doi.org/10.1021/nn203507y.

[23] A.C. Nielander, M.J. Bierman, N. Petrone, N.C. Strandwitz, S. Ardo, F. Yang, J. Hone, N.S. Lewis, Photoelectrochemical behavior of n-type Si(111) electrodes coated with a single layer of graphene, J. Am. Chem. Soc. 135 (2013) 17246–17249.

[24] Y. Ling, G. Wang, D.A. Wheeler, J.Z. Zhang, Y. Li, Sn-doped hematite nanostructures for photoelectrochemical water splitting, Nano Lett. 11 (2011) 2119–2125, https://doi.org/10.1021/nl200708y.

[25] G. Wang, Y. Ling, D.A. Wheeler, K.E.N. George, K. Horsley, C. Heske, J.Z. Zhang, Y. Li, Facile synthesis of highly photoactive α-Fe₂O₃ based films for water oxidation, Nano Lett. 11 (2011) 3503–3509, https://doi.org/10.1021/nl202316j.

[26] Y. Zeng, Y. Han, Y. Zhao, Y. Zeng, M. Yu, Y. Liu, H. Tang, Y. Tong, X. Lu, Advanced Ti-Doped Fe2O3@PEDOT core/shell anode for high-energy asymmetric supercapacitors, Adv. Energy Mater 5 (2015), https://doi.org/10.1002/aenm.201402176.

[27] X. Li, W. Cai, J. An, S. Kim, J. Nah, D. Yang, R. Piner, A. Velamakanni, I. Jung, E. Tutuc, S.K. Banerjee, L. Colombo, R.S. Ruoff, Large-area synthesis of high-quality and uniform graphene films on copper foils, Science (80-.) 324 (2009) 1312–1314, https://doi.org/10.1126/science.1171245.

[28] J.W. Suk, A. Kitt, C.W. Mangnuson, Y. Hao, S. Ahmed, J. An, A.K. Swan, B.B. Goldberg, R.S. Ruoff, Transfer of CVD-grown monolayer graphene onto arbitrary substrates, ACS Nano 5 (2011) 6916–6924.

[29] A.M. Jubb, H.C. Allen, Vibrational spectroscopic characterization of hematite, maghemite and magnetite thin films produced by vapor deposition, ACS Appl. Mater. Interfaces 2 (2010) 2804–2812.

[30] J.S. Bunch, M.L. Dunn, Adhesion mechanics of graphene membranes, Solid State Commun. 152 (2012) 1359–1364, https://doi.org/10.1016/j.ssc.2012.04.029.

[31] S.P. Koenig, N.G. Boddeti, M.L. Dunn, J.S. Bunch, Ultrastrong adhesion of graphene membranes, Nat. Nanotechnol. 6 (2011) 543–546, https://doi.org/10.1038/nnano.2011.123.

[32] C. Metzger, S. Re, M. Liu, S.V. Kusminskiy, A.H.C. Neto, A.K. Swan, B.B. Goldberg, Biaxial strain in graphene adhered to shallow depressions, Nano Lett. 10 (2010) 6–10, https://doi.org/10.1021/nl901625v.

[33] W. Gao, P. Xiao, G. Henkelman, K.M. Leichti, R. Huang, Interfacial adhesion between graphene and silicon dioxide by density functional theory with van der Waals corrections, J. Phys. D Appl. Phys. 47 (2010) 1–6.

[34] A. Das, B. Chakraborty, A.K. Sood, Raman Spectroscopy of graphene on different substrates and influence of defects, Indian Acad. Sci. 31 (2008) 579–584.

[35] A.C. Ferrari, J.C. Meyer, V. Scardaci, C. Chairaghi, M. Lazzeri, F. Mauri, S. Piscance, D. Jiang, K.S. Novoselov, S. Roth, A.K. Geim, Raman spectrum of graphene and graphene layers, Phys. Rev. Lett. 97 (2006) 187401–187404.

[36] A.C. Ferrari, J. Robertson, Interpretation of Raman spectra of disordered and amorphous carbon, Phys. Rev. B 61 (2000) 14095–14107, https://doi.org/10.1103/PhysRevB.61.14095.

[37] A.C. Ferrari, J. Robertson, Raman spectroscopy of amorphous, nanostructured, diamond-like carbon, and nanodiamond, Phil. Trans. R. Soc. Lond. A. 362 (2004) 2477–2512, https://doi.org/10.1098/rsta.2004.1452.

[38] Y.-S. Hu, A. Kleiman-Shwarsctein, A.J. Forman, D. Hazen, J.-N. Park, E.W. McFarland, Pt-doped a-Fe₂O₃ thin films for photoelectrochemical water splitting, Chem. Mater. 20 (2008) 3803–3805.

[39] I. Cesar, K. Sivula, A. Kay, R. Zboril, M. Grätzel, Influence of feature size, film thickness, and silicon doping on the performance of nanostructured hematite photoanodes for solar water splitting, J. Phys. Chem. C 113 (2009) 772–782, https://doi.org/10.1021/jp809060p.

[40] L. Bertoluzzi, J. Bisquert, Investigating the consistency of models for water splitting systems b light and voltage modulated techniques, J. Phys. Chem. Lett. 8 (2017) 172–180.

[41] E.A. Ponomarev, L.M. Peter, A comparison of intensity modulated photocurrent spectroscopy and photoelectrochemical impedance spectroscopy in a study of photoelectrochemical hydrogen evolution at p-InP, J. Electroanal. Chem. 396 (1995) 45–52.

[42] L.M. Peter, K.G. Wijayantha, AA. Tahir, Kinetics of light-driven oxygen evolution at alpha-Fe2O3 electrodes, Faraday Discuss 155 (2012) 309–322.

[43] W. Li, D. He, S.W. Sheehan, Y. He, J.E. Thorne, X. Yao, G.W. Brudvig, D. Wang, Comparison of heterogenized molecular and heterogeneous oxide catalysts for photoelectrochemical water oxidation, Energy Environ. Sci. 9 (2016) 1794–1802.

[44] J.E. Thorne, J.-W. Jang, E.Y. Liu, D. Wang, Understanding the origin of photoelectrode performance enhancement by probing surface kinetics, Chem. Sci. 7 (2016) 3347–3354.